(NASA-CR-174328) A COMETARY ION MASS SPECTROMETER Final Report (Lockheed Missiles and Space Co.) 111 p HC A06/MF A01 CSCL 14B N85-17343

Unclas
G3/35 01517

LOCKHEED
PALO ALTO RESEARCH LABORATORY

LOCKHEED MISSILES & SPACE COMPANY, INC. • A SUBSIDIARY OF LOCKHEED AIRCRAFT CORPORATION

LMSC/F018835

FINAL REPORT ON

CONTRACT NASW-3572

A Contract to Develop a Cometary Ion Mass Spectrometer

Prepared by

E. G. Shelley
and
D. A. Simpson

LOCKHEED PALO ALTO RESEARCH LABORATORY
LOCKHEED MISSILES & SPACE COMPANY, INC.

TABLE OF CONTENTS

1. INTRODUCTION

1.1 Background

This was a contract to develop flight suitable analyzer units for that part of the GIOTTO Ion Mass Spectrometer (IMS) experiment designated the High Energy Range Spectrometer (HERS) and to deliver these units to the University of Bern for further testing, integration with the remaining components of the instrument, integration into the GIOTTO payload, and flight to Comet Halley. The specific tasks included the preparation of a detailed design of the total ion-optical system for the HERS analyzer, the preparation of the detailed design of the analyzing magnet, the detailed evaluation of microchannel plate detectors and associated two-dimensional anode arrays, and the fabrication and evaluation of two flight-suitable units of the complete ion-optical analyzer system including two-dimensinal imaging detectors and associated image encoding electronics.

The GIOTTO IMS project is an international team effort including team members from seven institutions. These institutions include the University of Bern (UoB), Bern, Switzerland; the Max-Planck Institute for Aeronomy (MPAE), Lindau, West Germany; the Danish Space Research Institute (DSRI), Lyngby, Denmark; the Jet Propulsion Laboratory (JPL); the Los Alamos National Laboratory (LANL); the Massachusetts Institute of Technology (MIT); and the Lockheed Palo Alto Research Laboratories (LPARL). JPL and MIT are responsible for the conceptual design of the ion optics and ongoing support for computer modeling of the ion optical elements as they evolve. Their effort is supported by NASA through the GIOTTO Co-I program. The Max-Planck Institute is responsible for the design, development and fabrication of all electronics except for the detector and imaging encoding components. The University of Bern is responsible for the integration, testing and calibration of the overall instrument and for the fabrication of the magnetic section of the ion optics. Lockheed has responsibility for the detailed design and fabrication of the ion optics, including the imaging detector and associated image encoding electronics, but excluding the magnet fabrication. Lockheed also supports the instrument integration and calibration. The responsibilities of the other institutions are limited to consultation on the instrument design and participation in the operations planning and data analysis. This report will be limited primarily to the Lockheed portion of the HERS instrument design and fabrication.

1.2 Overview of Optics

Figure 1 is a schematic depiction of the entire HERS ion optics system. Figures 2 and 3 are photographs of the actual optical system as seen from two different aspects angles. The ions enter through the front collimating aperture which ultimately sets the limits on which ions will be accepted by the instrument. This aperture is most clearly seen in Figure 2. As depicted in Figure 1, the ion trajectories cross over one another in the vicinity of this aperture, thus in spite of the large field of view ($\approx 60^0$) the physical size of the aperture is very limited.

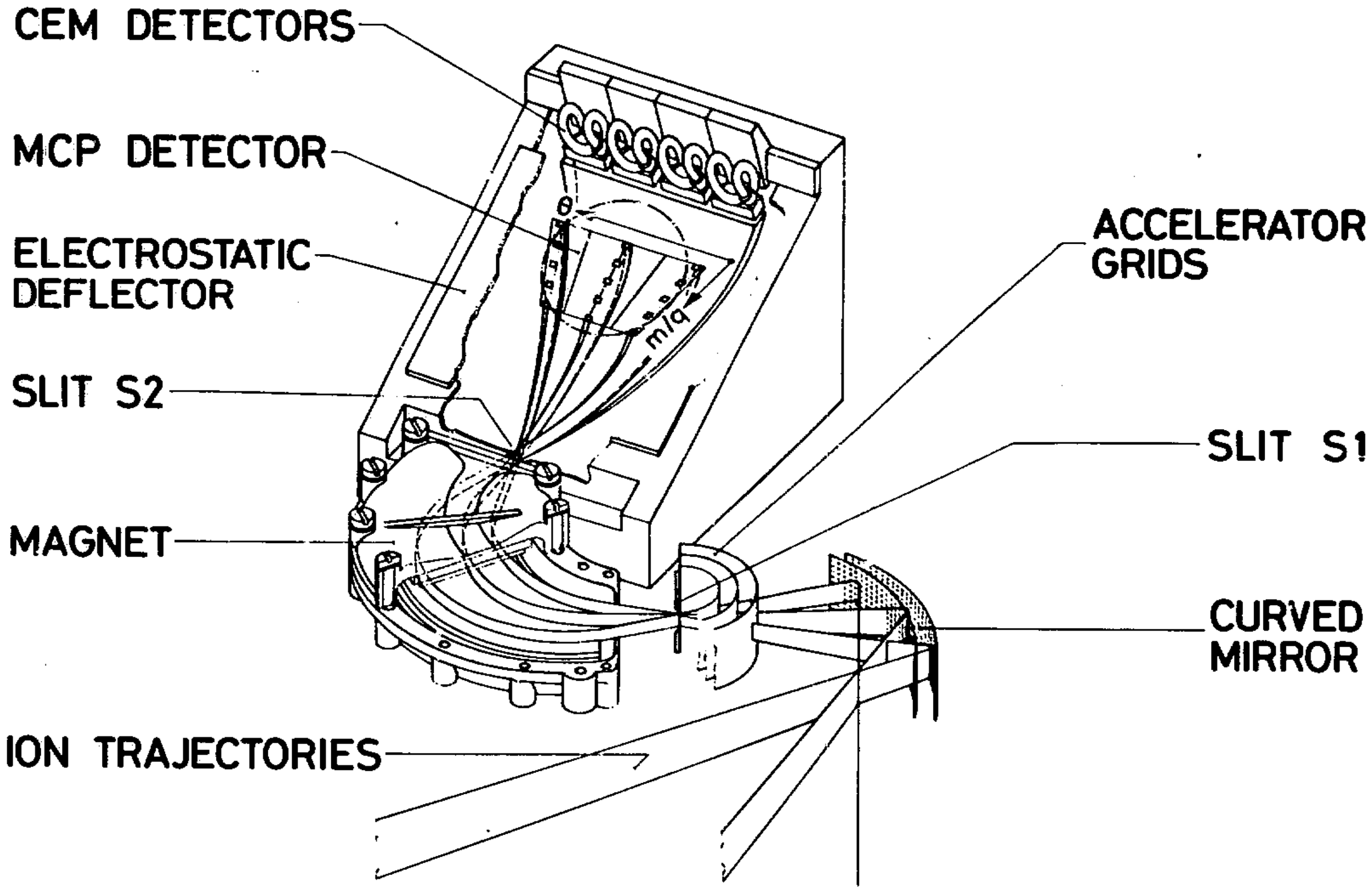

Figure 1. Schematic depiction of the HERS ion optics showing the key optical elements.

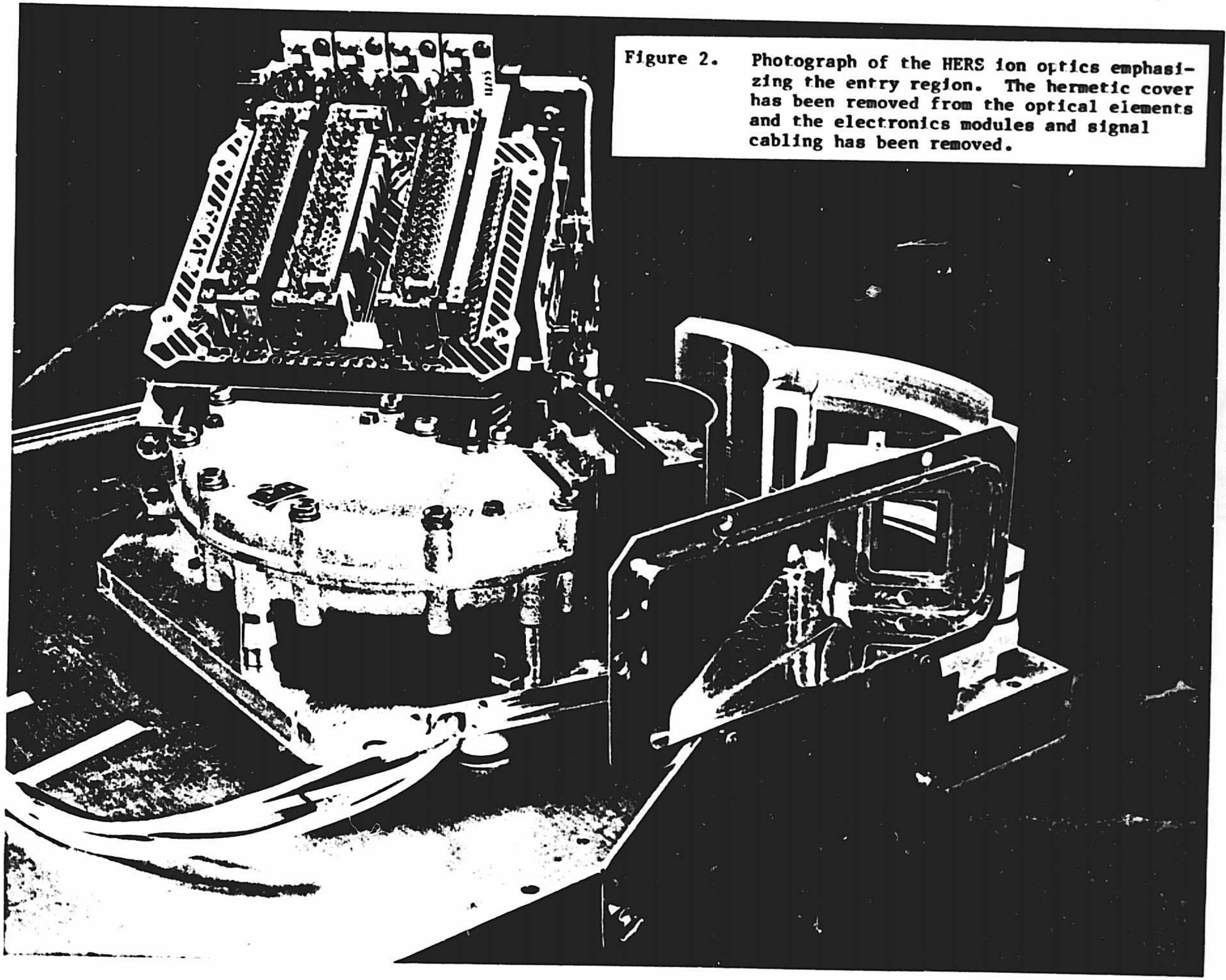

Figure 2. Photograph of the HERS ion optics emphasizing the entry region. The hermetic cover has been removed from the optical elements and the electronics modules and signal cabling has been removed.

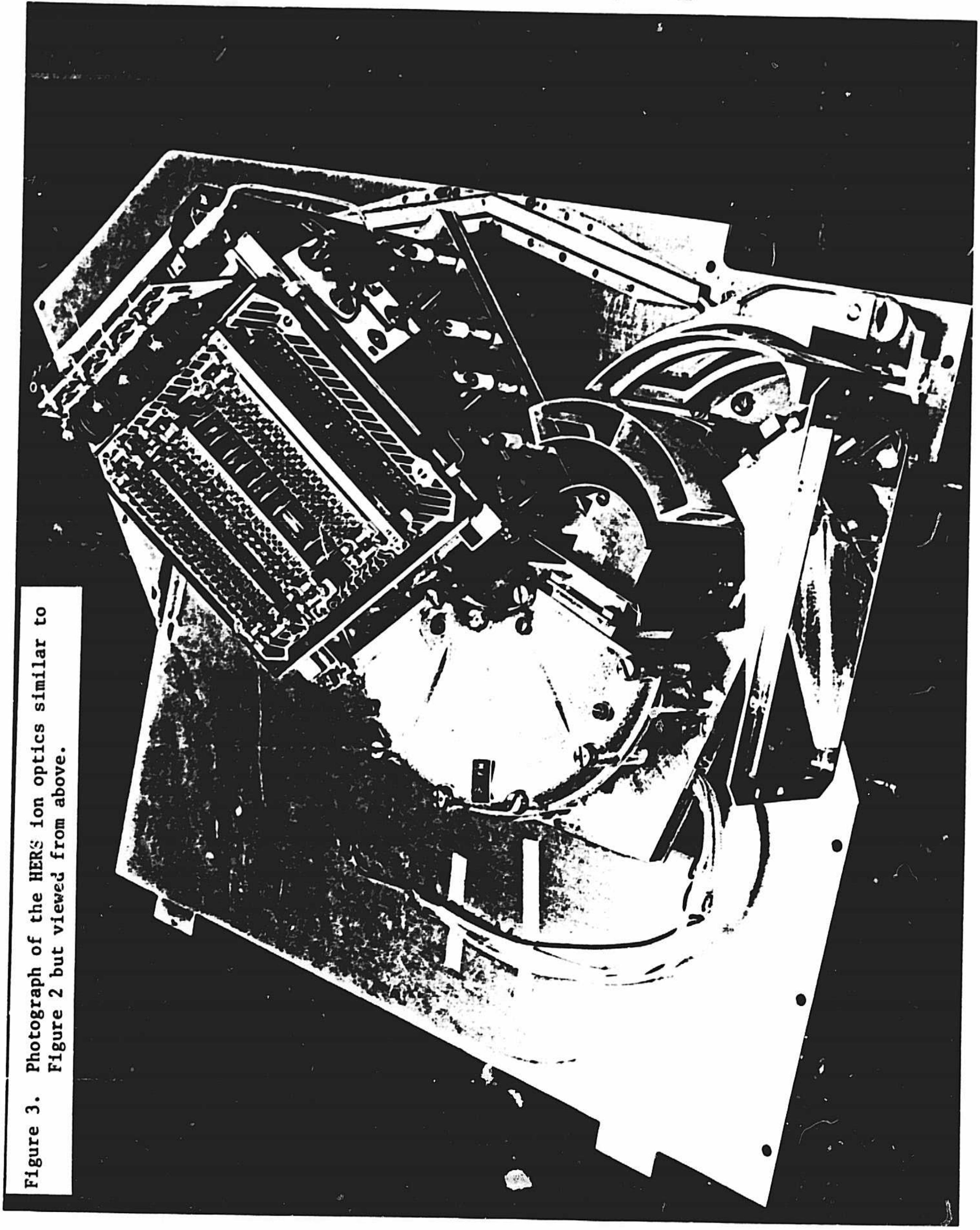

Figure 3. Photograph of the HERS ion optics similar to Figure 2 but viewed from above.

Following the collimator, the ions are reflected from a curved electrostatic mirror. This mirror is labeled in Figure 1 and is clearly identifiable in Figure 3 as the gold plated element in the lower right corner of the photograph. The mirror serves two purposes. It reflects ions of the desired energy range into the remainder of the optical system and it compresses the external 60° field of view into an internal angular range of only 30° (the latter is limited by the size of the magnetic analyzer). The reflected ions next pass through a cylindrical acceleration region where the ions are either accelerated or decellerated such that ions of the desired external energy have the correct momentum to pass through the fixed field magnetic analyzer. This section is labeled "accelerator grids" in Figure 1. It consists of three concentric cylinders and is clearly visible in the photographs of Figures 2 and 3. All optical elements and associated electronics following the inner most cylindrical acceleration element float at the acceleration potential which ranges between -8 kilovolts and +8 kilovolts. This can be seen in Figure 2 where the optical support plate stands off from the larger primary support plate and is isolated by ceramic insulators. The wires seen in Figures 2 and 3 exiting from the optical support plate connect to electronics modules which were not included in the assembly at the time the photographs were taken.

Slits S1 and S2 (see Figure 1) are the object and image slits respectively for the magnetic analyzer which is shown schematically in Figure 1 (labeled Magnet) and is seen in Figures 2 and 3 as the gold plated object near the center of each photo. This magnetic analyzer section transmits only those ions with a specific normal component of momentum per unit charge. Slit S2 is also the entrance slit for the electrostatic deflector. The electrostatic deflector deflects the ions upwards out of the plane of the preceeding optical elements and focuses them onto the diagonal upper surface of the deflector. The combined effects of the magnetic analyzer and electrostatic deflector are such as to focus all ions of a given mass per charge, independent of incidence angle, along a horizontal line which is perpendicular to S2. The higher mass per charge ions are focused closest to S2 and the ligher mass per charge ions are focused the farthest from S2. Ions of constant angle of incidence and different mass are focused along a single line radiating outward from a point near S2. Thus, the ions are imaged in two dimensions, mass per charge and angle of incidence.

An image intensifying microchannel plate (MCP) detector is placed in the focal plane of the electrostatic deflector to detect and intensify the signals from the impinging ions while preserving the angle-mass "image". The output signals from the MCP are collected on an anode system which is coupled to an image encoding electronics system via a matrix of low noise charge sensitive preamplifiers. The preamplifier matrix assembly can be seen as three rows of miniature hybridized modules above the electrostatic deflector focal plane in Figure 2 and 3. The output signals from the preamplifiers are carried to the image encoding electronics unit via flexible flat cables (see Figure 4) which connect to the tops of the preamplifier matrix assemblies.

In addition to the MCP detector there are four channel electron multiplier (CEM) detectors positioned at the upper (low mass per charge) end of the electrostatic deflector focal plane. The CEM detectors, which appear in Figures 2 and 3 as black helical structures mounted on ceramic substrates at the top of both photographs, are positioned to intercept hydrogen ions

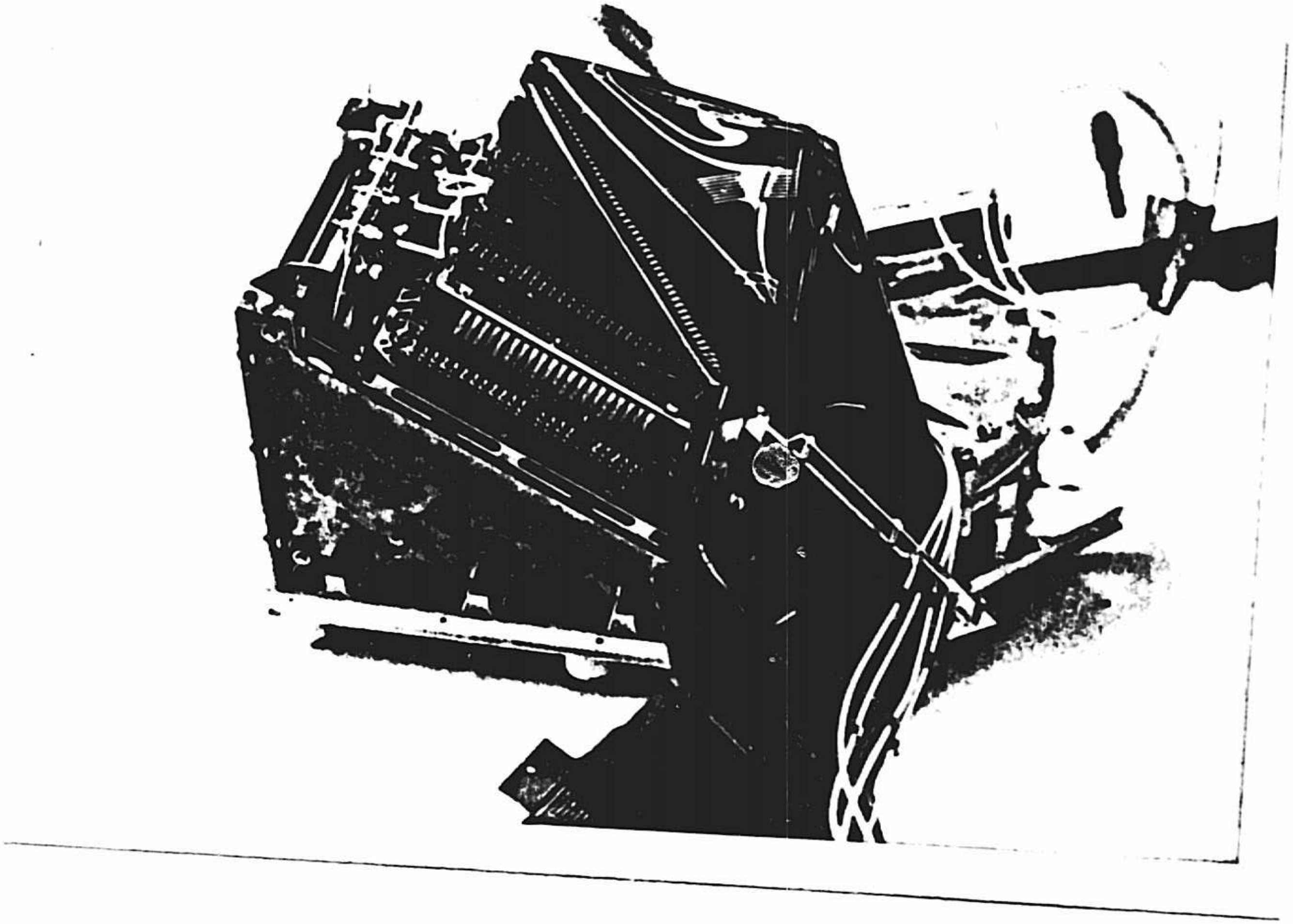

Figure 4. Photograph of the HERS ion optics with the signal cabling connected.

(protons) when the electrostatic deflector voltage is set to focus ions with mass per charge between 2 amu/e ($^4He^{2+}$) and 4 amu/e ($^4He^+$) onto the MCP detector. The CEM detectors are used to handle the higher count rates expected for protons in the solar wind and the interaction region of the comet.

Also evident in the upper right hand quadrant of Figure 3 is the high voltage distribution and filter system for the ion optical elements that float at the acceleration-deceleration potential. The high voltage is generated in a separate module which, in the complete assembly, is mounted in the space to the left of the magnet in Figure 3 where the bundle of wires is taped down to the primary support plate. The high voltages for the MCP, CEM and electrostatic deflector are fed via these wires, which pass through the optical support plate, to the four hermetically sealed high voltage feedthroughs on the right hand side of the optical support plate next to the electrostatic deflector in Figure 3. The filter circuit for the MCP is seen above the feedthroughs.

In the flight configuration, the entire optical system following the accelerator grids, i.e. all elements mounted on the optical support plate, are enclosed within an electrostatic shield. This subassembly is shown in Figure 5. This enclosure protects the critical optical elements from contamination and provides a controlled high potential surface to prevent corona when voltages up to ± 8 kV are applied.

The optical elements as well as the associated electronics modules are contained within the primary honeycomb enclosure. The totally assembled HERS instrument is shown in Figure 6. The entrance aperture (collimator) with its

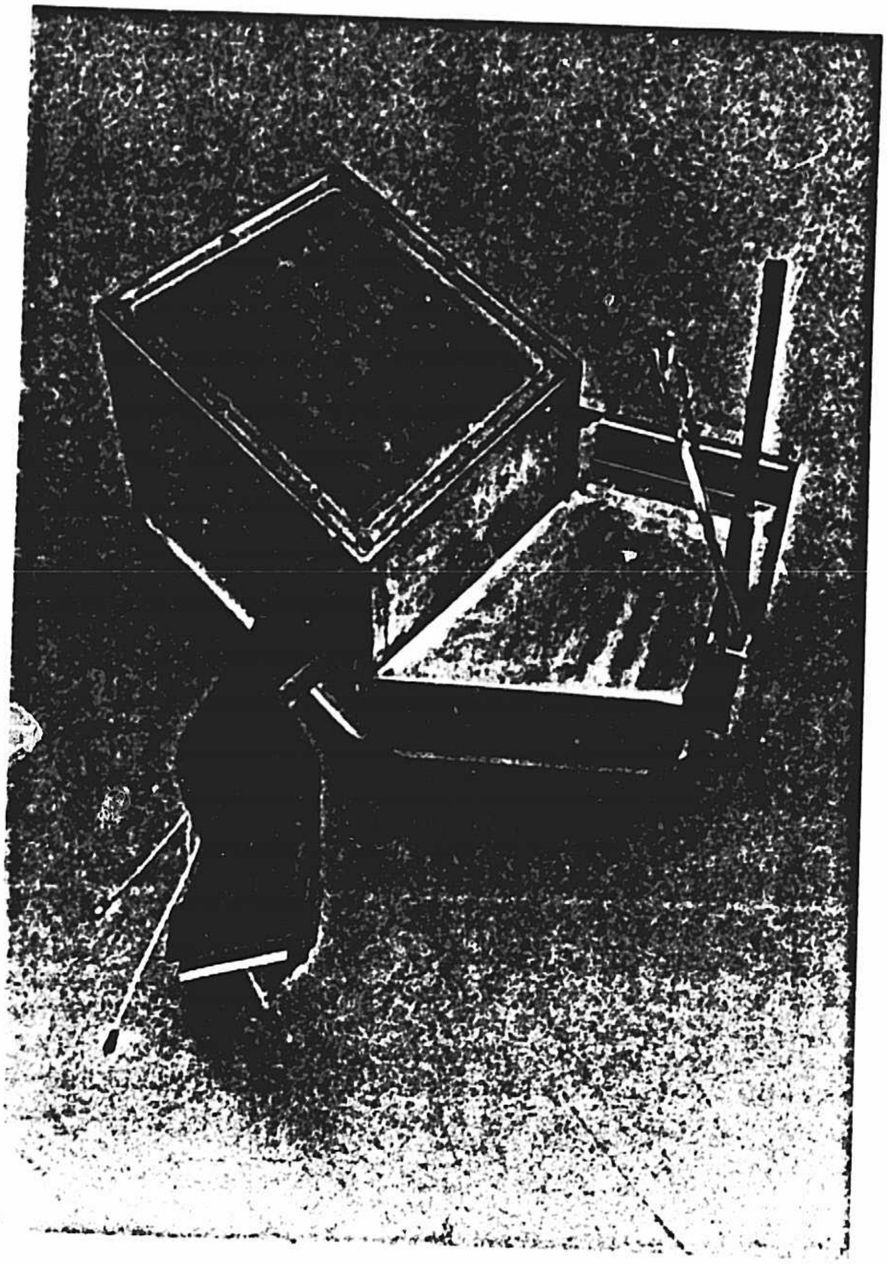

Figure 5. Photograph of the assembled high voltage section of the HERS ion optics with the hermetic cover in place. The signal cabling projects from the left and the high voltage cabling projects upwards.

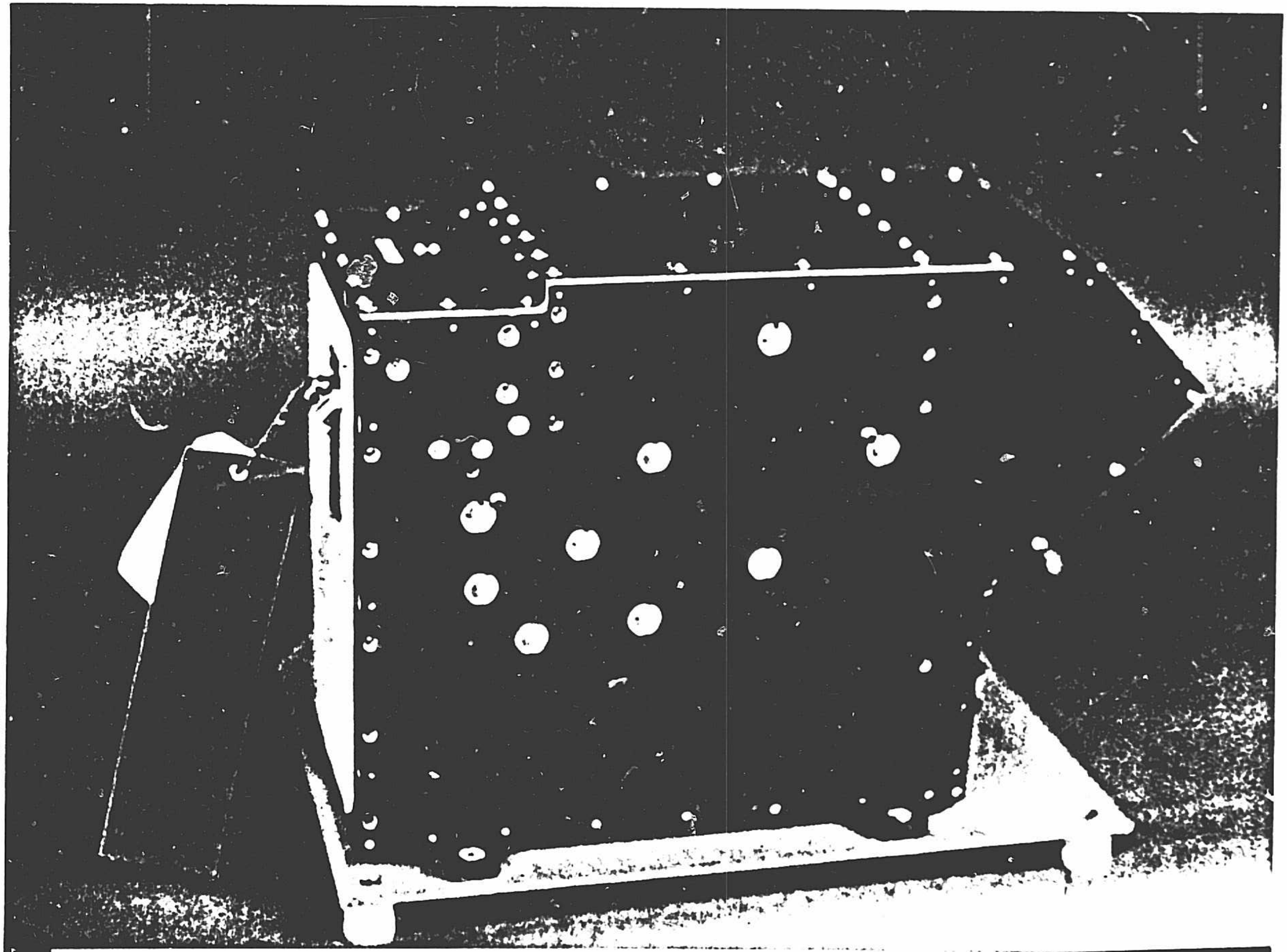

Figure 6. Photograph of the complete HEXS instrument with the non-flight aperture cover installed (see red tag item). The entrance aperture is to the left.

hermetically sealed aperture cover is on the left of the photograph with a red "remove before flight" tag attached. Surrounding the aperture one sees the low emissivity thermal control surfaces which are exposed to the space environment in flight.

2. ION OPTICS

2.1 Collimator

As discussed in the introduction, the external collimator is most visible in Figure 2. The polished collimator housing serves to reflect most of the solar radiation, but is conducting to avoid differential charging which could alter the trajectories of incoming ions. The actual ion beam collimation is accomplished by the black inner rim seen in the collimator opening. This can be visualized more clearly by refering the engineering drawing schematic of the "front end" ion optical elements in Figure 7. This is an engineering drawing, to scale, but with most non-essential details removed.

The key points in the collimator are labeled P1, P2 and P3 in Figure 7. The functions of these points will be more obvious as we discuss the ion trajectories in conjunction with other optical elements. Neglecting the effects of refraction resulting from acceleration or deceleration and the small angle scattering due to various grids, the collimator together with the object slits (S1) and electrode S20 defines the bundle of ion trajectories accepted by the instrument. The collimator also minimizes the access of neutral gasses and solar ultraviolet to the inner portions of the ion optics.

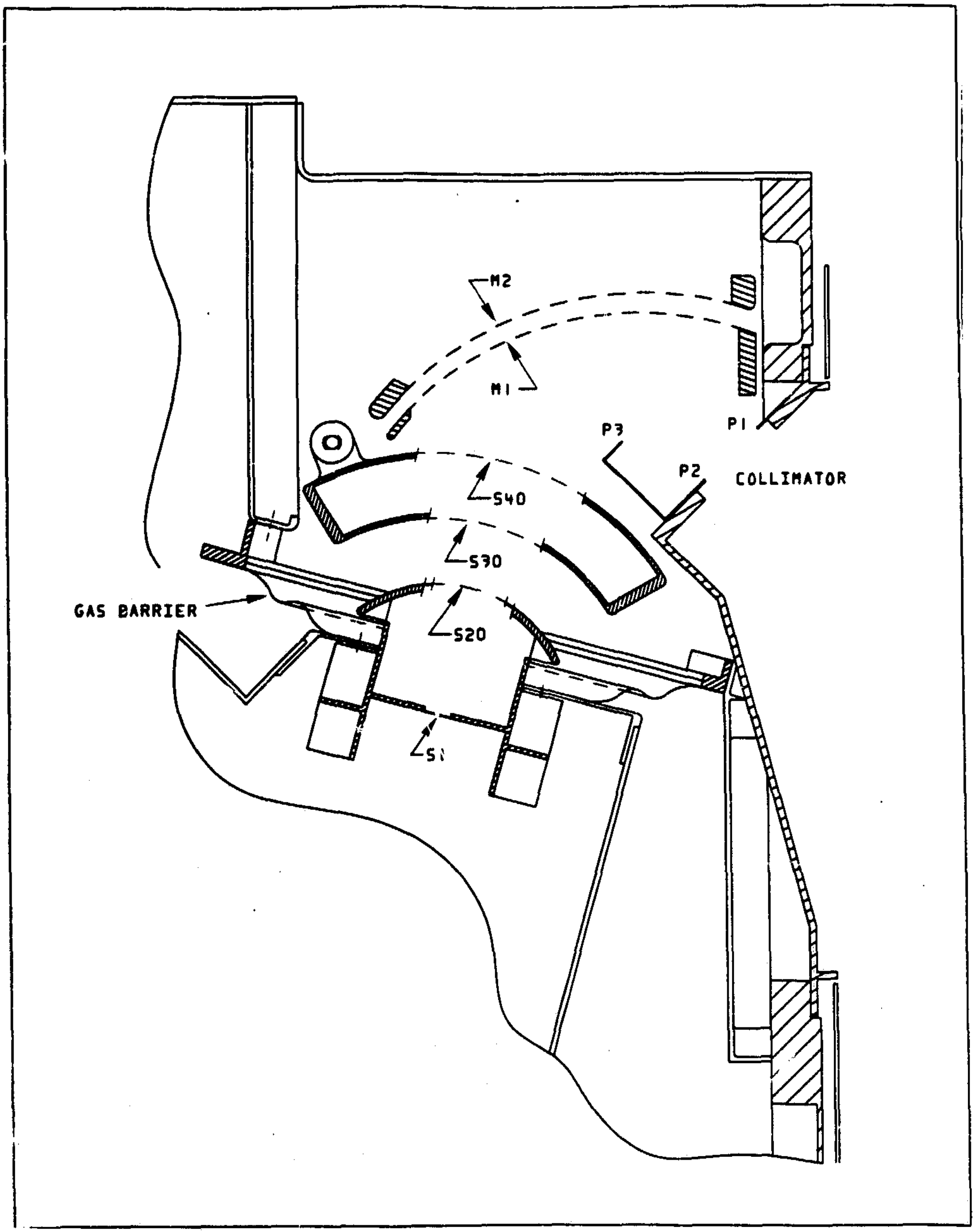

Figure 7. Engineering schematic drawing of the entry region ion optical elements including the collimator, mirror (M1-M2), the ion repeller-accelerator section (S20,S30,S40) and the object slit S1. The high voltage isolation gas barrier completes the hermetic seal around the ion optics elements.

For this purpose the surface of the collimator has been specially treated with a copper oxide process which minimizes ion and photon scattering.

2.2 Mirror

The electrostatic mirror serves two primary functions. It reflects the desired ions into the analysis section of the system while transmitting the undesired photons and neutral gasses and it compresses the large (60°) external field of view into the smaller acceptance angle (30°) of the analysis system.

If we define θ as the angular direction of a particle incident on a reflecting surface and γ as the angular direction of a reflected particle (see Figure 8), than $d\theta/d\gamma = 1$ only for a flat surface. That is only a flat mirror reflects without magnification or distortion. Any curved surface will result in a local angular magnification or demagnification. However, for most simple surfaces such as cylinders $d\theta/d\gamma$ varies over the surface so that the angular magnification is not a constant. As summarized in Figure 8, the requirement for magnification without distortion is that

$$d\theta/d\gamma = \text{constant} = C \qquad (1)$$

or

$$d\theta = C\, d\gamma \qquad (2)$$

GENERAL CASE: OPTICAL REFLECTION
CONSTANT MAGNIFICATION MIRROR

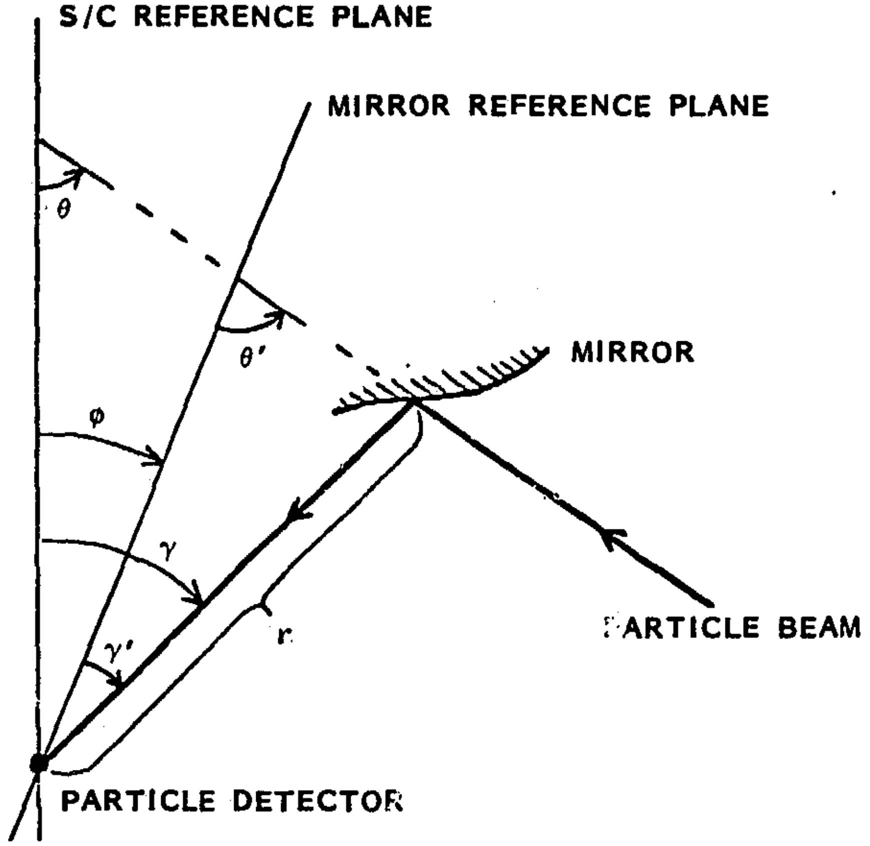

REQUIREMENT: $d\theta/d\gamma = \text{CONSTANT} = C$

$d\theta = d\theta' = Cd\gamma = Cd\gamma'$

RESULT: $r = r_o\left[\cos\left\{\frac{(C+1)}{2}\cdot(\gamma-\phi)\right\}\right]^{-\frac{2}{C+1}}$

$\theta' = C\gamma' = C\ (\gamma-\phi)$

$\theta = \theta' - \phi = C\gamma - \phi\ (C + 1)$

Figure 8. Geometry for the solution of the generalized constant magnification optical mirror problem.

From the geometry it is clear that

$$\theta = \theta' - \phi \tag{3}$$

$$d\theta = d\theta' \tag{4}$$

$$\gamma' = \gamma - \phi \tag{5}$$

$$d\gamma' = d\gamma \tag{6}$$

From (2) (4) and (6)

$$d\theta' = Cd\gamma' \tag{7}$$

solving (7) and substituting (5) leads to the results that

$$\theta' = C\gamma' = C(\gamma-\phi) \tag{8}$$

Furthermore, from (3) and (8),

$$\theta = \theta' - \phi = C\gamma - \phi(C+1). \tag{9}$$

It can be shown that the equation, in cylindrical coordinates (r,γ), for the generalized surface which satisfies equation (9) is given by

$$r = r_o[\cos\{1/2(C+1)(\gamma+\phi)\}^{-\frac{2}{C+1}} \tag{10}$$

The special case for magnification of −2 is shown in Figure 9. The negative sign implies that γ decreases as θ increases and results in a concave

SPECIAL CASE: CONCAVE MIRROR WITH MAGNIFICATION EQUAL TO 2 (C=-2)

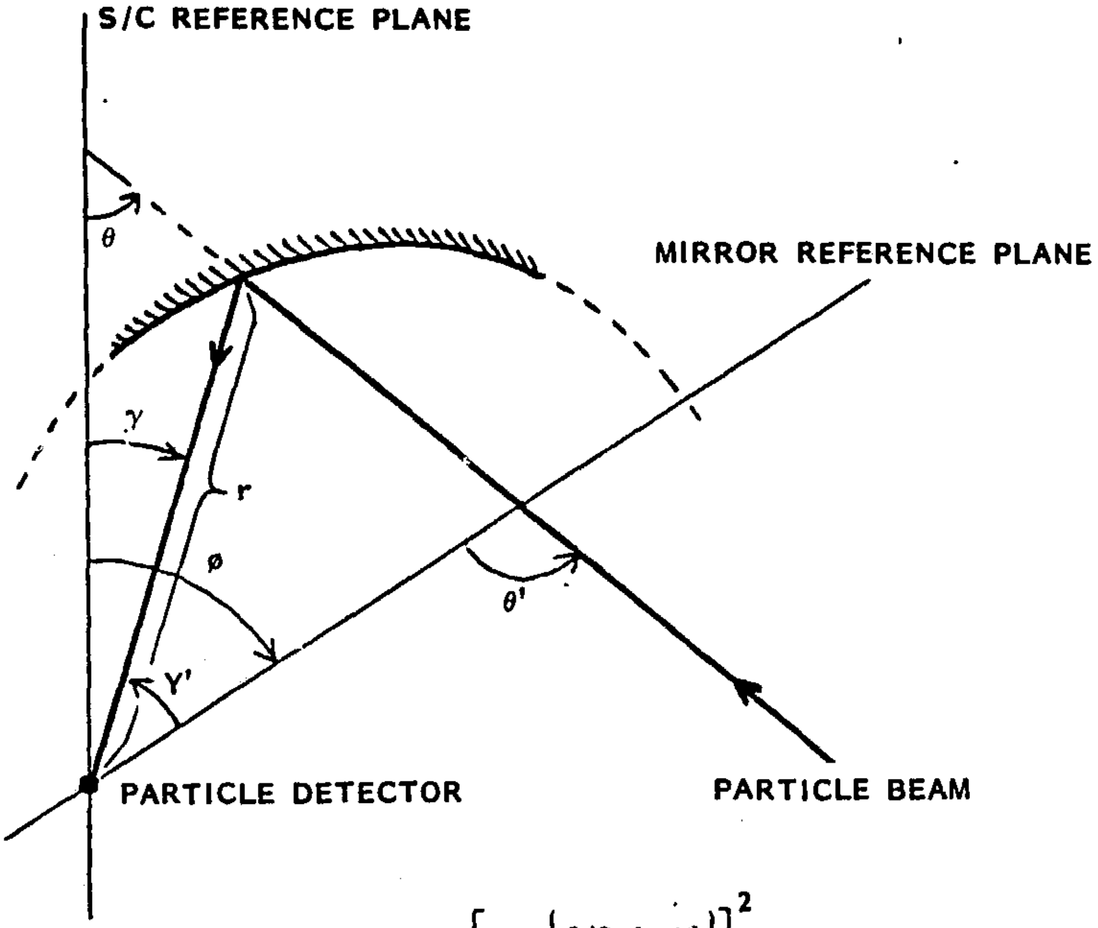

$$r = r_o \left[\cos\left\{1/2\ (\phi-\gamma)\right\}\right]^2$$

$$\theta' = -2\gamma' = 2\ (\phi-\gamma)$$

$$\theta = \theta' - \phi = \phi - 2\gamma$$

Figure 9. Geometry for the special case optical mirror with magnification of -2.

mirror geometry as opposed to a convex mirror with the same absolute magnification. The concave geometry was chosen so that the ion trajectories would cross over outside the mirror allowing the size of the opening in the instrument to be minimized.

The above equations and the geometries shown in Figures 8 and 9 assume impulse reflection of light from a polished metal surface. Practical limitations on electric field intensities in an electrostatic mirror (a few kilovolts per millimeter) result in the condition that the turning radii of the ions in the field are not truly negligible in comparison to the radius of the mirror. Thus the separation of the two electrodes in the mirror is not negligible in comparison with the radius of curvature of the surface. In the process of reflecting in a finite field, the ions propogate tangentially to the mirror surface. The distance traveled, and thus the orientation of the surface at the exit point, varies with the depth of penetration into the field. The latter is directly proportional to the ratio of the normal component of the ion energy per charge to the retarding potential applied to the second electrode. The net effect is that there is not a unique, one-to-one, relationship between the incident and reflected trajectories of the ions. Figure 10 shows a computer generated pair of electrodes satisfying the exact surface configuration of Figure 9 but oriented so as to minimize the variability of reflection angle versus incidence angle over the full 30° range of reflected angles. In this geometry the surface M1 is held at ground potential and a retarding potential is applied to surface M2. Actual ion trajectories will be shown in Figures 19 through 21.

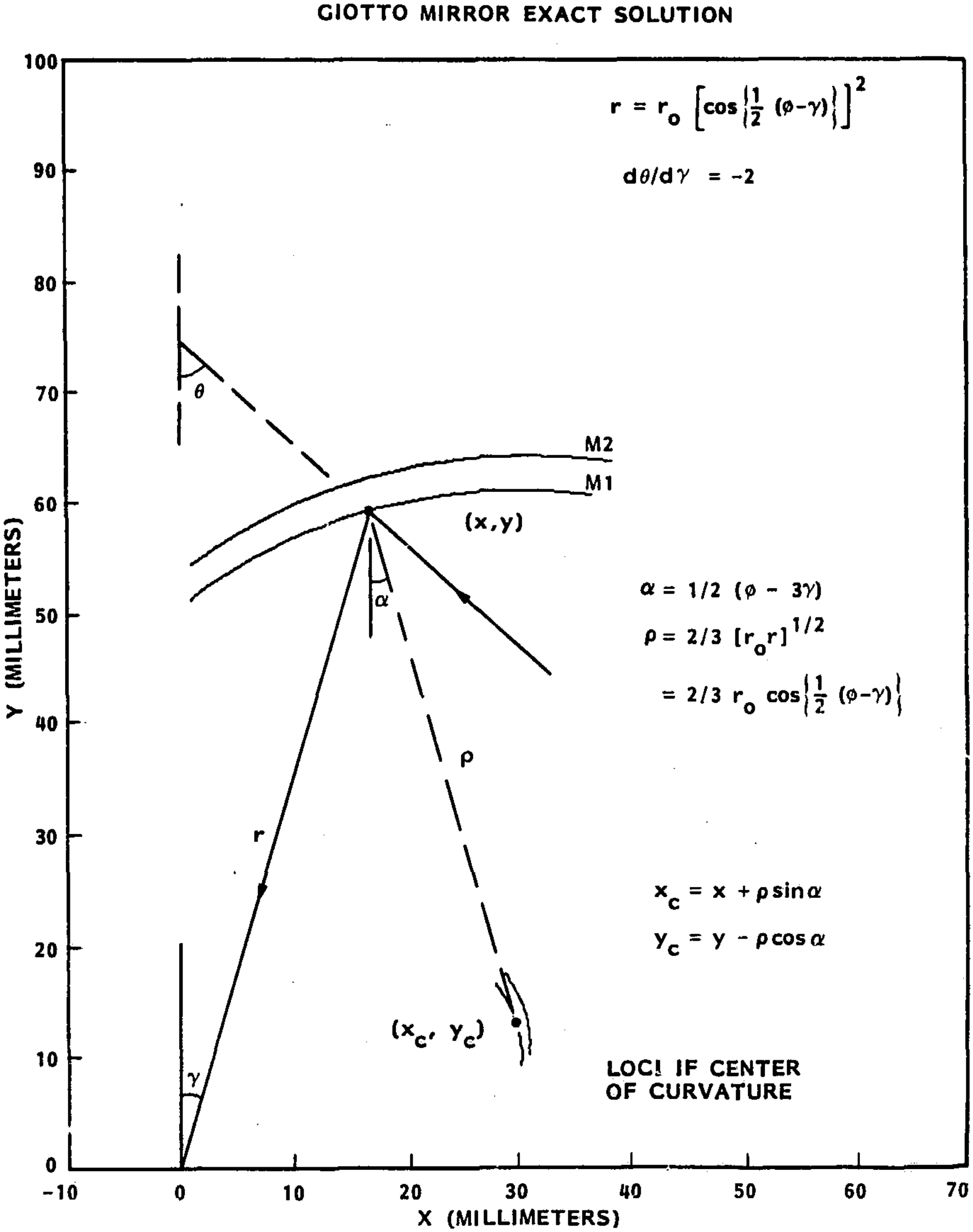

Figure 10. Exact solution for the idealized electrostatic mirror with a constant magnification of -2.

Mirror surfaces of the type shown in Figure 10 are optimum, but due to their complex shapes (see the equations in Figures 9 and 10) they would be very difficult and expensive to fabricate. For that reason we investigated the degree of distortion that would result from the use of cylindrical surfaces which approximated the idealized surfaces over the angular range of interest. As one could anticipate, the degree of local distortion, that is the variability of the reflected angle γ for a given incident angle θ, is not significantly worse for cylindrical surfaces than for the idealized surfaces. This simply reflects the fact that the radius of curvature for the idealized surfaces is not a strong function of angle. For the idealized surfaces of Figure 10, the magnification ($d\theta/d\gamma$) is independent of θ for all ions of a fixed penetration depth F, where F is defined as

$$F = \frac{E_{\perp}}{qV} = \frac{mv^2\cos^2\theta}{2qV} \tag{11}$$

and m is the ion mass, v is the ion velocity, q is the ion charge and V is the potential on M2.

One of our criteria for the quality of approximated surface shapes was the variability of the angular magnification over the angular range of interest ($\Delta\theta = 60^{\circ}$). Figures 11 and 13 show two sets of non-concentric cylindrical surfaces which were selected to approximate the surfaces of Figure 10. For CASE A, Figure 11, cylinders were selected which best matched the idealized surfaces near their respective center points. This required that the centers of curvature for the cylinders lie on the loci of center of curvature from Figure 10. The resultant surface parameters are shown in

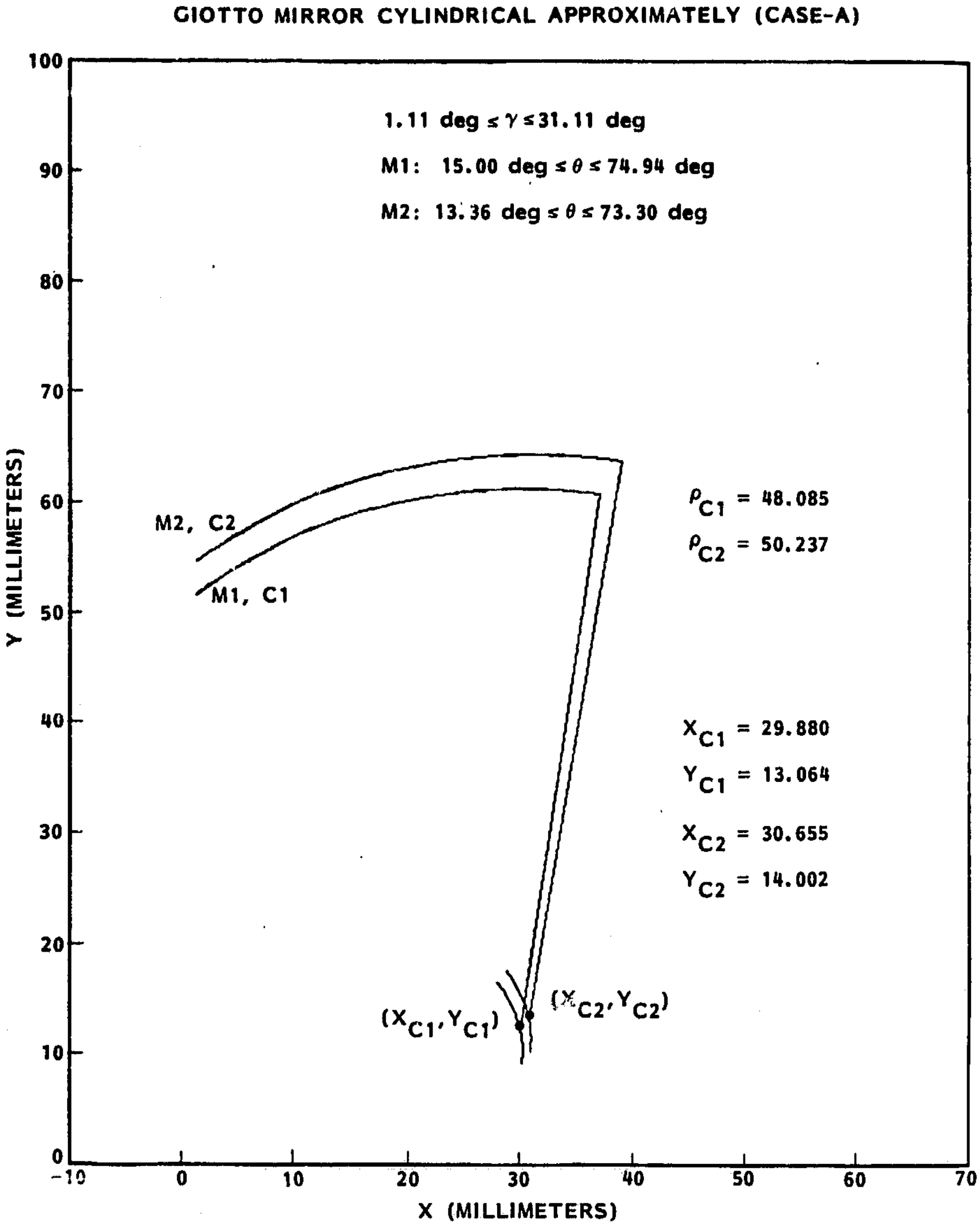

Figure 11. CASE-A cylindrical approximation to electrostatic mirror with magnification of -2. This approximation matches the idealized geometry in the central portion of the mirror.

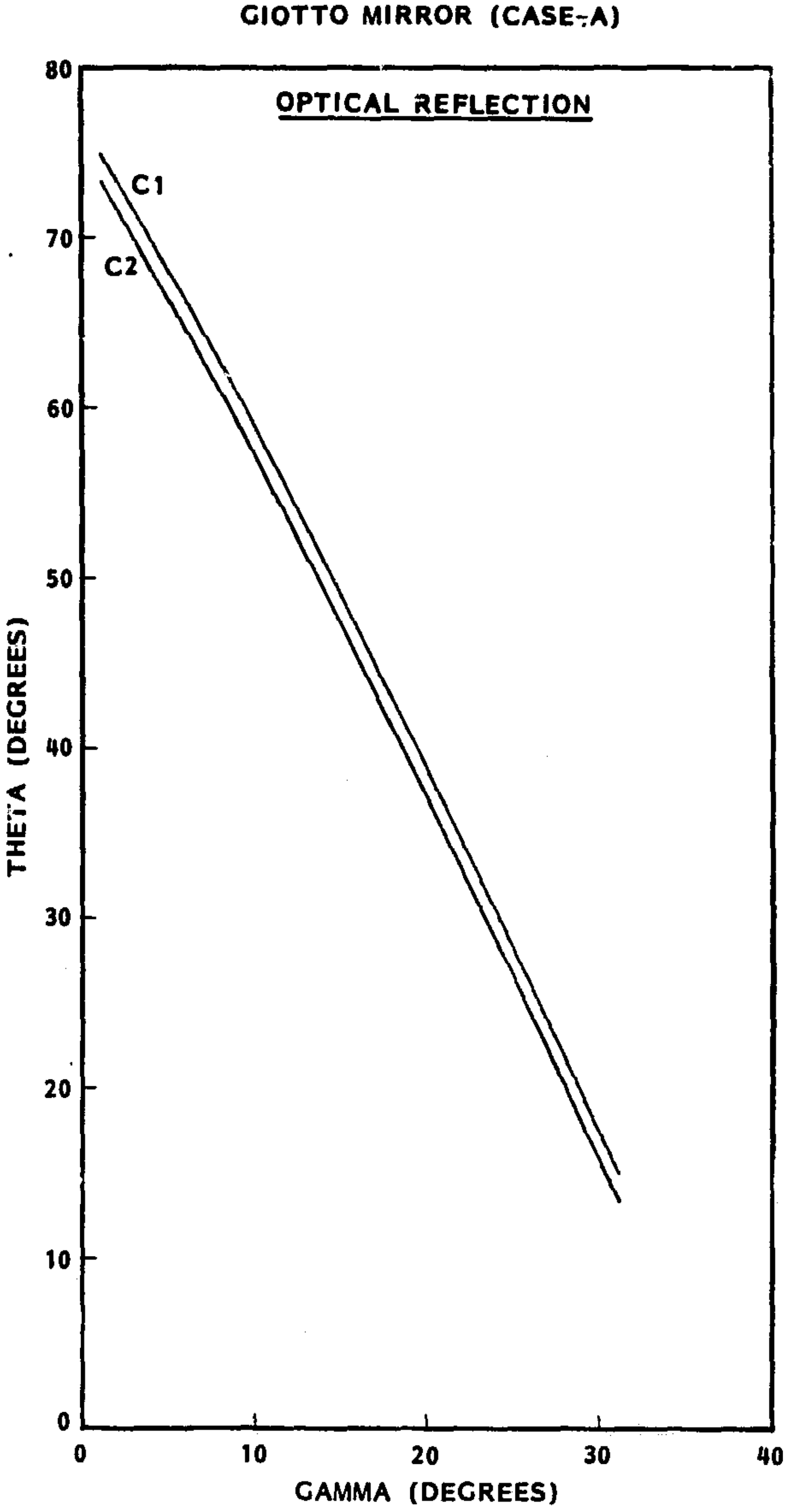

Figure 12. Optical reflection for the two surfaces of the mirror in Figure 11. Constant magnification would produce straight lines.

Figure 11. Figure 12 shows the relationship between incident angles θ and reflected angles γ for ions reflected near the front surface C1 and the back surface C2 for CASE-A. The fact that the curves, labeled C1 and C2 respectively in Figure 12, are not straight lines with a slope of -2 shows the magnification is not constant at the value of the idealized surfaces. However, the magnification varies only slightly over the 60° range of interest.

A better approximation to the idealized surface properties (CASE-B) was achieved by selecting cylindrical surfaces which coincided with the idealized surfaces at both extremes and the center. The resultant surfaces and corresponding cylinder parameters are shown in Figure 13. In this case the cylindrical surface centers of curvature are not constrained to lie on the loci of the centers of curvature for the idealized surface, but are determined by passing a circle through the three points (x_1, y_1; x_2, y_2,; x_3, y_3) on the idealized surface. These points for surface M1 are identified in Figure 13. Within the resolution of the figure it is not obvious that the cylindrical centers (X_{C1}, Y_{C1}) and (X_{C2}, Y_{C2}) do not fall on the respective loci of centers for the respective surfaces M1 and M2. The resultant magnification curves for CASE-B are shown in Figure 14. Again, there is some deviation from a straight line, but the deviation is slightly less than was the case in Figure 11.

Other cylindrical approximations were investigated but none proved to be significantly superior to CASE-B and the latter was selected for fabrication.

All of the calculations presented above assumed homogeneous potential surfaces for M1 and M2. In actuality the only practical method of imposing

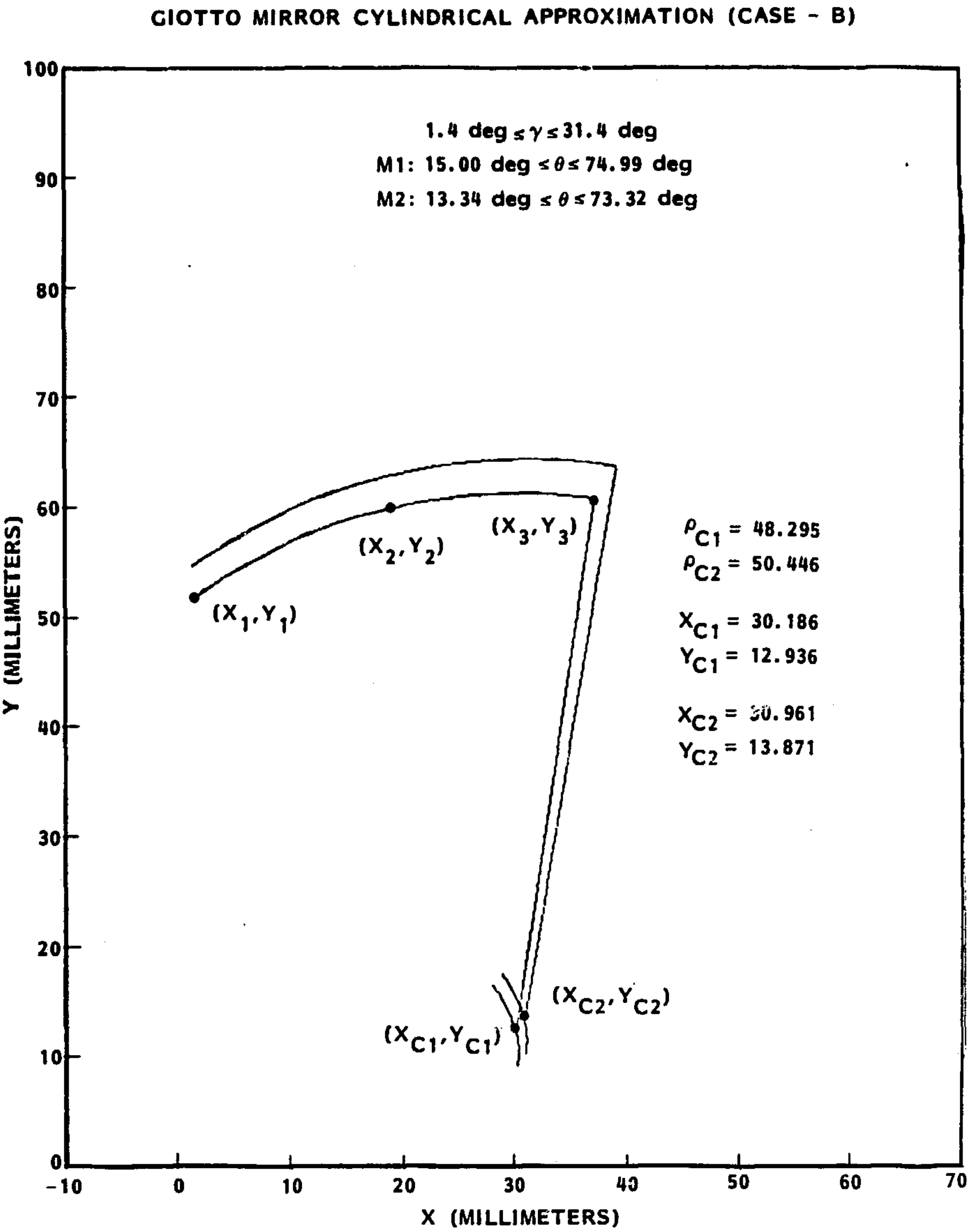

Figure 13. CASE-B cylindrical approximation to the idealized electrostatic mirror of Figure 10. This approximation matches the exact solution at three points on each surface.

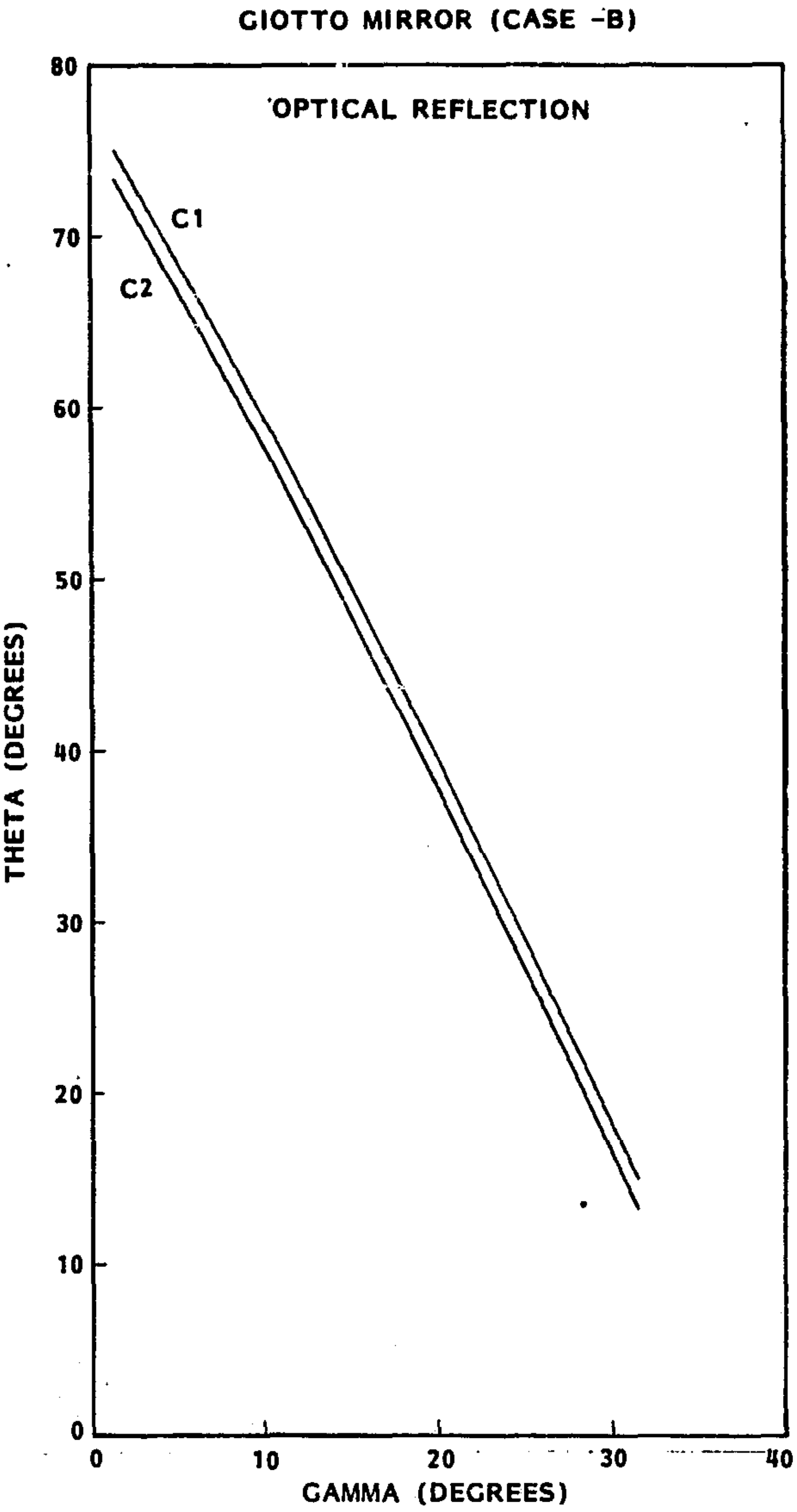

Figure 14. Optical reflection characteristics from the two surfaces of the CASE-B cylindrical mirror.

equal potentials on surfaces which are transparent to low energy ions is to use high transmission metal mesh material which is formed to the desired shape, in this case cylindrical. Since the potential is applied only on the "wires" of the mesh, the potential is not constant across the gap between wires. The result is that equal potential surfaces bulge out in the gaps forming small pincushion-like structures. Thus the electric field is significantly distorted near each wire and the local forces acting on an ion depend on where it enters the mirror relative to the wire locations. Figure 15 shows some typical computer generated trajectories of ions for mesh geometries simulating those actually used in the HERS mirror. In fact the computer simulation uses a one-dimensional mesh which has the wire spacing adjusted to approximate the effects of the actual two-dimensional mesh (per Hanson et al., JGR 77, 1914, 1972). The ions approach the mesh from the lower left corner with the same energy and parallel trajectories. Those passing nearest to a wire experience the greatest perturbation and some ions actually strike a wire and are lost. The remaining ions reflect at different depths since the perturbation changes their directions and thus alters their normal component of energy (see Equation 11 above). After reflection the ion trajectories again pass through the mesh and experience a second perturbation. Note that the ions exiting to the lower right are no longer parallel.

As one might expect, the ions which reflect nearest to the mesh experience the greatest perturbation since their energy is smallest compared to the mirror potentials and thus the perturbing forces. The perturbation also depends on the angle of incidence(θ). In order to quantitatively assess the degree of angular diffusion resulting from the grid wire perturbations, several hundred ion trajectories were calculated for different angles of

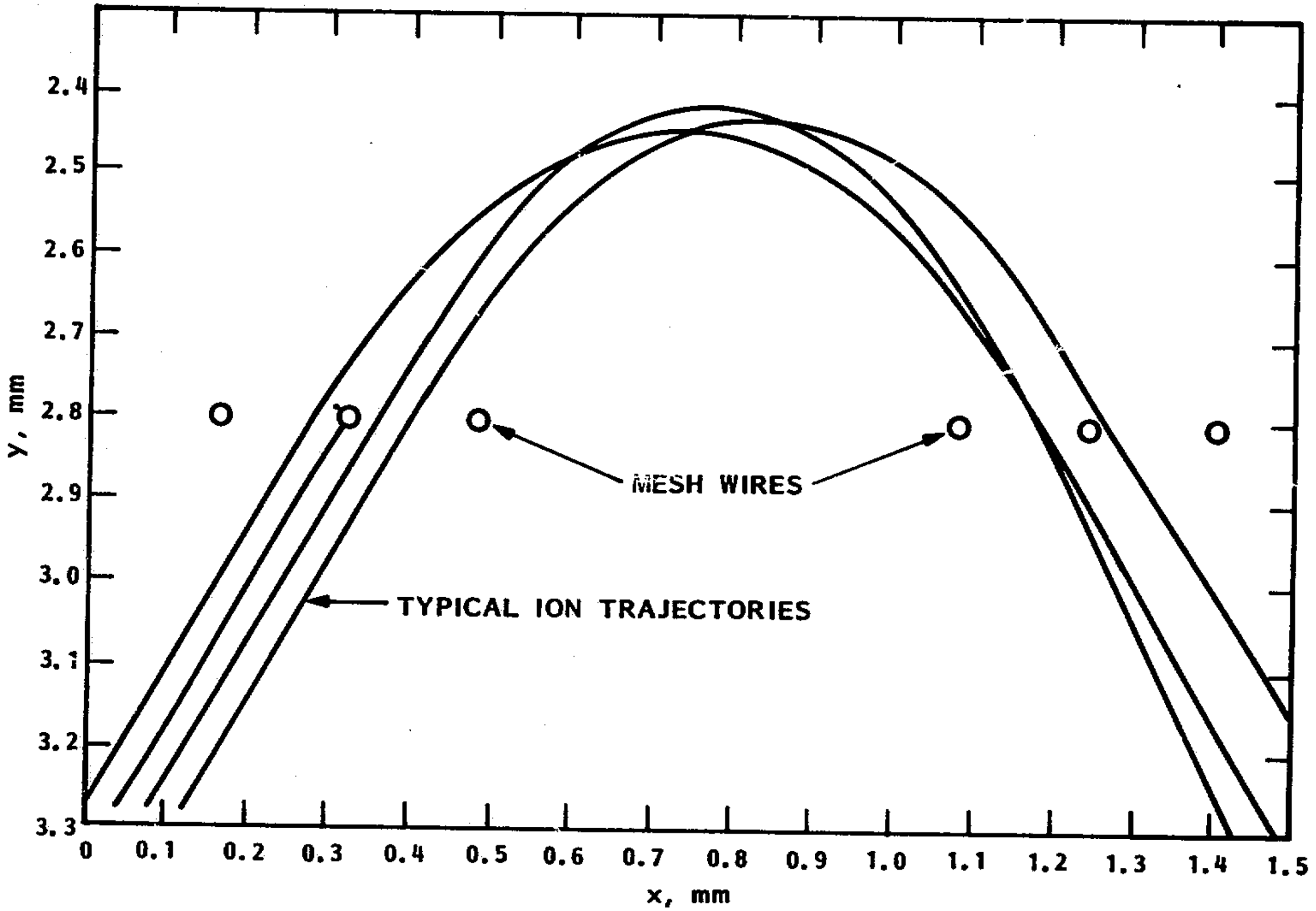

Figure 15. Angular perturbations of ion trajectories from non-uniform potential along a wire mesh surface.

incidence (θ), different penetration depths F (see Equation 11) and varying positions of incidence relative to the wires. Some typical results are shown in Figure 16 for two different F values (0.1 and 0.3) and two different angles of incidence (0° and 30°). Note that the angular scales are not constant. The average value of the absolute variation from the mean value is shown above each histogram. These values quantitatively verify our qualitative arguments that the degree of perturbation depends strongly on the depth of penetration. For $\theta = 0^\circ$, $\langle|\phi|\rangle$ is three times greater for F = 0.1 than for F = 0.3. Similarly, for $\theta = 30^\circ$ the ratio is approximately 3.4. On the other hand, for a constant F value the perturbation decreases with increased angle of incidence relative to the normal. This reflects the fact that for a constant penetration depth the total ion energy is minimum at normal incidence.

A finer mesh size results in a smaller angular diffusion, but for practical reasons this generally results in a lower total transmission which would reduce the overall instrument sensitivity. The tradeoff studies led to the selection of 80% transmission grids with 0.001 inch wire and 100 lines per inch.

Figure 17 shows the fixtures used to attach the high transmission mesh to the cylindrical mirror frames. This somewhat elaborate fixturing was required in order to insure that the mesh remained taunt and smooth. Any irregularity in the mirror surface would lead to ion relfections with distortions similiar to what is seen when looking at optical reflections from an irregular mirror such as one finds in a fun house. The mirror frames and the mirror mesh are both fabricated from beryllium-copper to minimize thermal mismatches which could results in varying mirror distortions as a function of temperature.

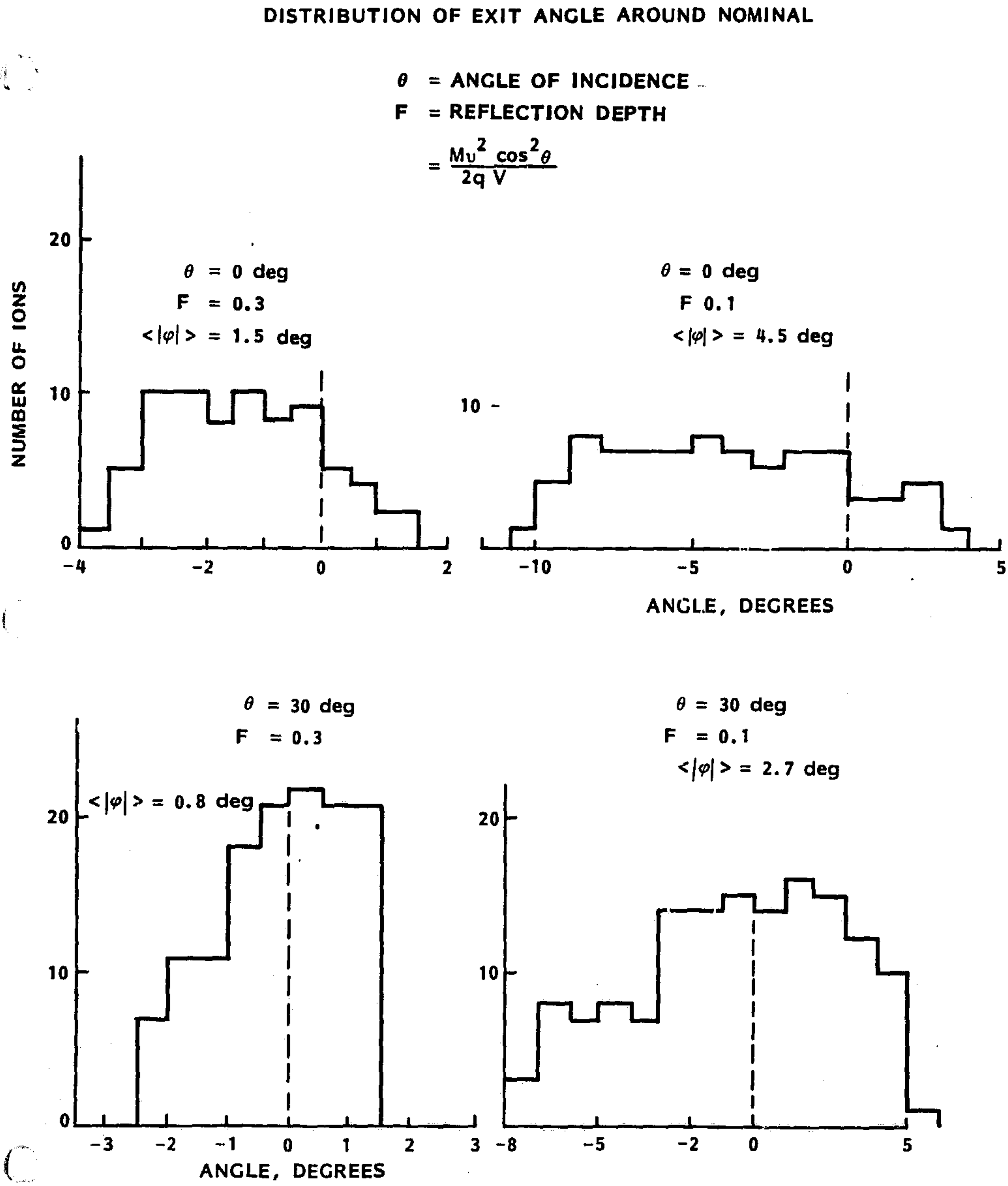

Figure 16. Typical distributions of exit angles from an electrostatic mirror for a given input angle and ion energy. Spread in exit angles results from non-uniform potential at wire mesh surface. Note variations in horizontal scales.

ORIGINAL PAGE IS
OF POOR QUALITY

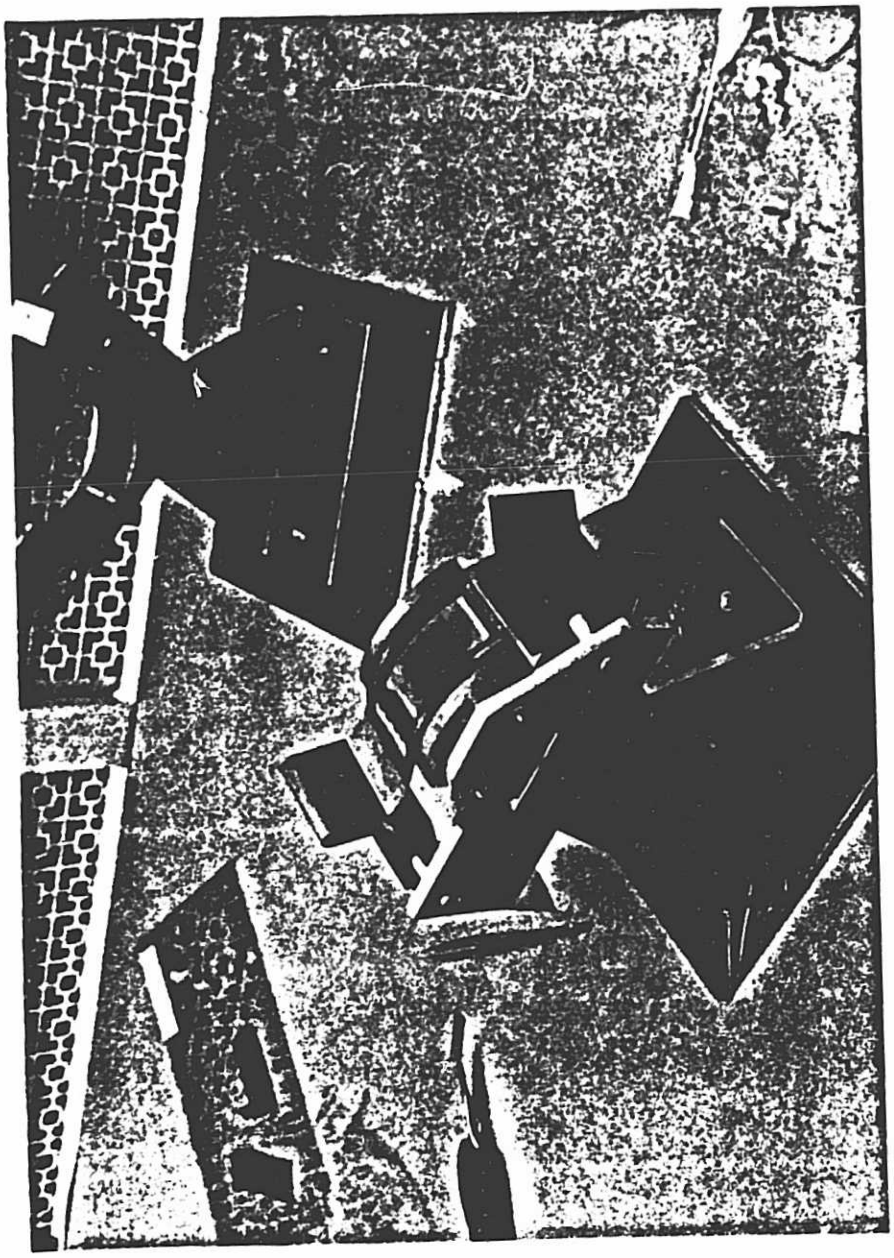

Figure 17. Photograph of fixtures required to mount the flat grid material onto the curved electrostatic mirror surfaces.

A photograph of a completely assembled mirror system is shown in Figure 18. The mirror is being viewed from the back or M2 side. Note the ceramic insulating supports under the M2 element. Voltages as high as 8,000 volts must be applied to the M2 element to reflect the maximum energy ions analyzed. The mirror potential is programmed to be approximately proportional to the accelerating potential so that most ions of interest are reflected at a penetation depth (F) near 0.5 to minimize angular diffusion (see Figure 16). Under some conditions the penetration varies between 0.1 and 0.9 depending on mass, angle of incidence and energy. This is shown for a few specific cases in Figures 19-21. These will be discussed in more detail in conjunction with the accelerator section.

2.3 Accelerator Section

Refering back to Figure 7, the accelerator section consists of a set of three concentric, cylindrical, gridded electrodes. These are identified by their respective radii in millimeters as S20, S30 and S40. As discussed in the introduction, the ion optical elements starting with the object slit (S1) operate at a fixed normal component of momentum per unit charge. This is determined by the radius of curvature, as defined by the object and image slits, S1 and S2 respectively, and field strength of the permanent magnet momentum analyzer. In order to analyze ions with other values of momentum the ions are appropriately accelerated or decelerated prior to the analysis. This is accomplished by applying negative or positive potentials of up to 8,000 Volts to the analysis system. This potential is applied to the gap between S20 and S30 in Figure 7.

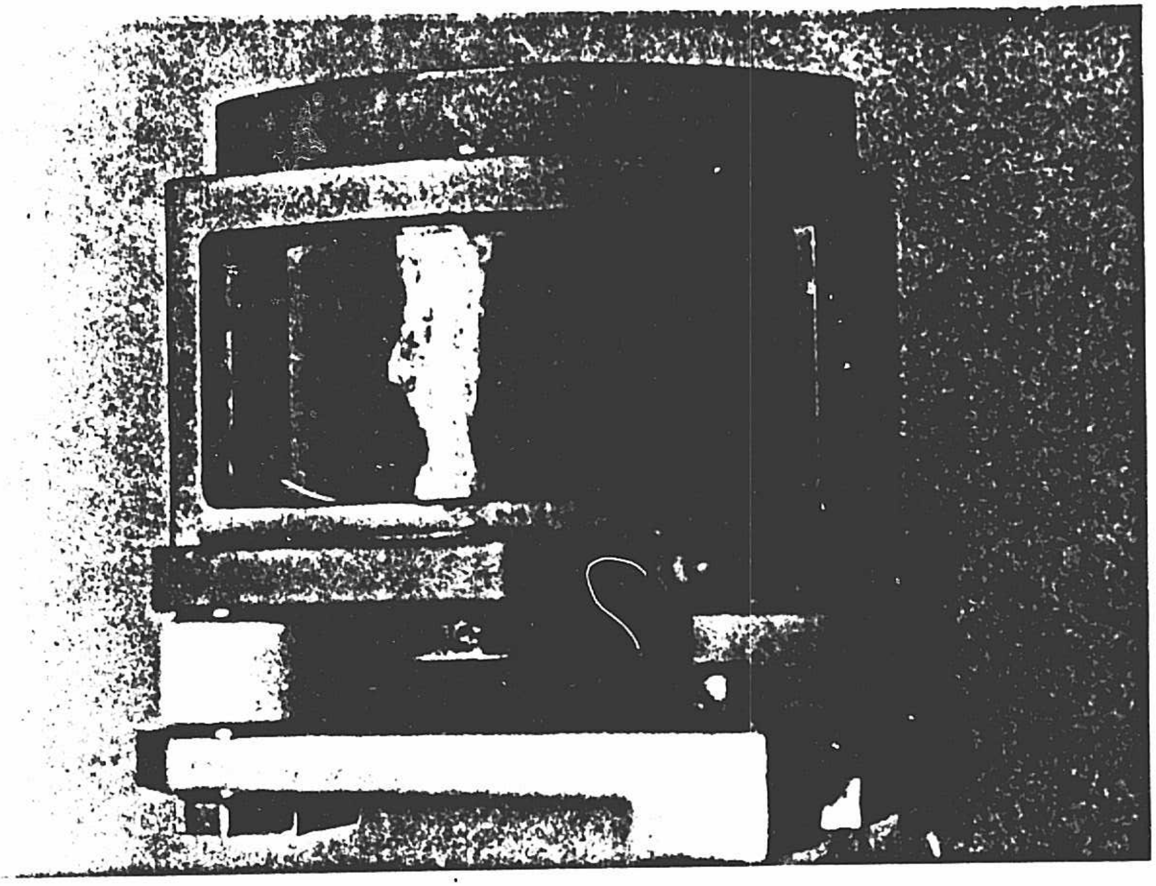

Figure 18. Complete HERS electrostatic mirror assembly with mirror grid surfaces mounted.

For an infinitesimal slit width S1 and perfectly homogeneous potential surfaces at S20 and S30, all ions of interest would be traveling radially in the plane of Figure 7. Thus, to first order, the use of cylindrical electrodes rather than flat electrodes eliminates ion trajectory refraction in one dimension. This is very important in a system that has a large acceptance angle since

$$E_o \sin^2\theta_o = (E_o - qV)\sin^2\theta_1 \tag{12}$$

where E_o is the initial energy of the ion, θ_o is the angle of incidence measured from the surface normal, q is the ion charge, V is the potential through which the ion is accelerated and θ_1 is the angle of exit relative to th surface normal. This equation is strictly true only for an impulsive acceleration, but it is a good approximation for acceleration by finite electric fields. This effect is referred to as a refraction since it is the equivalent of optical refraction when light rays pass through the interface between materials of different indices of refraction. In our case, by making the equapotential surfces cylindrical, θ_o and θ_1 are minimized. Obviously as θ_o approaches zero the effect goes to zero. The fact that the analyzer accepts only a very small range of angles ($\approx 1^o$) in the plane normal to Figure 7 means that the refraction is generally less important in that dimension.

The finite dimensions of S1 ($\approx$ 1 mm) relative to the 20 mm radius of S20 results in some refraction. This is maximum for low energy hydrogen which must be accelerated before analysis. This is illustrated in Figure 19 which is a computer generated plot of hydrogen ion trajectories for the actual

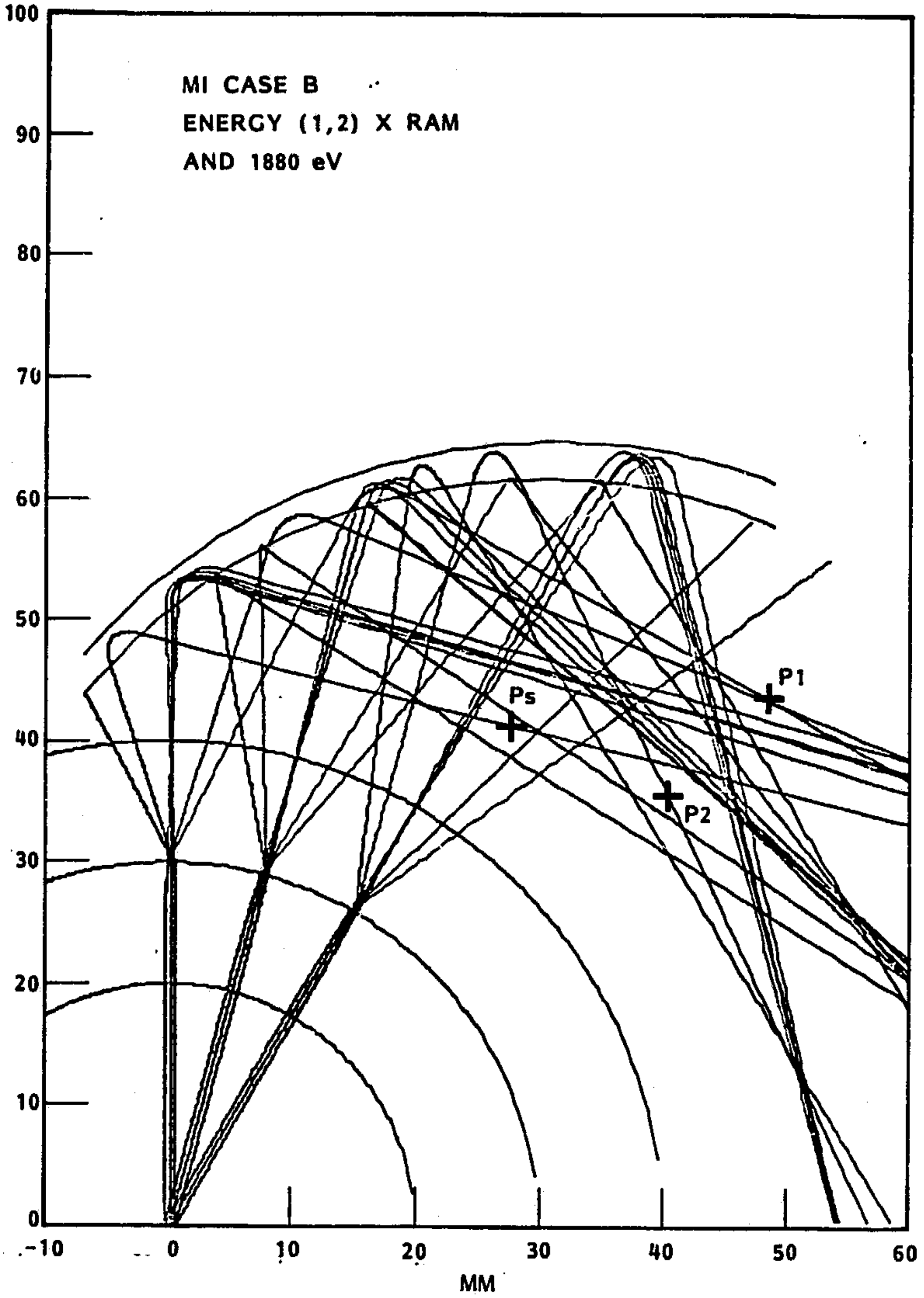

Figure 19. Computer simulated ion trajectories for low energy hydrogen ions. Simulation includes the electrostatic mirror and acceleration region with finite S1 slit width but does not include angular diffusion due to the grids. P1, P2 and P3 represent collimator limits (See Figure 7).

mirror geometry and accounting for the finite S1 slit width. Points P1, P2 and P3 correspond to similarly labeled points on the collimator in Figure 7. In this plot ions are traced backwards from S1 for energies corresponding to the upper, middle and lower limit of the magnet transmission, for angles at both extremes and in the middle of the angular acceptance and for three positions on S1. This figure was selected to illustrate several undesirable but unavoidable effects in electrostatic ion optics which result from the necessity to use acceleration potentials which are large compared with initial ion energies. The refraction, which occurs very near S30, results in a mixing of internal angles relative to incident external angles. This effect is limited by the entrance collimator. Any ray which intercepts a line between P2 and P3 or falls outside the line between P1 and P2 is lost. Also those ions which do not intercept the finite dimensions of the mirror are lost.

Figure 19 also demonstrates the variability of the penetration depth of ions into the mirror reflecting region. As we discussed previously in conjunction with Figure 16, the angular diffusion resulting from the mirror electrode mesh wires is dependent on both the angle of incidence and the depth of penetration. This diffusive effect was not included in the trajectory calculations of this figure.

Figures 20 and 21 demonstrate the more typical case for the HERS system where the relative accelerating potentials are progressively reduced relative to those for Figure 19. For relatively low energy ions with mass per charge 4 (e.g. $^4He^+$), some refraction occurs and the ions are reflected very near the front surface of the mirror; however, one sees that the incident trajectories

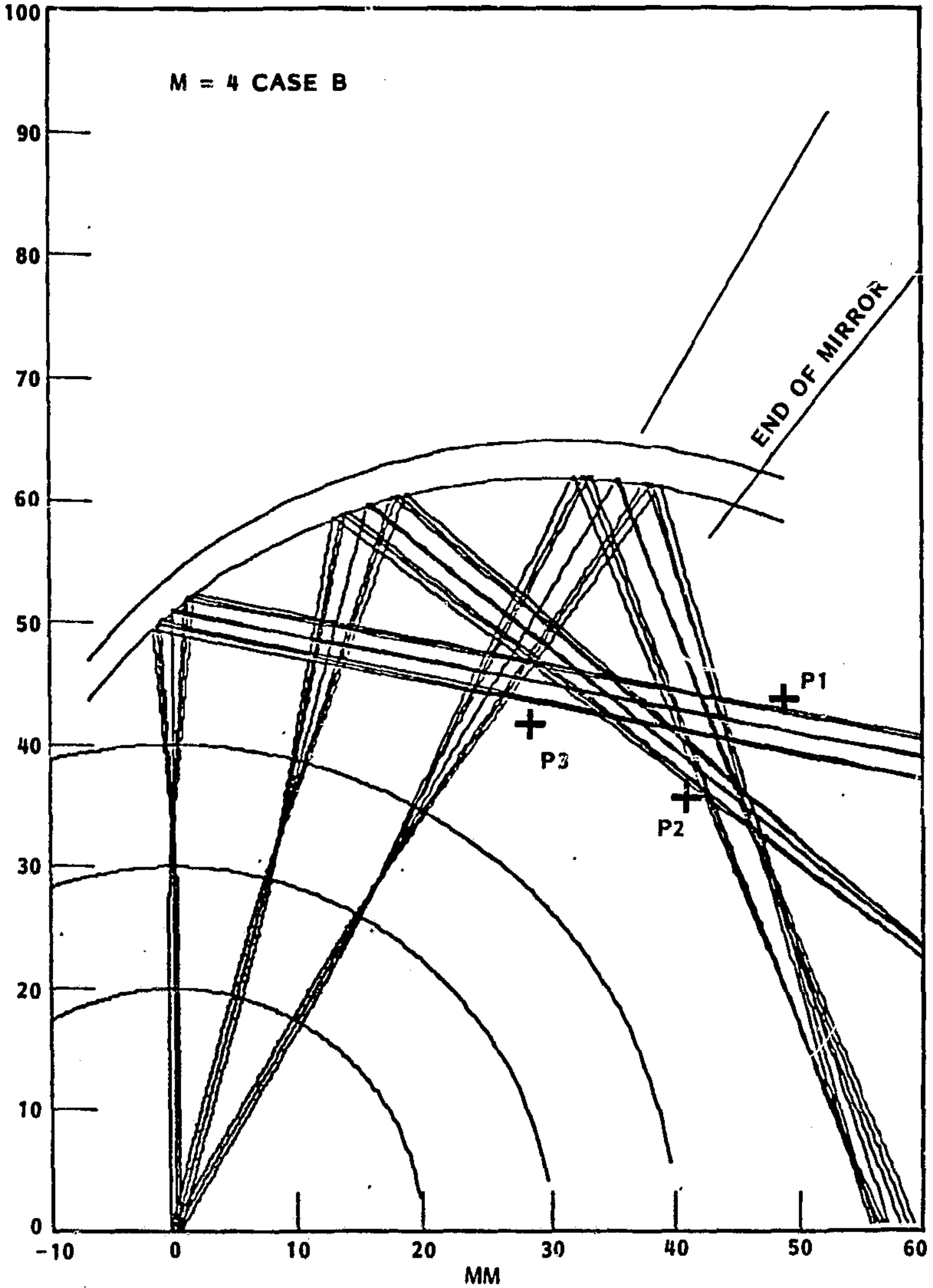

Figure 20. Similar to Figure 19, but for ions with mass per charge of 4 amu/e.

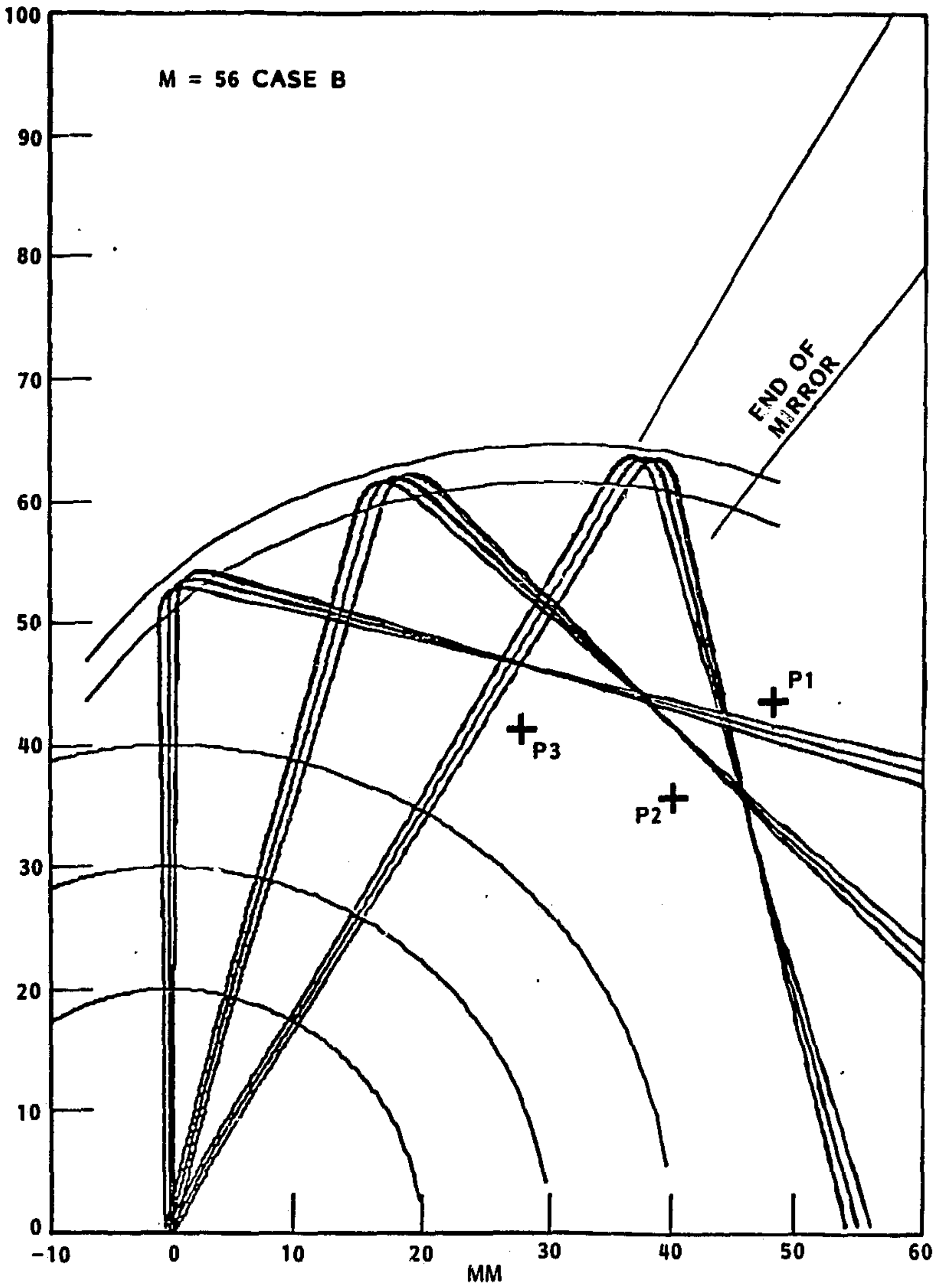

Figure 21. Similar to Figure 19, but for ions with mass per charge of 56 amu/e.

for a given internal angle are nearly parallel. We also note that all ions intercept the mirror and none fall outside the collimator.

For heavy ions (M = 56) of moderate energy where very little acceleration or deceleration is required and the ions reflect very near a penetration depth of 0.5 in the mirror (see Figure 21) the ray bundles remain very compact as they traverse the various optical elements. As with the trajectories shown in Figure 20, the external collimator does not limit the rays. Without significant refraction the rays are limited by the finite opening is S20 (see Figure 7).

Deep within the coma of the comet, it is anticipated that the GIOTTO spacecraft will be enveloped in a high density of low energy ions as a result of interactions with the neutral gas and dust of the comet. An unknown, but possibly significant, flux of the low energy ions could find their way into the HERS aperture. If the ions were accelerated into the magnet region they could be confused with the ambient ions. The use of two outer grids S30 and S40 minimizes the penetration of the accelerating field into the collimator region where the low energy ions would enter. To further reduce the possibility of the ions reaching the inner optical system, S30 and S40 are operated at a slight positive potential (≈ +10 Volts) relative to spacecraft ground. This potential acts to repel the ions away from the acceleration region.

2.4 Magnetic Analyzer

Figure 22 shows the focal properties of a sector magnet for large angles of incidence. It is well known that for parallel rays a sector magnet will

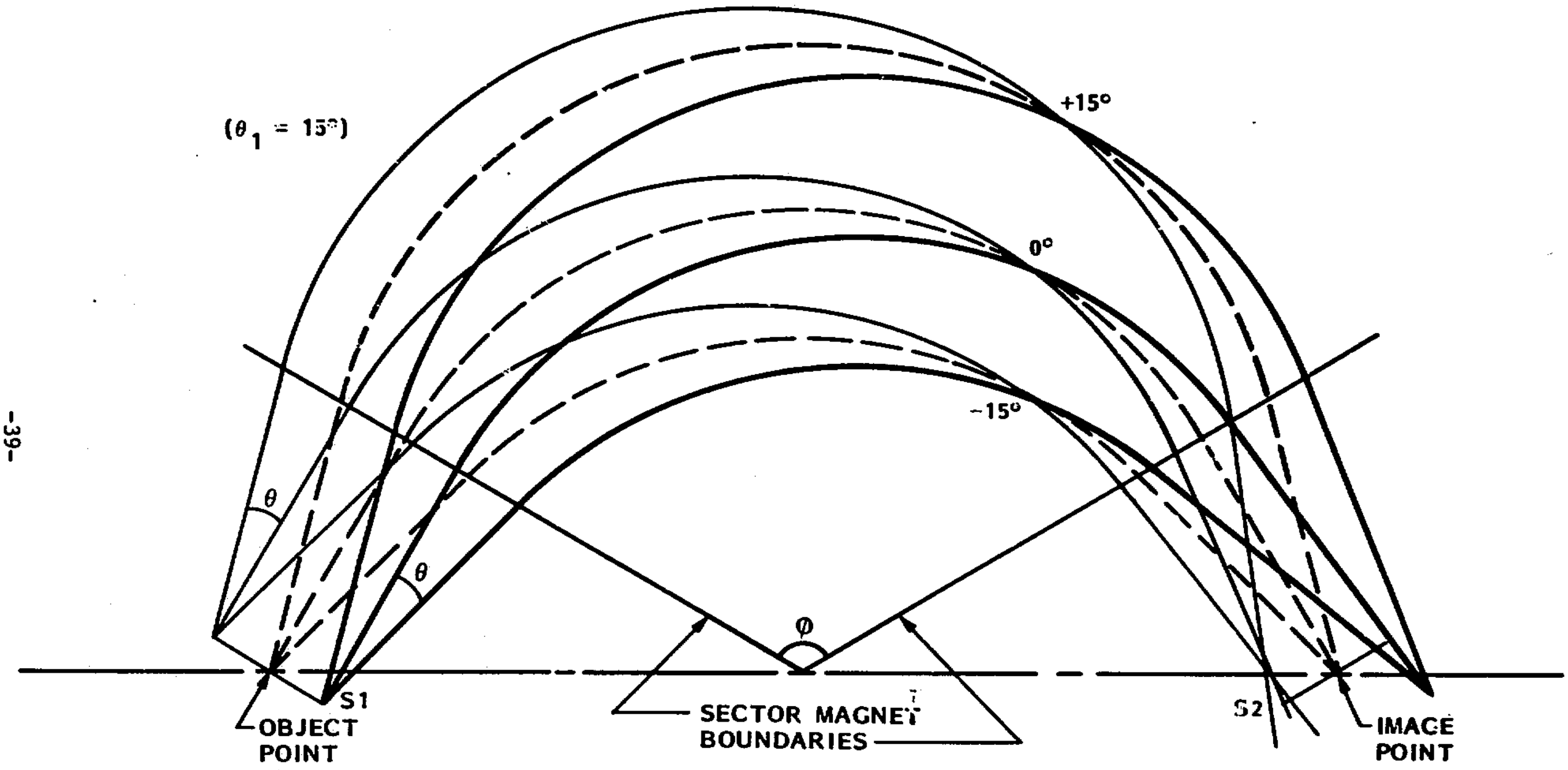

Figure 22. Bend focal properties of the HERS magnetic sector analyzer. Slit widths are exaggerated to emphasize the effects of finite slit width and non-paraxial rays.

focus ions of a fixed energy E_o emanating from an object point S1 onto an image point S2 where S1, S2 and the apex of the sector magnet lie on a straight line. In this case

$$E_o = P_o^2/2m \tag{13}$$

$$P_o = qr_oB \tag{14}$$

where P_o is the momentum, m is the mass, q is the charge, B is the magnetic field and r_o is the radius of curvature, which for normal entry to the magnet is the distance from the apex to the point of entry.

For non-paraxial rays a sector magnet still has the same focal properties, but with the condition that

$$E\cos^2\theta = P_o^2/2m = E_o \qquad (15)$$

where θ is the angle of incidence relative to the sector magnet boundary normal. This is demonstrated by the set of three dashed ion trajectories emanating from the center (object point) of S1 and converging on the center of S2 (image point).

The two sets of solid line ion trajectories in Figure 22 which emanate from the ends of S1 demonstrate the fact that the focal properties hold strictly only for an infinitesimal object size. To first order, however, these ions do come to a focus along the line joining the image and object points. In Figure 22 the sizes of S1 and S2 have been exaggerated to emphasize the effect. If one were interested only in the focal properties of the magnetic analyzer one would select an image slit along the first order focal line. However, in the HERS the image slit for the magnetic analyzer (S2) acts as the object for the electrostatic deflector, and it is essential that this object slit be normal to the central ion trajectory. As will be discussed in the next section, the imaging properties of the electrostatic deflector require that the ions entering the deflector satisfy equation 15.

Figure 23 shows the theoretical energy passbands of the HERS magnet system for slit widths of 0.9 mm. In this figure both the horizontal scale and the vertical scale are proportional to $\cos^{-2}\theta$. The actual angles are also shown as a non-linear horizontal scale. From equation 15 we see that,

$$E = E_o \cos^{-2}\theta \qquad (16)$$

This equation defines the two diagonal lines with slopes of -1 and 1, respectively, which diverge from $\theta = 0$, $E = E_o$. From equations 13 and 14 we see that

$$\frac{\Delta E}{E_o} = \frac{2\Delta P}{P_o} = \frac{2\Delta r}{r_o} \qquad (17)$$

and from the geometry of Figure 22 we see that Δr is proportional to the widths of S1 and S2. Since to first order r is proportional to $\cos^{-1}\theta$, the fixed slit widths would infer a symmetric narrowing of $\Delta E/E$ with increasing θ either positive or negative. However, to second order, we note in Figure 22 that for negative θ the image of S1 is compressed relative to the image for $\theta = 0$ while for postive θ the image is expanded. This permits a wider range

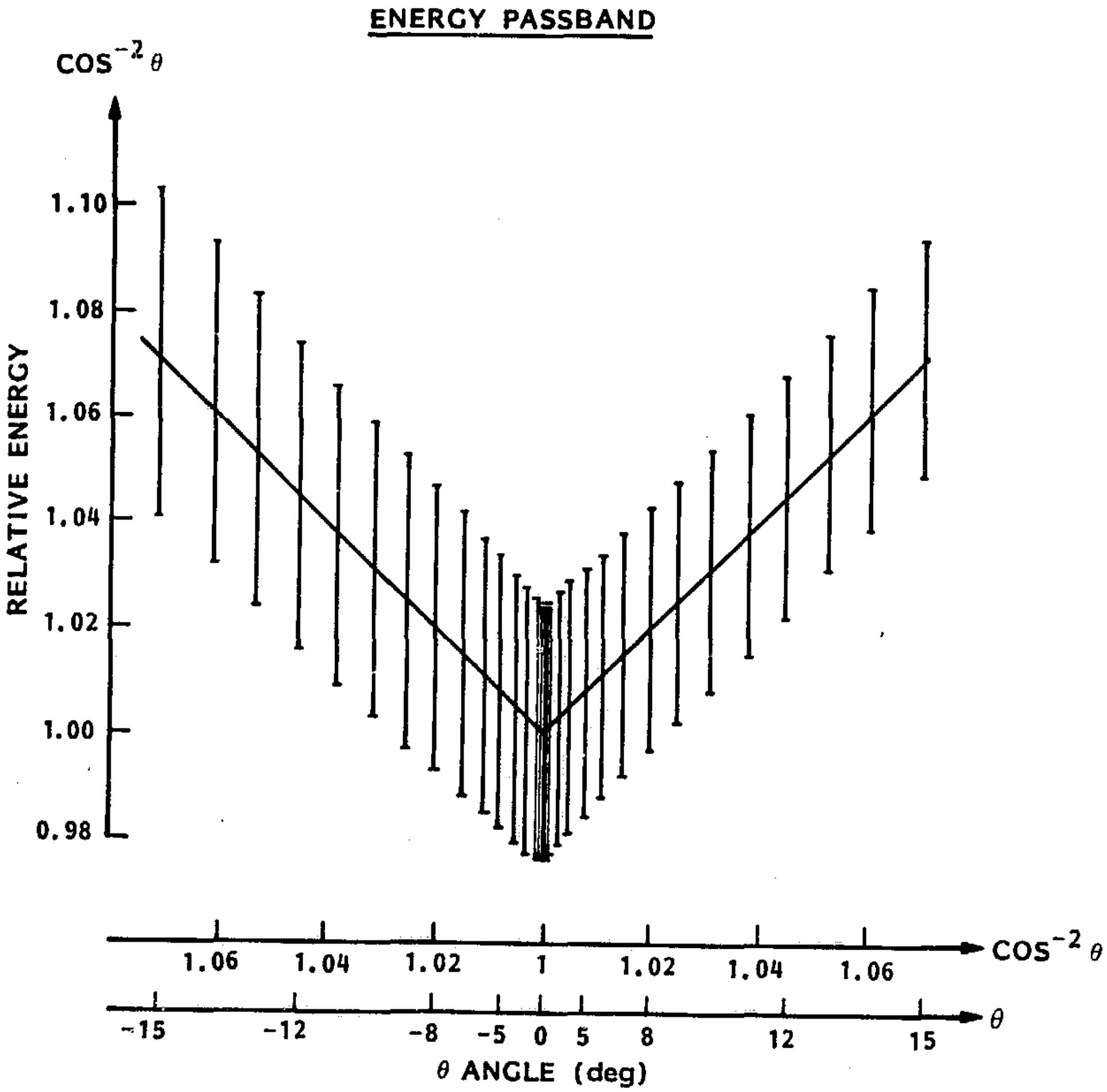

Figure 23. Energy passband of HERS magnetic analyzer as a function of incident angle Θ. Both the Θ axis and the relative energy axis are parameterized as $\cos^{-2}$ to show the linear relationship per Equation 16.

of momenta to be accepted within a given S2 slit width for negative angles and a narrower range for positive angles. This is the explanation for the assymetry in the energy passbands of Figure 22.

All of the preceeding analysis was based on an idealized "hard edged" magnetic field. That is the field is assumed to abruptly jump from zero outside the magnet boundaries in Figure 22 to a constant and uniform field inside the boundaries. For paraxial rays entering normally to the magnet boundary, the fringing field simply moves the effective boundary of the magnet outward. However, for non-normal ion entry the component of the fringing field transverse to the ion velocity will apply either an upward or a downward force to the ions. This is illustrated in Figures 24 and 25. Figure 24 illustrates schematially in three dimensions the relationships among the fringing field, the magnet boundary and the ion velocity for ions approaching the magnet with a positive θ (see figure 22) but with a velocity vector parallel to the plane of the magnet. That is $\vec{v}$ is perpendicular to $\vec{B}$(INTERNAL). Three cases are shown; one where the ion is moving in the central plane ($\vec{v}_c$), one where the ion is below the central plane ($\vec{v}_L$), and one where the ion is above the central plane ($\vec{v}_u$). $\hat{N}$ represents the inward normal to the magnet boundary. For positions well away from a corner of the magnet the fringing field lies in plane defined by $\hat{N}$ and $\vec{B}$(INTERNAL).

Figure 25 is a more detailed illustration of the geometry in the fringing field region. The coordinate system is defined with $\hat{x}$ parallel to $\vec{v}$ and $\hat{z}$ parallel to $\vec{B}$(INTERNAL). We assume that $\vec{v}_u$ and $\vec{v}_L$ are symmetric about the central plane. From symmetry $\vec{B}_c$ is parallel to the $\hat{z}$ axis.

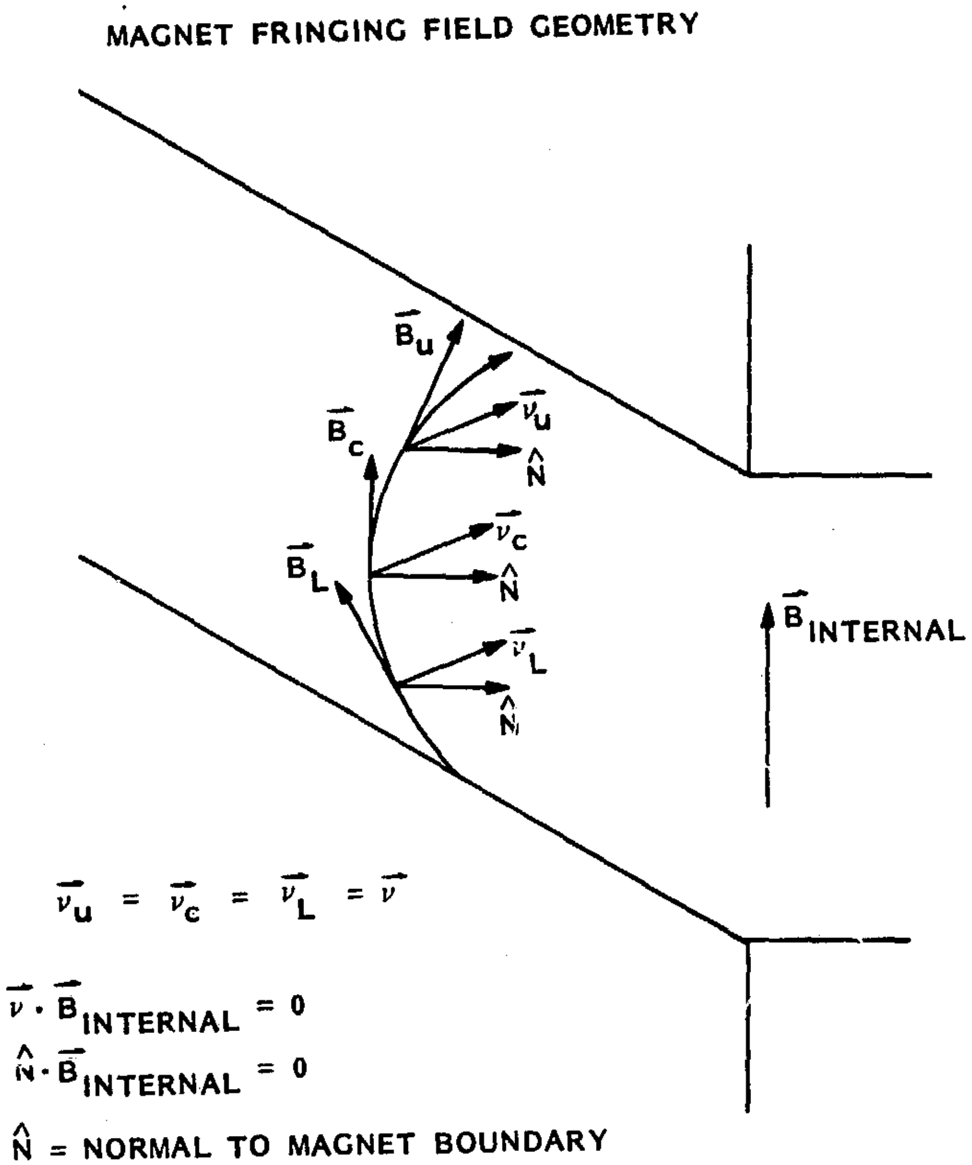

Figure 24. Geometry for analysis of focal properties of the fringing field of a sector magnet. The ion velocities are in the plane of the magnet, perpendicular to the internal field. v_c lies in the median plane and v_u and v_L symmetrically above and below the median plane, respectively. See Figure 25 for more detail.

GEOMETRY FOR Z-FOCUSING IN FRINGING MAGNETIC FIELD

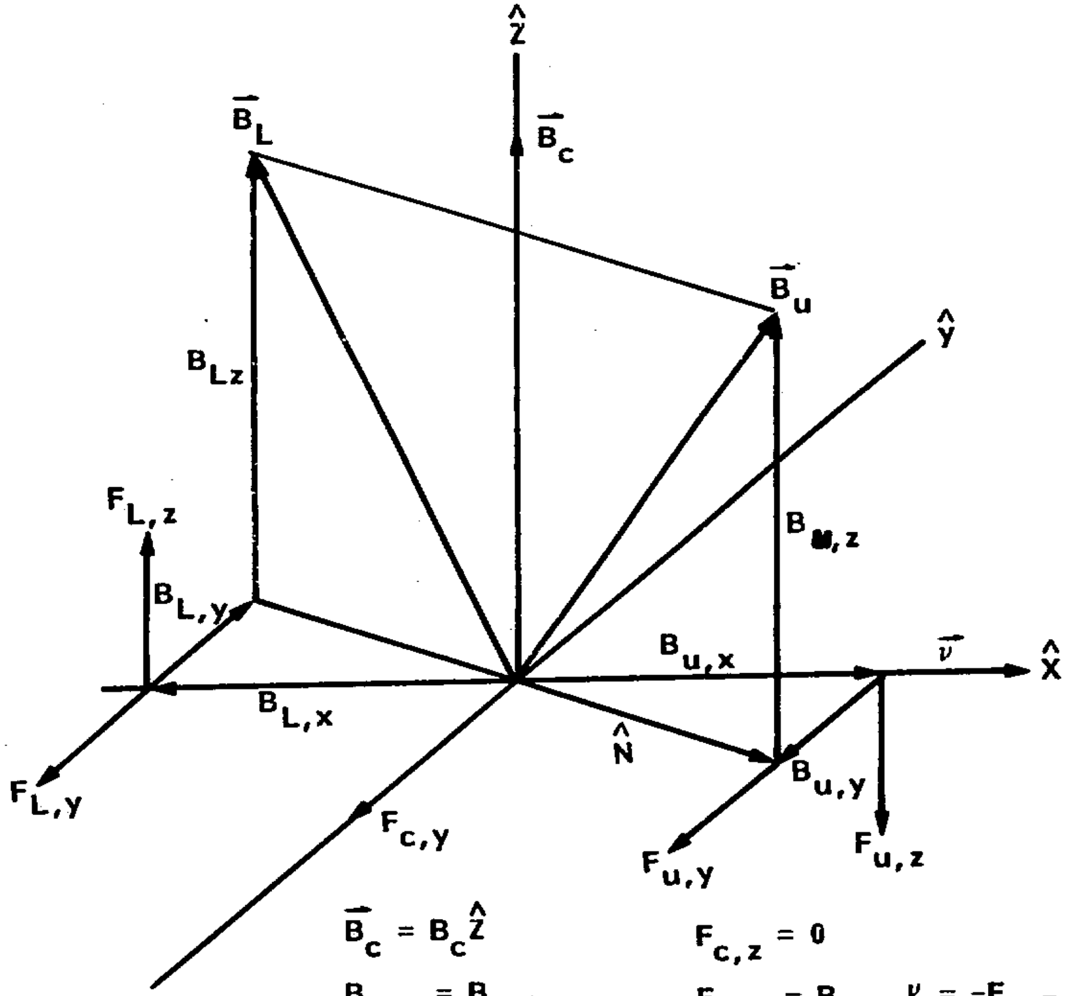

$\vec{B}_c = B_c\hat{Z}$

$B_{L,Z} = B_{u,Z}$

$B_{L,y} = -B_{u,y}$

$B_{L,x} = -B_{u,x}$

$F_{c,z} = 0$

$F_{L,Z} = B_{L,Z}\,\nu = -F_{u,Z}$

$F_{L,y} = B_{L,Z}\,\nu = F_{u,y}$

$F_{c,y} = B_c\,\nu$

$F_{L,x} = F_{u,x} = F_{c,x} = 0$

Figure 25. Detailed geometry for fringing field vertical focusing. In this coordinate system x is parallel to v and z is parallel to the internal field. See text for details.

Since the force on an ion is given by

$$\vec{F} = q\vec{v} \times \vec{B} \tag{18}$$

the only force acting on the central plane ion is in the $-\hat{y}$ direction. Since the $\hat{z}$ component of the fringing field is everywhere positive, the $\hat{y}$ component on all ions is negative. From equation (18) we see that there can be no $\hat{x}$ component of force since $\vec{v}$ is parallel to $\hat{x}$. The component of force which is of particular interest to us here is that along the $\hat{z}$ direction. From (18) we see that

$$F_z = v_x B_y = vB_y \tag{19}$$

Thus, since v_x is positive by definition, F_z has the sign of B_y. This means that ions above the central plane experience a downward force and ions below the central plane experience an upward force. This results in a focusing of ions for the geometry shown in Figures 24 and 25. As we pointed out above, that geometry is for positive θ angles. It is easy to see that for negative θ angles the $\hat{z}$ forces are reversed. That is these ions experience a defocusing force. The effect of this focusing is to increase the transmission of ions with positive θ angles and reduce the transmission of ions with negative θ angles.

Figure 26 shows the predicted angular resolution of the magnet at $\theta = 0^{\circ}$. Similar responses are predicted for other angles. If we now combine the above described focusing effects with the energy passband predictions of Figure 23 and the angular resolution (e.g. Figure 26) we can predict the θ dependence of

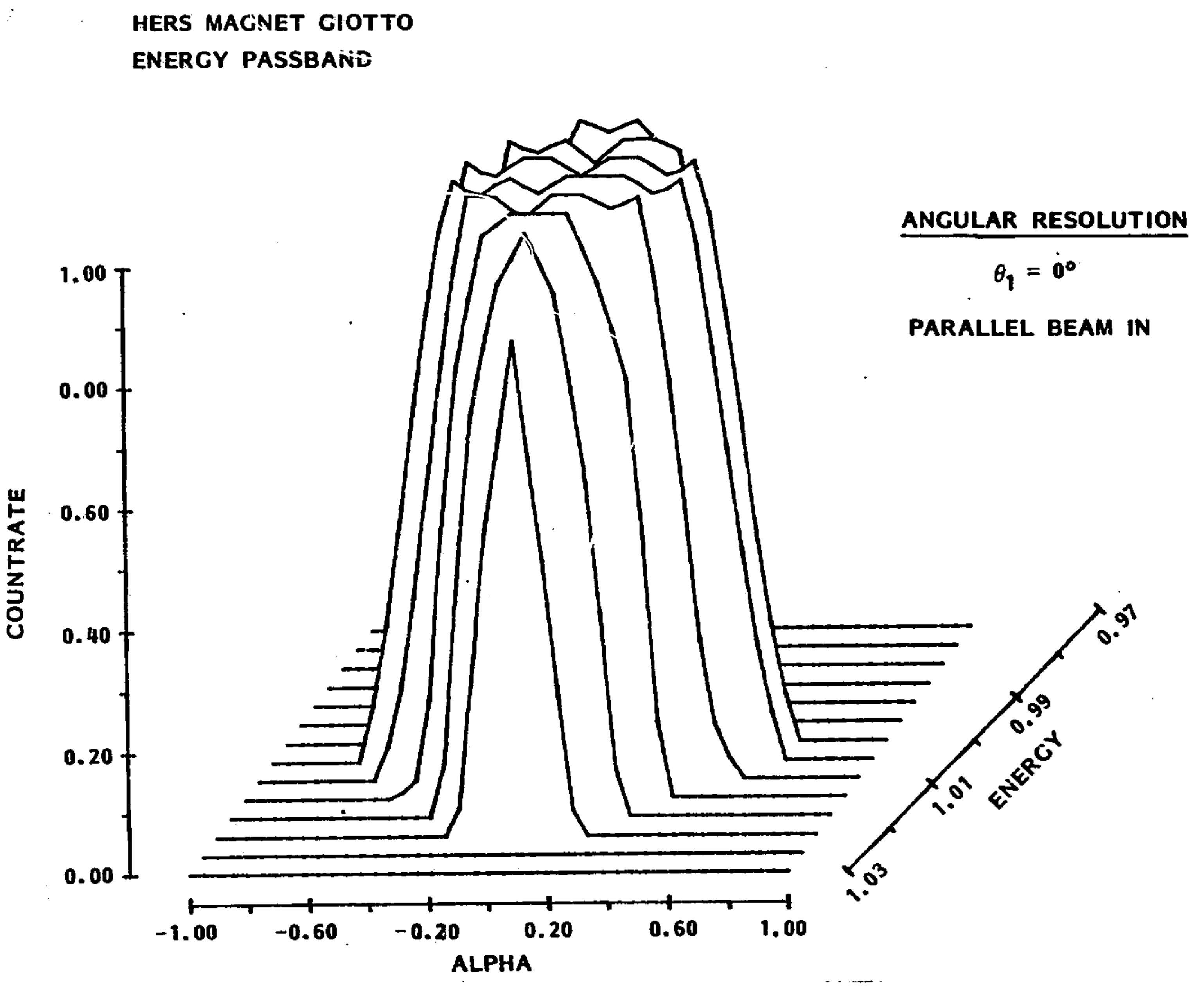

Figure 26. Angular resolution of the HERS magnetic analyzer. Predicted exit angles (labeled ALPHA) a function of energy for a parallel input ion beam.

the total magnet transmission. The results of computer modeled magnet transmission characterstics are shown in Figure 27. The transmission increases monotonically from negative θ through zero to positive θ. Less obvious is the increased angular width at a fixed energy for ions with negative θ. This is related to the energy passband shown in Figure 23.

Figure 28 shows the laboratory verification of the predicted θ dependent transmission. In this case we have used a relative energy scale which is parameterized in θ ($E \propto \cos^{-2}\theta$) for direct comparison with Figure 23. The results are both qualitatively and quantitatively consistent with prediction. For example, note the relative widths of the $+15^{\circ}$ and -15° curves.

The homogeniety of the magnetic field within the magnet is an important parameter in the ultimate mass resolution of the system. The theoretical focal properties assume that the field is constant everywhere in order to satisfy equation (15). The specification for homogeniety was ± 0.1%. Figure 29, which shows contours of constant field strength actually measured in the magnet shows that only the 0.1% contour deviates measureably from the magnet boundary shape. All other contours are confined to the fringing field.

2.5 Electrostatic Deflector (ESD)

The magnetic analyzer separates ions according to their normal component of momentum per unit charge, resulting in the fact that all ions entering the electrostatic deflector (exiting the magnetic analyzer) have energies proportional to $\cos^{-2}\theta$ (see Equation 15). In order to separate these ions according to mass per unit charge, the electrostatic deflector (ESD) must

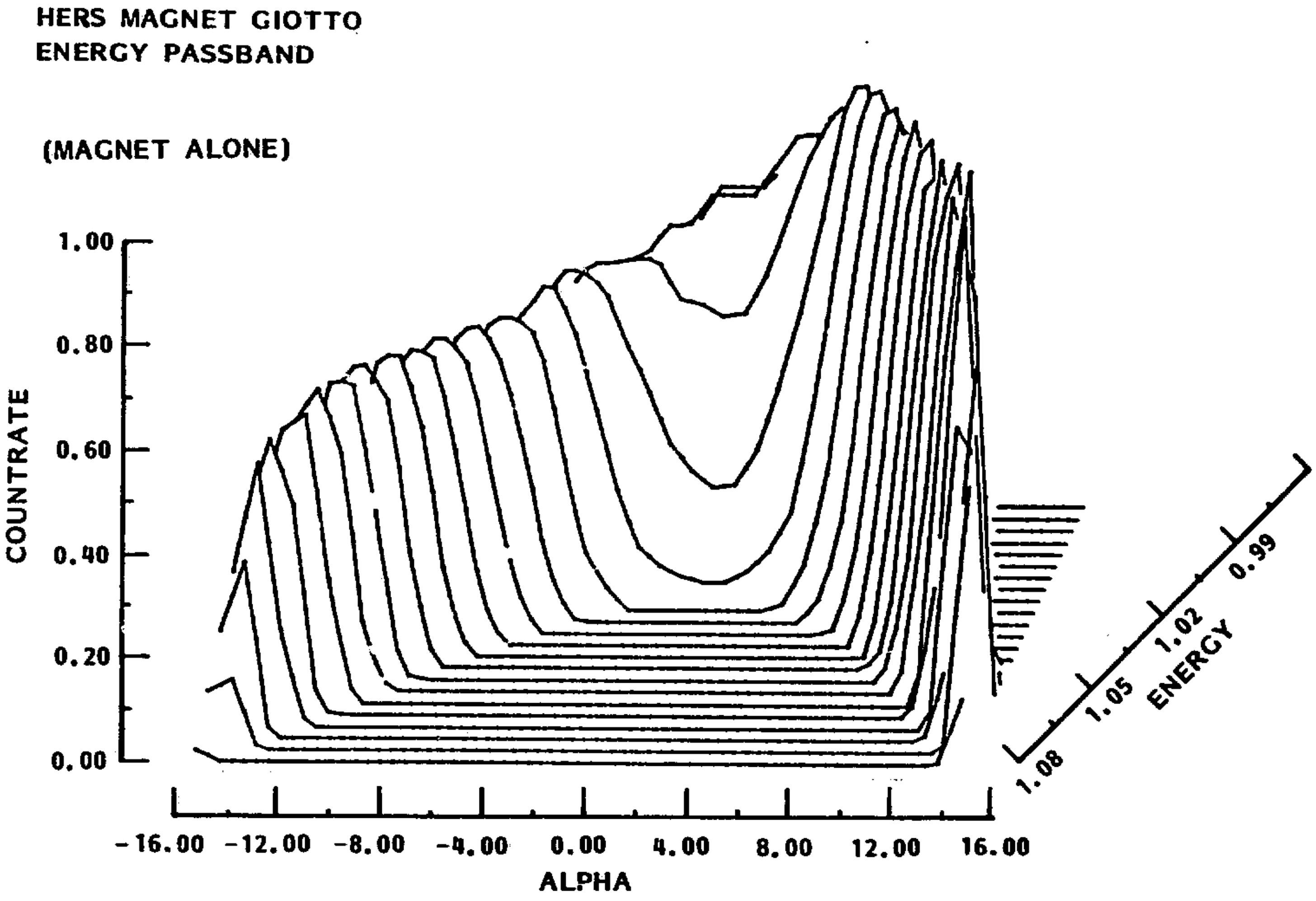

Figure 27. Theoretical energy passband as a function of incident angle for the HERS magnetic analyzer. Both bend plane and vertical plane focusing are included. Note narrower but higher responses for positive Θ (labeled ALPHA here) angles.

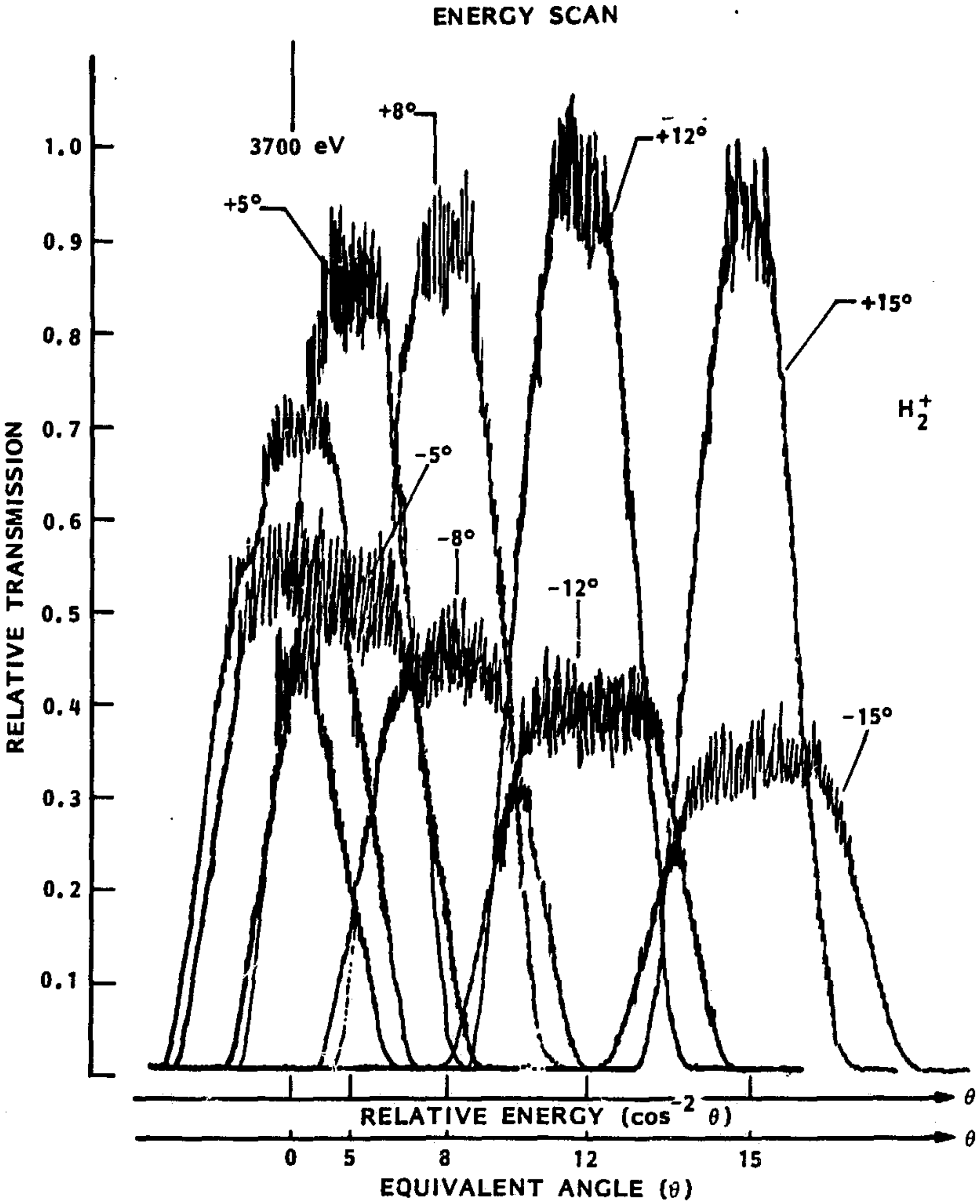

Figure 28. Measured energy passband of the HERS magnetic analyzer as a function of incident angle Θ. The relative energy axis is parameterized as $\cos^{-2}\Theta$. See Equation 16. In comparing with Figure 27 note that both positive and negative angles increase to the right.

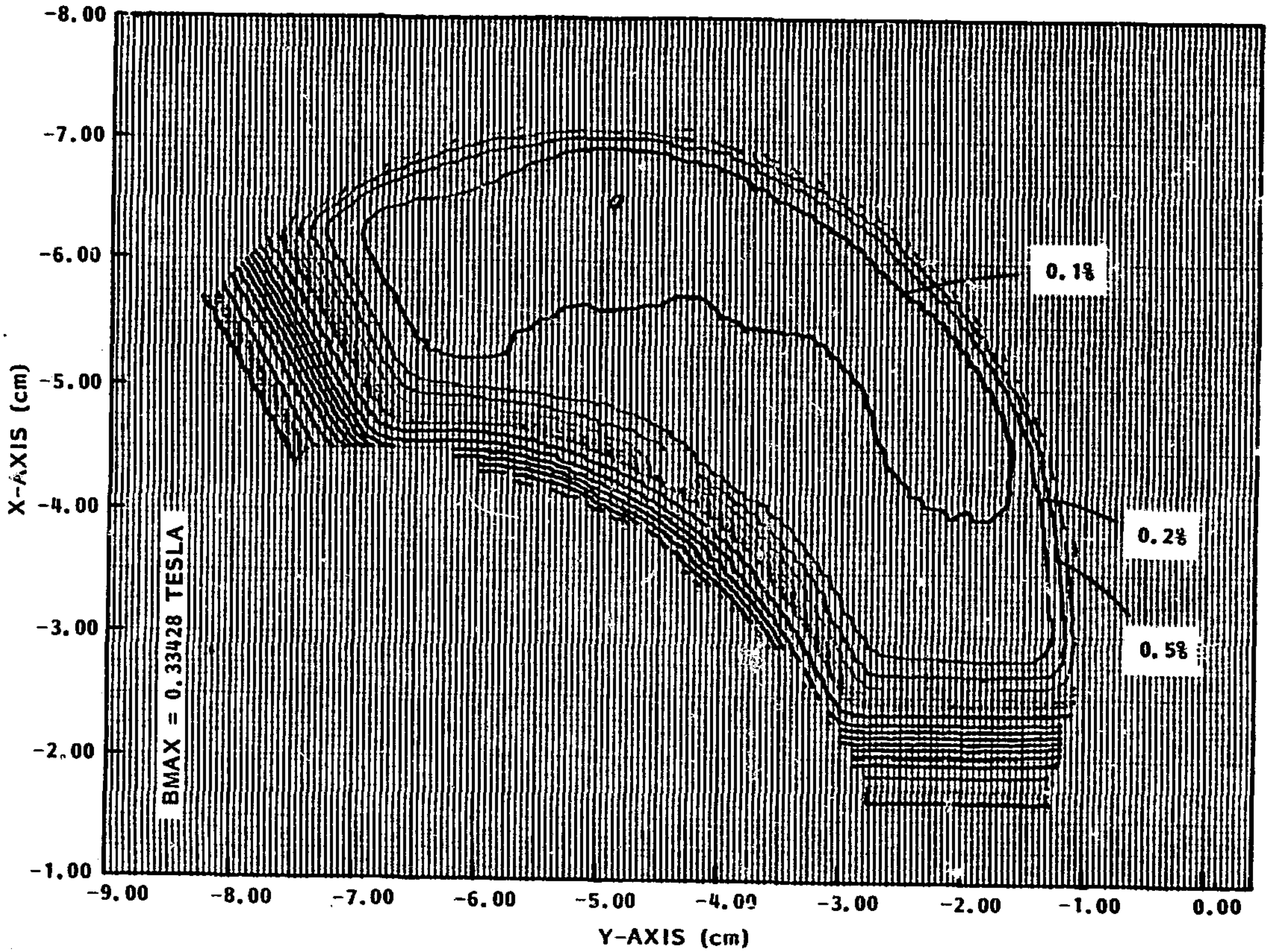

Figure 29. Constant field contours measured for the HERS magnet. Note that only the 0.1% contour deviates significantly from the magnet boundary. All other contours are dominated by edge effects.

disperse them according to their normal component of energy per unit charge. This can be seen by solving Equation 15 for m and substituting from Equation 14,

$$m/q = \frac{r_o^2 B^2}{2(E/q)\cos^2\theta} \tag{20}$$

A two dimensional field lying in the plane $\theta = 0^o$ has this property. That is, the component of particle motion in the plane of the field depends only on the strength of the field and the parameter $E_o/q = (E/q)\cos^2\theta$. The motion perpendicular to this plane is unaffected. While any two dimensional field acting with a component normal to the ion trajectory would result in m/q dispersion, good mass resolution requires not only m/q dispersion but focusing of ions with a fixed m/q. This could be achieved with a uniform parallel field for a single ion species; however we require simultaneous focusing of ions over a wide range of masses. An optimum field configuration was achieved by iteratively altering the potential distribution on the boundary of the ESD and determining the focal properties by computer ray tracing. (This work as well as most of the other ray tracing work was performed by JPL).

Figure 30 illustrates an example of an optimized potential distribution achieved by forcing constant potential gradients along various segments of the boundary. Such boundary conditions are very useful for computer simulations; however, they are far from optimum for implementation in space instrumentation. For one reason it is very difficult to achieve highly uniform resistivity over large surfaces. Semiconducting glass plates are relatively heavy and have very strong thermal coefficients of resistivity. They also

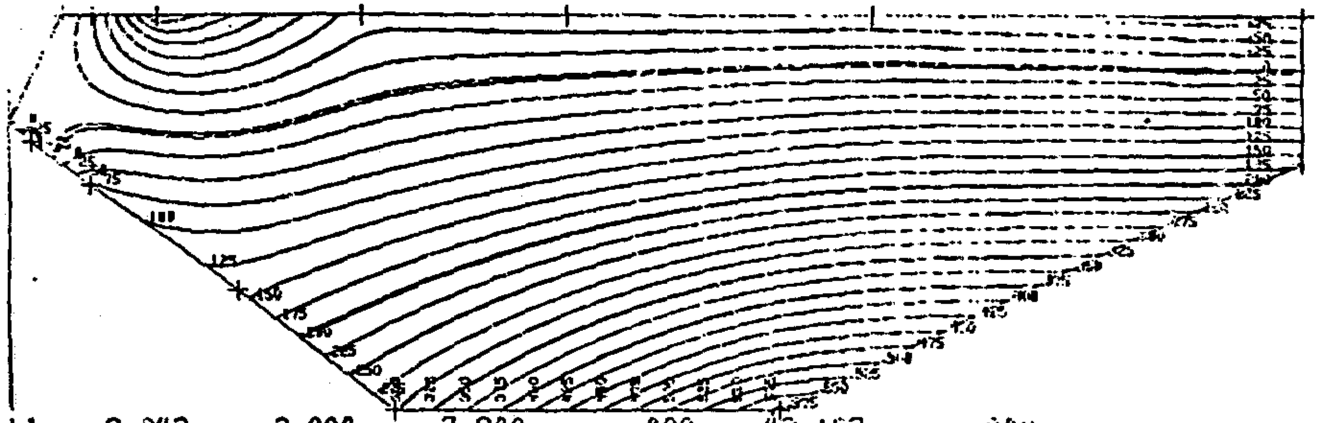

```
1     9.243      2.000     7.800      .000   -43.167      .000
1    12.669      6.750     9.243     2.000    78.867   -43.167
1    20.857     18.100    12.669     6.750   138.833    78.867
1    29.800     30.500    20.857    18.100   297.033   138.833
3    29.800     60.000    29.800    30.500   578.900   297.033
2    11.000    100.000    29.800    60.000   166.133   578.900
2      .000    100.000    11.000   100.000   -93.333   166.133
3      .000     67.000      .000   100.000   -70.700   -93.333
3      .000     43.500      .000    67.000   -70.700   -70.700
3      .000     27.750      .000    43.500   -59.267   -70.700
2      .000     12.000      .000    27.750  -199.967   -59.267
3      .000      7.000      .000    12.000   -42.933  -199.967
3      .000      4.503      .000     7.000      .000   -42.933
4      .000      4.503     7.800      .000      .000      .000
   30.0000     .0000    -.0185     .0338    -.0184    -.0857     .0595   -.0254
     .1373     .2481     .0712    -.0303    -.0400     .0000    3.3000  15.0000
    .00000    .00000    .00000    .00000    .00000    .00000
```

Figure 30. Equipotential contours for optimum two dimensional electrostatic deflector focal properties using continuous potential boundary conditions. Ions enter normal to the short diagonal segment in the upper left and focus onto the upper plane.

tend to have high secondary electron emission coefficients which can result in field distortions when surfaces ar bombarded by high fluxes of ions. Lower impedence systems which are less vulnerable to effects of secondary emission consume excessive power at the high voltages required in the HERS system (≈ 5,000 Volts). Continuous surfaces also present significant ion scattering problems which results in background.

For all of the above reasons, it is far more practical to define the potential boundary conditions at discrete values. To first order this is achieved by placing electrodes at the boundaries tangent to the desired equal potential contours. This is illustrated in Figure 31 where the straight solid lines represent electrodes at fixed voltages and the contour lines represent the resultant equipotentials. This process was iterated until the resultant potential contours were equivalent to the optimum contours of Figure 30 within the regions of interest (i.e. the region traversed by the ions being focused onto the detector plane).

Figures 32-34 show a representative set of resultant ion trajectories for the final version of the HERS ESD. For clarity only the electrodes and the ion trajectories are shown. Figure 32 represents the conditions for the light ion mode (L-mode). As we will discuss in more detail below, the two dimensional microchannel plate (MCP) detector is located two millimeters above the upper horizontal surface of the ESD between the two vertical line segments near the ray bundles labeled 2 and 4. The trajectories take into account the potential on the face of the MCP which accelerates the ions after they exit the ESD. Note that while the ions with mass per charge between 4 and 2 ($^4He^+$ and $^4He^{2+}$ respectively) are intercepted by the MCP, ions with mass per charge

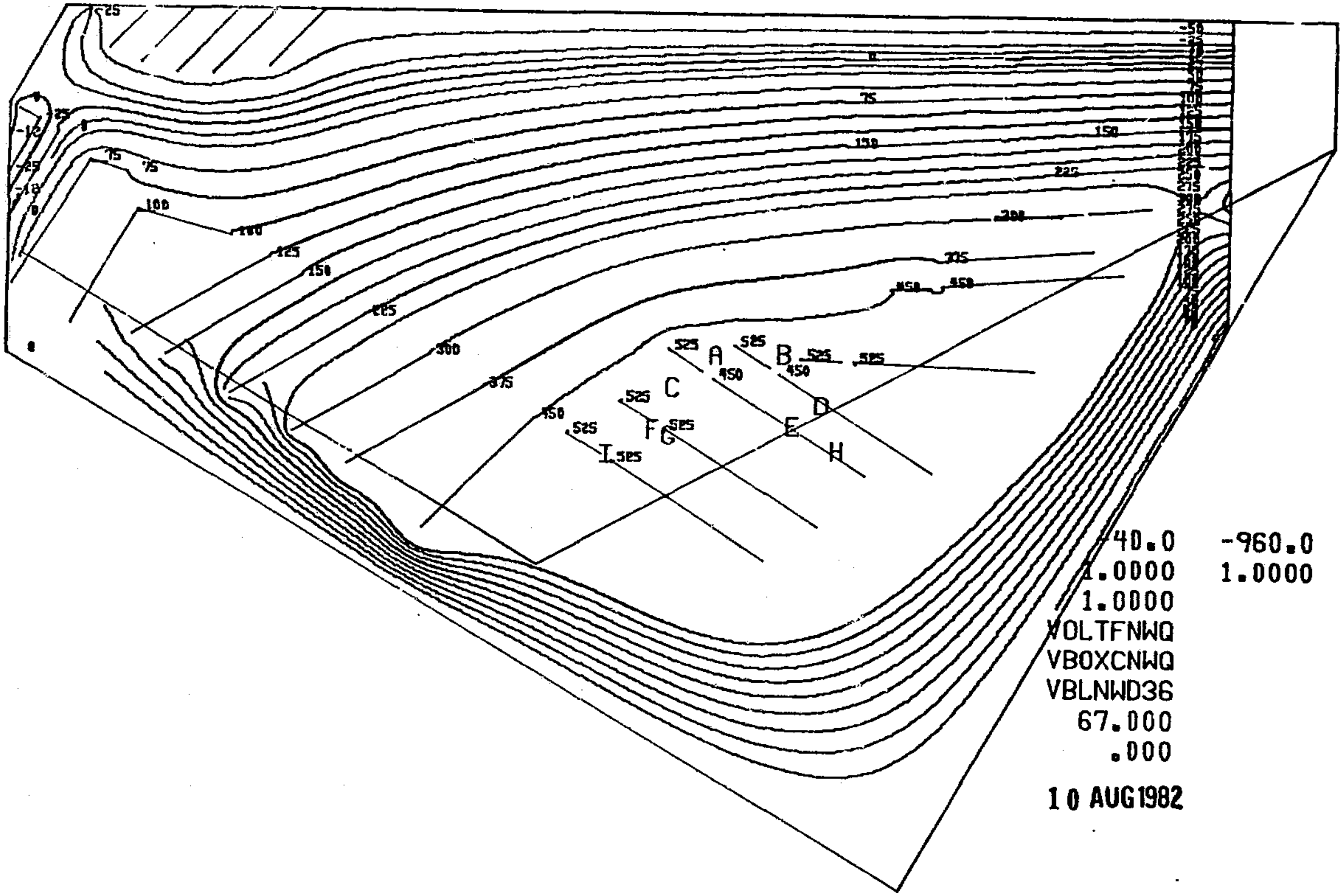

Figure 31. Equipotential contours for best approximation to optimum field of Figure 30 using discrete electrode boundary conditions in two dimensions.

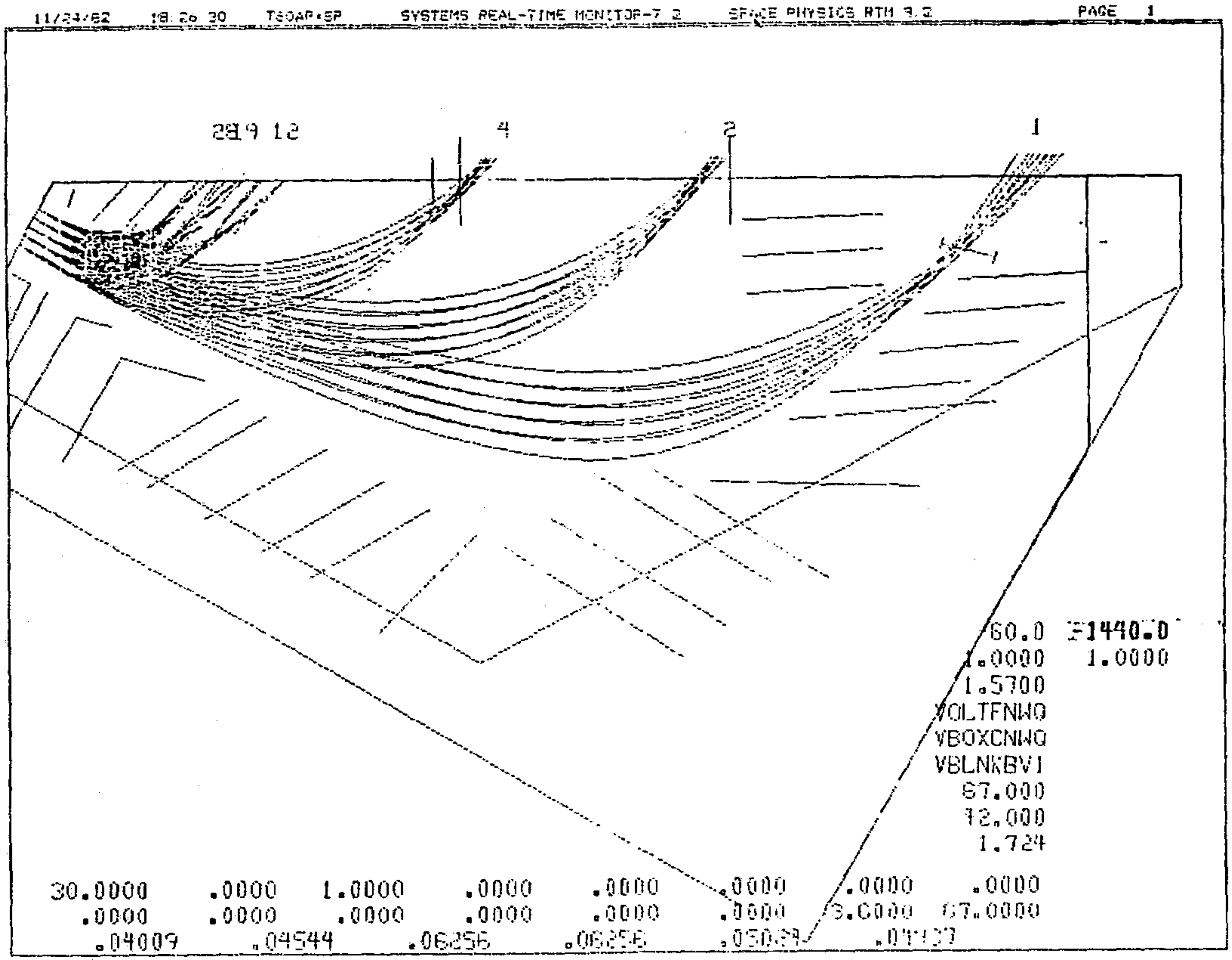

```
11/24/82   18:26 30   TSOAP+SP   SYSTEMS REAL-TIME MONITOR-7 2   SPACE PHYSICS RTM 9.2   PAGE  1
```

```
                                                                      60.0   F1440.0
                                                                     1.0000   1.0000
                                                                     1.5700
                                                                   VOLTFNWO
                                                                   VBOXCNWO
                                                                   VBLNKBV1
                                                                     67.000
                                                                     12.000
                                                                      1.724
30.0000    .0000   1.0000     .0000     .0000     .0000     .0000     .0000
  .0000    .0000    .0000     .0000     .0000     .0000    3.0000   67.0000
   .04009    .04544     .06256     .06256     [illegible]     [illegible]
```

Figure 32. Ion trajectories calculated for electrostatic deflector field of Figure 31 with absolute potentials adjusted for the light ion mode (L-mode). Only discrete electrodes and ion trajectories are shown. The short line segment crossing the ray bundle labeled 1 in the upper right represents the CEM detectors. The MCP detector is represented by the two long vertical line segments near the ray bundles labeled 2 and 4.

1 ($^1H^+$) pass through an opening in one of the equipotential electrodes. The H^+ ions area intercepted by channel electron multipliers (CEMs).

The bulge in the equipotential surfaces near the upper left corner of the ESD (see Figures 30 and 31) is generated by a series of nearly vertical electrodes all at the same potential. This serves to trap heavier ions which impact this area of the ESD in the L-mode. This minimizes the probability that these ions will scatter onto the MCP. All electrodes are oriented so that ions impact them on the underside so that secondary ions will not have access to the MCP. Any electrons produced by ion bombardment of the electrodes drift away from the MCP.

Figures 33 and 34 show the ion trajectories for the medium mode (M-mode) and heavy mode (H-mode) respectively. The diverging bundle of trajctories running diagonally from the upper left corner of Figure 33 is an artifact of the computer code. Mass resolution of approximately 1 AMU is achieved in the L- and M-modes, with proportionally reduced resolution in the H-mode.

We note from equation 15 that the ion energy, and thus the relative potentials required to deflect the ions onto the MCP, is inversely proportional to the mass per charge of the ions being analyzed. Thus in the H-mode the maximum ESD potential is only a few hundred volts. In this case the MCP potential, which is applied just outside the ESD, is much larger and care must be exercised to insure that this potential does not significantly alter the optical properties of the ESD. To minimize this effect, the MCP is isolated from the ESD by two high transmission grids spaced approximately one millimeter apart. Typical MCP voltages, which must be altered to compensate

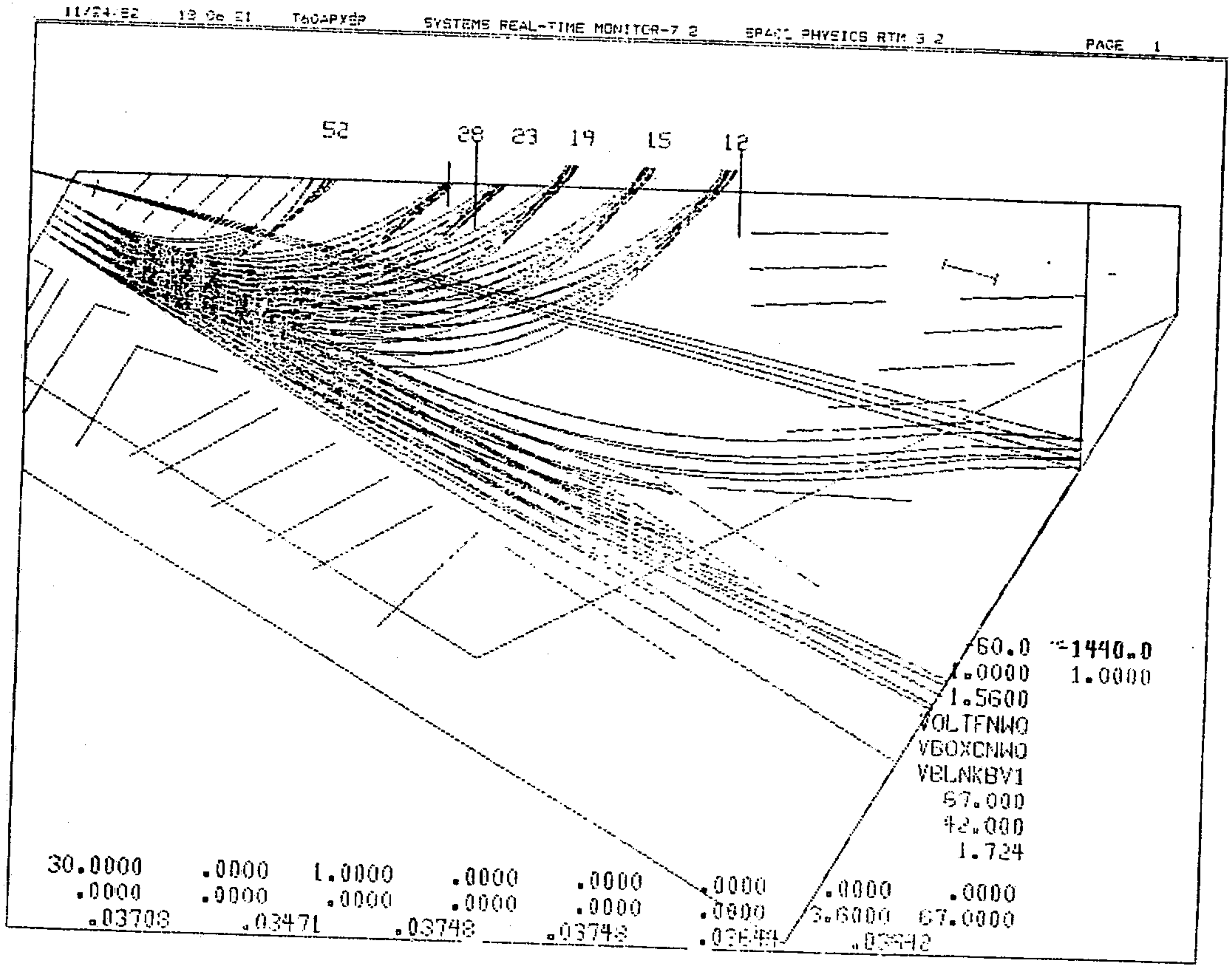

Figure 33. Ion trajectories for the medium ion mode (M-mode). Numbers along the top indicate the mass per charge (amu/e) for the respective ray bundles. The bundle of rays diverging linearly from the upper left and intersecting the right hand edge is non-physical and results from an error in the ray tracing code. See Figure 32 caption for more detail.

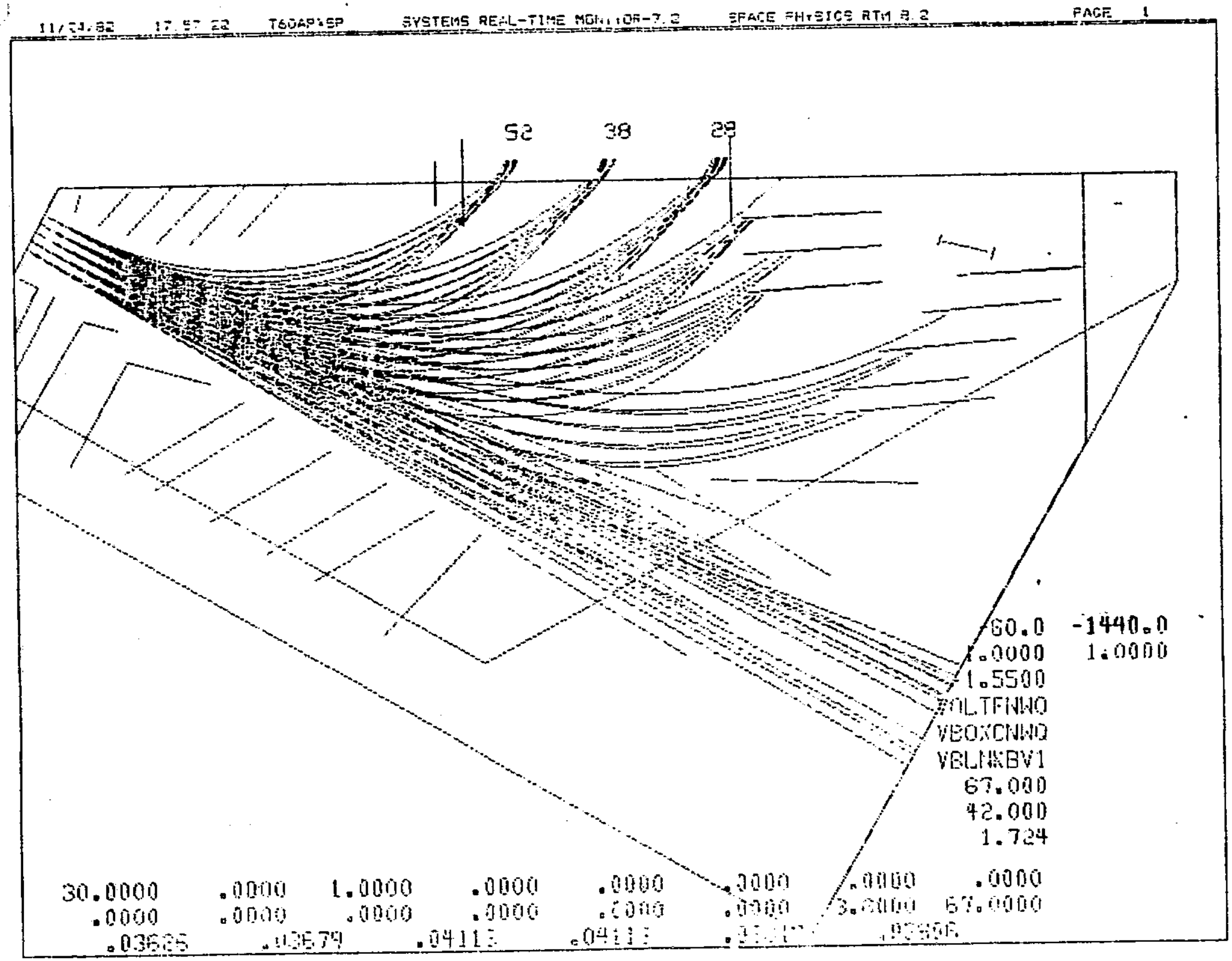

Figure 34. Ion trajectories for the heavy ion mode (H-mode). As with Figures 32 and 33 an MCP potential of -1440 Volts is assumed.

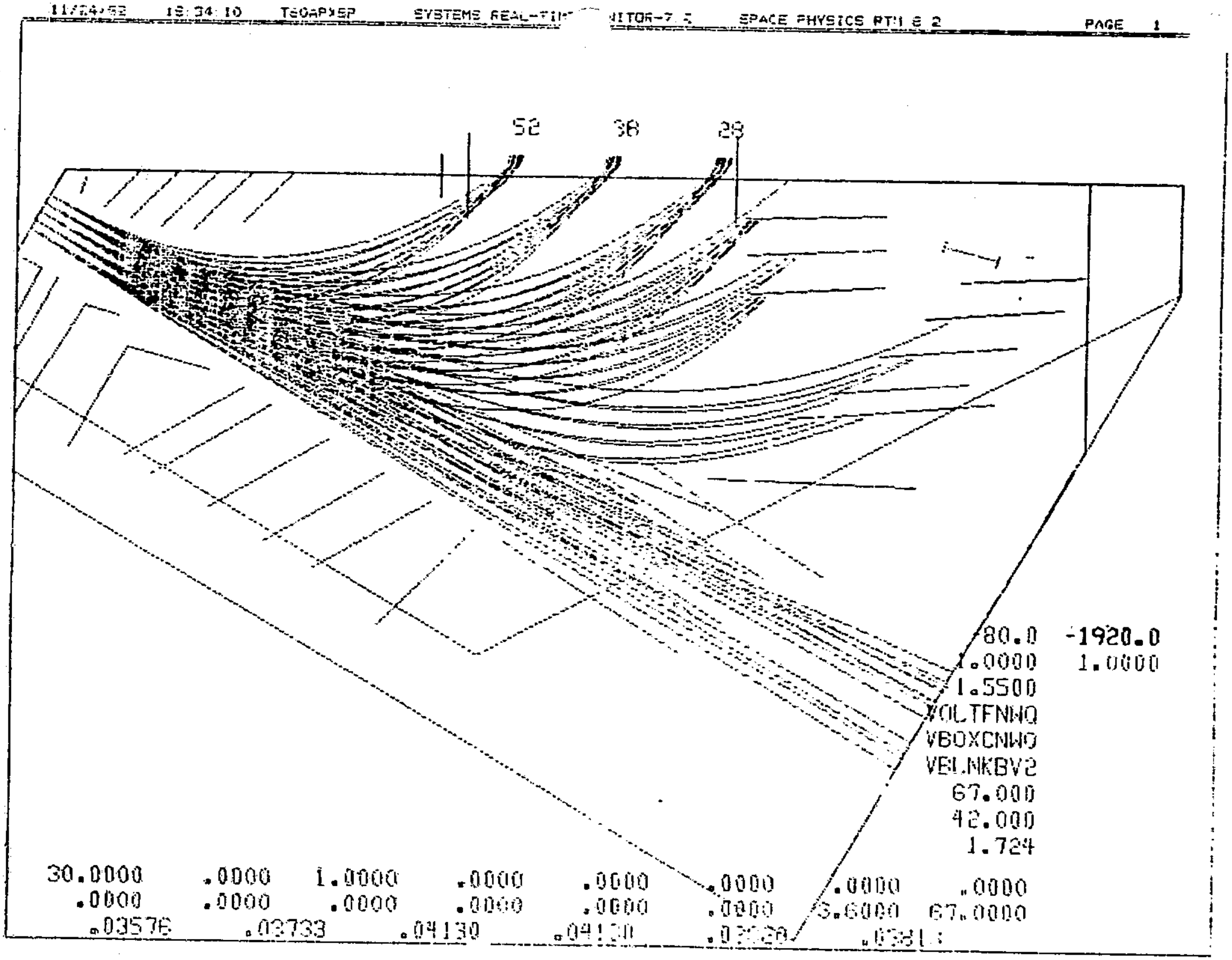

Figure 35. Same as Figure 34 except for an assumed MCP potential of -1920 Volts. Note the more vertical trajectories outside the electrostatic deflector boundary near the MCP which results from the increased ion acceleration in this region.

ORIGINAL PAGE IS
OF POOR QUALITY

for gain variations, range from approximately -1500 Volts to -1850 Volts. Figures 34 and 35 compare ion trajectories for -1440 Volts and -1920 Volts, respectively. One can see that the m/q = 52 trajectories in Figure 35 are more nearly vertical when they strike the MCP (the end of the trajectories) than are those in Figure 34. It is found that for the L-mode and M-mode the effects are undetectable and for the H-mode the mass peak shift is a small fraction of the mass line width.

All of the above data are based on computer simulations of the ESD. The actual implementation of the ESD model within the constraints of space instrumenation proved to be a significant technological challenge. The computer simulations assumed a two dimensional geometry. That is the boundary conditions were only specified in two dimensions, the system was assumed to be infinite in the third dimension. This would generally require that the system be long in the third dimension in comparison to the "working region" and all other dimensions such as the spacing between electrodes. The alternative is to impose the desired boundary conditions in the third dimension. This was the approach taken. The imposition of these boundary conditions was accomplished by gold plating equipotential contours per Figure 31 onto the ceramic substraits which serve as end plates on the ESD. Since these contours match the free space equipotentials per Maxwell's equations, they do not distort the field at distances large compared with their thickness and spacing. These contours can be seen in Figure 36, which is a photograph of the Prototype HERS ESD without its upper electrode in place.

In order to maintain adequate dimensional stability and thermal compatability, the entire ESD structure was constructed of ceramic and titanium. The discrete electrodes or "vanes" referred to in conjunction with Figures 31 through 35 are clearly visible in Figure 36 as the gold colored plates suspended between the two ceramic end plates. These vanes were produced by gold plating rigid, flat, ceramic sheets with machined sharp leading edges to minimize scattering and to precisely define the equipotential surfaces. In the flight version of the ESD these vanes are copper-blacked to further reduce scattering. The gridded slot which transmits ions of mass per charge equal to 1 in the L-mode (see Figure 32) is visible near the top of the ESD in Figure 36.

The electrode structure consisting of epoxy bonded ceramic elements is suspended from a titanium support structure by three titanium rods. Two of these rods are visible, one in the foreground and one near the top. The third is located in the lower righthand corner. This construction provides a maximum of dimensional stability with a minimum of thermal stress. The high voltage contact to the electrode structure can be seen projecting through the right hand titanium support structure.

Figure 37 shows a more complete assembly of the ESD including the S2 slit sub-assembly and the upper electrode structure with the double grid and the cut-out for the MCP detector.

2.6 Detector System

The detector system which interfaces with the ESD consists of two sub-assemblies. These include a two-dimensional imaging microchannel plate (MCP) assembly and a set of four channel electron multiplier (CEM) detectors.

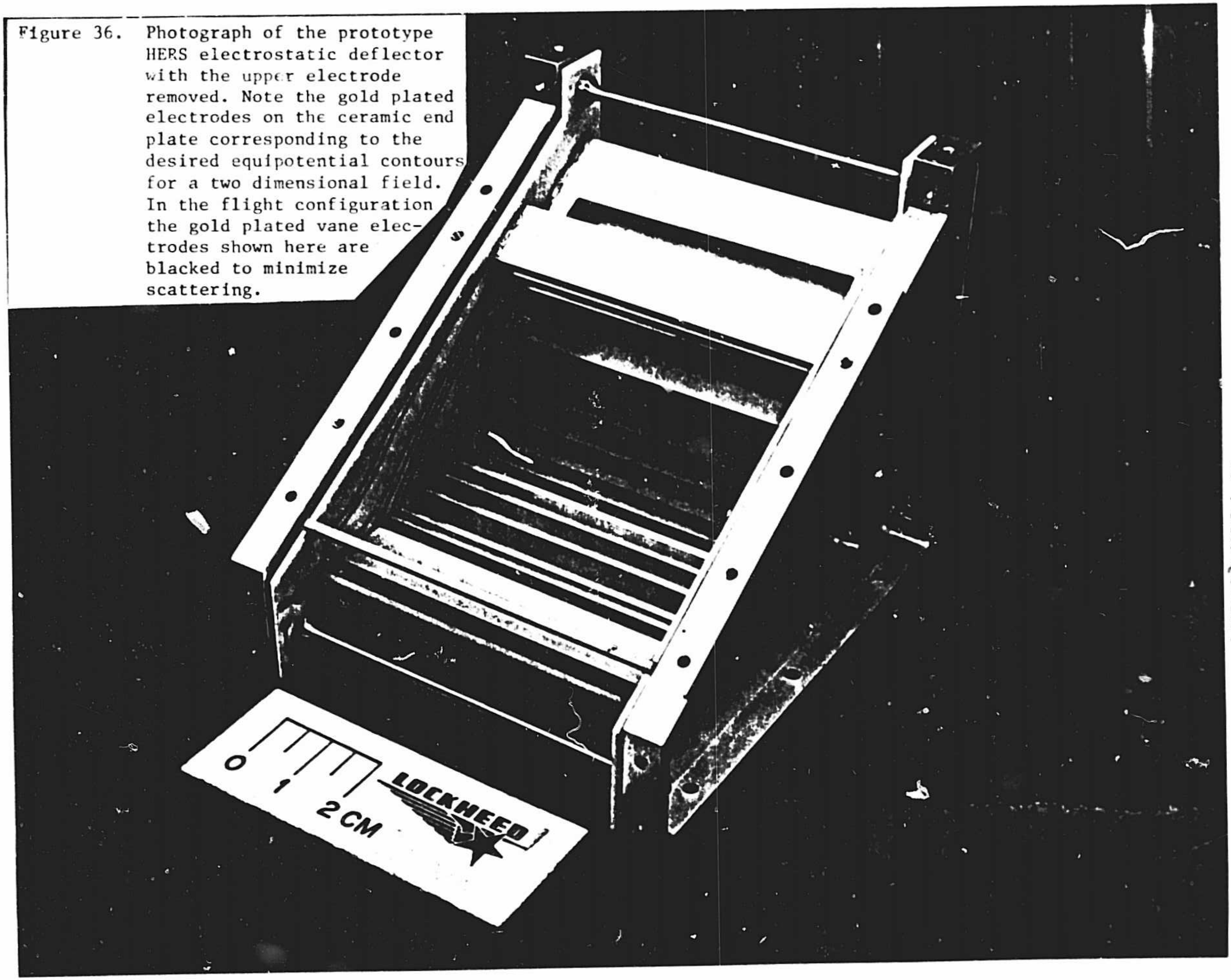

Figure 36. Photograph of the prototype HERS electrostatic deflector with the upper electrode removed. Note the gold plated electrodes on the ceramic end plate corresponding to the desired equipotential contours for a two dimensional field. In the flight configuration the gold plated vane electrodes shown here are blacked to minimize scattering.

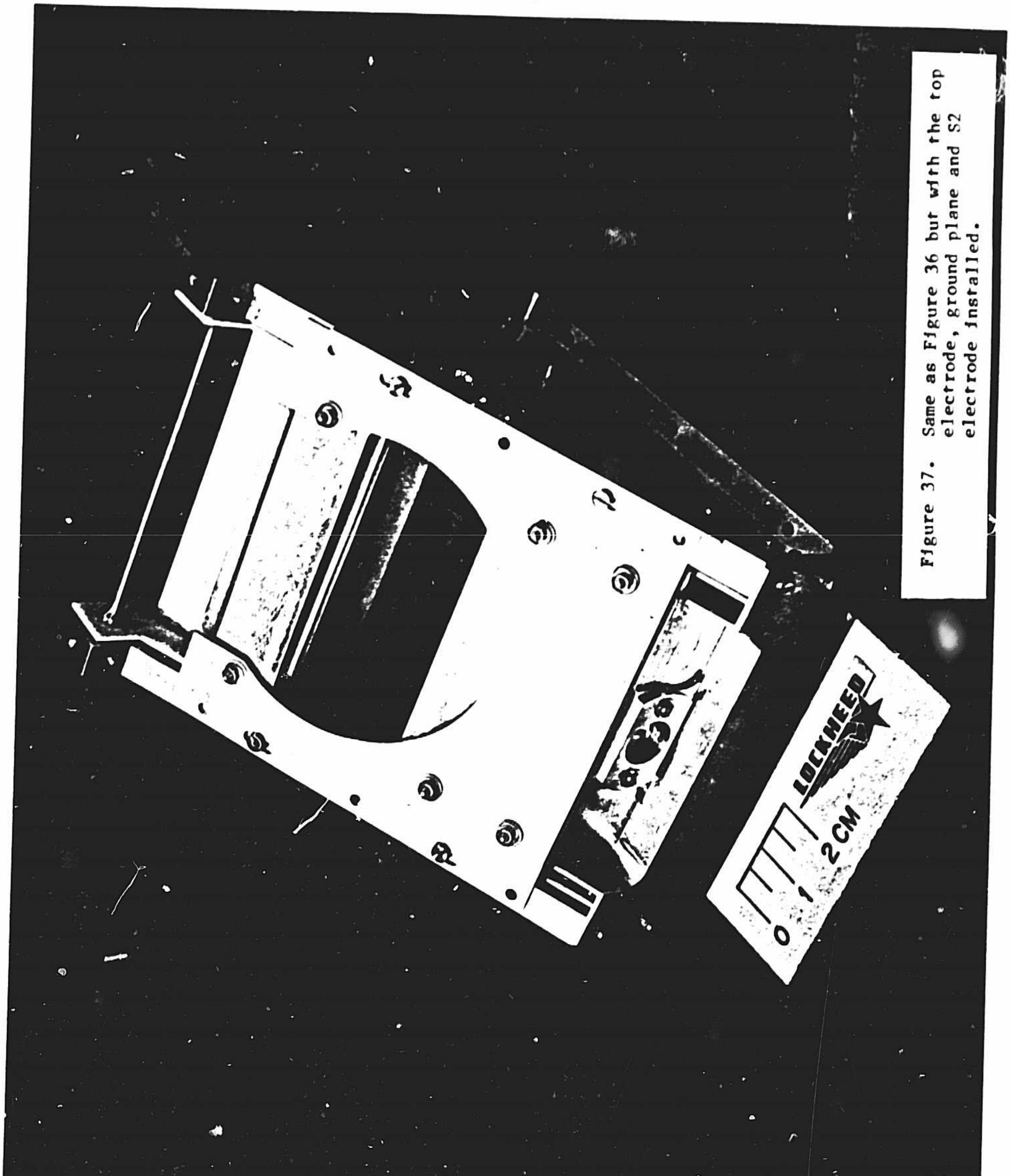

Figure 37. Same as Figure 36 but with the top electrode, ground plane and S2 electrode installed.

2.6.1 Channel Electron Multipliers (CEM)

The CEM detectors were selected for the $m/q = 1$ channel to accomodate the anticipated high count rate due to solar wind protons. It was also desirable to incorporate a separate channel for the protons to avoid the necessity for a facotr to two increase in the ESD voltages which would be required to deflect protons onto the MCP. Figure 38 shows the CEM assembly. The CEMs are standard except for the large (5 mm x 12 mm) rectangular funnels at their inputs. The 5 mm height is adequate to intercept essentially the entire $m/q = 1$ ion peak in the L-mode. The CEM entrance is indicated in Figure 32 by the short diagonal line segment transverse to the $m/q = 1$ ray bundle near its narrowest point. The four CEMs together provide nearly continuous coverage in the angular dimension of the ESD. Each 12 mm wide funnel intercepts approximately 7.5° internally, providing an angular resolution of 15° external to the HERS for protons. Each CEM is provided with a flat mesh screen over the funnel entrance to control the electric field configuration both inside the CEM and between the CEM and the ESD electrode. The CEM high voltage bias (common to the four CEMs) of approximately -3000 Volts is applied to the funnel end. The signal collection is at the ESD signal ground. The CEM data handling is discussed below in conjunction with the description of the HERS detector electronics.

2.6.2 Microchannel Plate (MCP) Detector

The two dimensional imaging detector is a key element in the HERS optics system. As shown schematically on the upper surface of the electrostatic

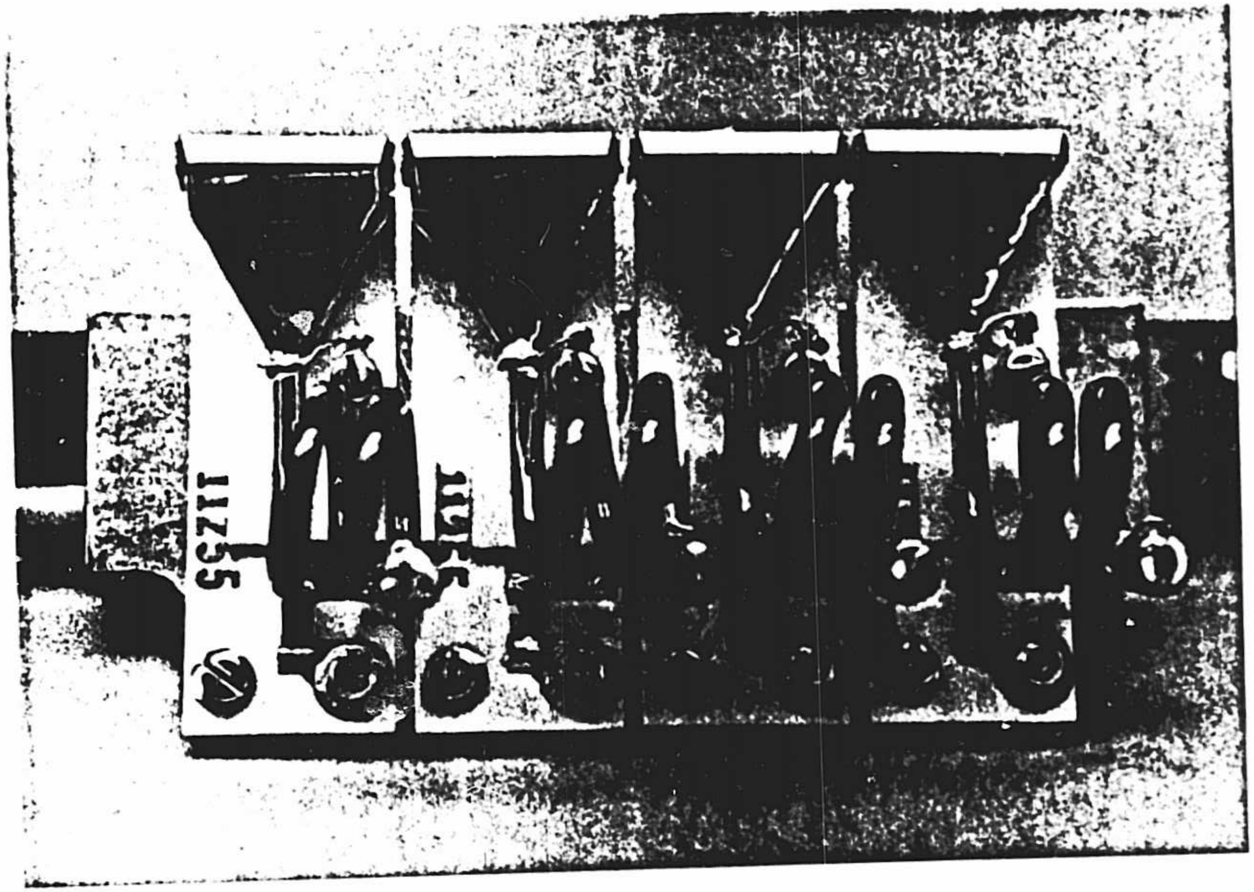

Figure 38. Photograph of the four CEM detector assembly. Ions enter from above.

deflector in Figure 1 and as described in more detail in Section 2.5 of the report, the HERS ion optics focus ions onto this "focal plan" in two dimensions. Mass per charge is dispersed vertically and incident angle is dispersed horizontally.

The detector system resolution must be consistent with the resolution characteristics of the ion optics and must have a high a sensitivity to keV ions. The latter requirs a bare surface multiplier. The obvious candidate for the image intensification, that is a system that can amplify the signal from the single ion to a level consistent with state-of-the-art signal processing, was a microchannel plate (MCP). MCPs are capable of producing gains of the order of 10^6 without significant loss of spatial resolution.

The MCP itself simply intensified the image, it does not detect or encode it. The detection and encoding require some form of two dimensional anode and associated electronics. Several anode systems were considered. Resistive anodes have good spatial resolution but they suffer from a potentially high false encode rate at moderate counting rates. In order to maintain the optical qualities of the HERS at relatively high peak counting rates ($\gtrsim 10^4 s^{-1}$) the system selected has to maintain a false encode rate of the order of 10^{-4} or less. It can be shown that the rate of events N_{AB} resulting from pileup between two event types A and B occuring at rates N_A and N_B respectively with resolving time τ is given by

$$N_{AB} = 2 N_A N_B \tau \qquad (21)$$

Thus without a separate system to identify pulse pileup events, the above requirements translate via equation 21 into

$$\frac{N_{AB}}{N_A} \leq 10^{-4} \text{ and } \frac{N_{AB}}{N_B} \leq 10^{-4} \tag{22}$$

Assume $N_A = N_B = 10^4 s^{-1}$,

$$\frac{N_{AB}}{N_A} = 2N_B\tau \leq 10^{-4} \quad , \tag{23}$$

$$\tau \leq \frac{10^{-4}}{2N_B} = 5 \times 10^{-9} s^{-1} \quad . \tag{24}$$

That is we would require a resolving time of the order of 5 nanoseconds or less. Typical analog ratioing times are of the order of 100 nanoseconds to several microseconds. Thus analog ratioing systems were rejected.

The most straight forward method of avoiding false encoding is the use a two dimensional array of discrete anodes, each with its separate set of detection electronics. The resolution required for the HERS results in 320 pixels. A totally parallel system, which would require 320 amplifier systems, was not considered practical. An alternative system which retains the false encode rejection features of a totally parallel system was selected. This is depicted schematically in Figure 39 and 40. The basic concept is to use the amplified electron signal ($\approx 10^6$ electrons per pulse) collected on an array of isolated anodes for one dimension of the image and to use the electron depletion signal which is residual on the MCP contact anode for the second

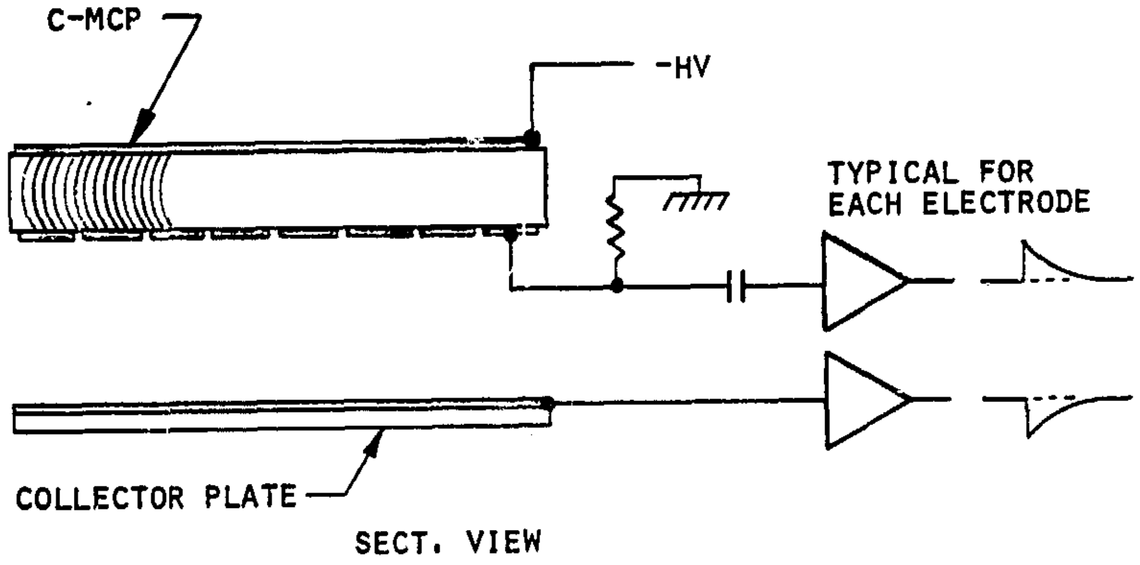

TWO DIMENSIONAL IMAGING USING SEPARATE PLANES (SCHEMATIC)

Figure 39. Schematic view of a cut through a two dimensional imaging system using two separate planes. Electrons are collected on an isolated electrode array and charge depletion signals are collected from the MCP contact electrodes. See Figure 40 for a schematic depiction of the system in the plane of electrode arrays.

TWO DIMENSIONAL IMAGING USING SEPARATE PLANES
(SCHEMATIC)

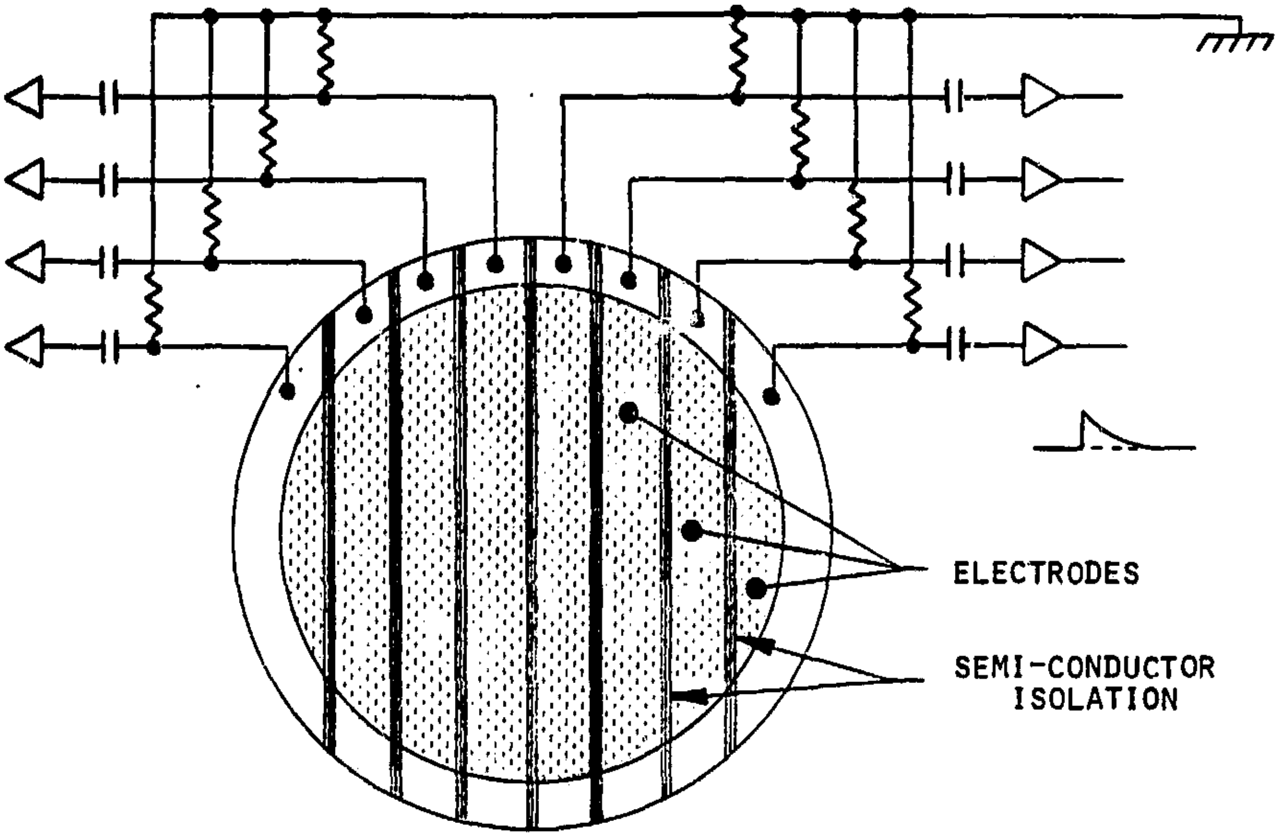

ANODE OF MCP (HORIZONTAL POSITION)

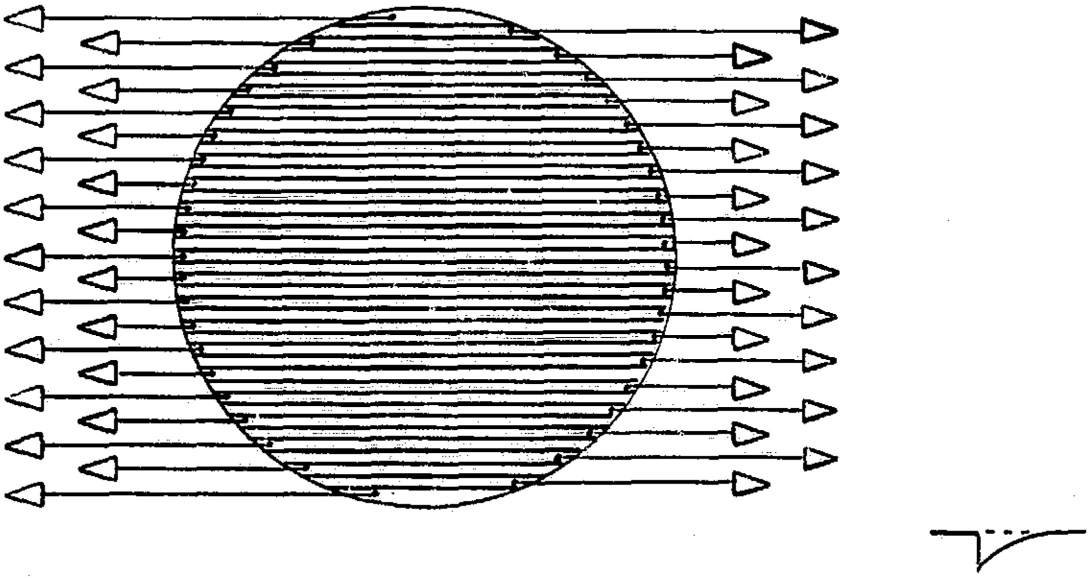

COLLECTOR PLATE (VERTICAL POSITION)

Figure 40. Schematic view of the two planes of electrode arrays. See caption of Figure 39 for more detail.

dimension. By demanding coincidence between signals from one electrode for each dimension but rejecting events with coincidence signals between two or more electrodes on either dimensional plane we can produce an 8 x 40 two dimensional image of 320 pixels with only 48 amplifiers while virtually eliminating false encoding due to pulse pileup. This system is described in more detail in a paper by M. Liptak et al. which is attached as Appendix A.

Figure 41 shows a superposition of the actual two dimensional anode system used in the HERS. One dimension consists of 40 horizontal electrodes oriented such that they intercept signals from all ions of the same mass, independent of their angular coordinate. These electrodes which are metalized onto a ceramic plate are referred to as the mass anode array. A photograph of an actual mass anode array is shown in Figure 42. The 40 individual electrodes are seen in a pattern similar to that shown in Figure 41. The signals collected on these electrodes are carried via metalized holes (seen alternating between the two ends of the electrodes) to the back side the of the mass anode array where they are distributed to electrical contacts (see Figure 43) which ultimately interface with individual charge sensitive preamplifiers. The latter are described in a subsequent section of this report.

Figure 44 shows the 8 element contact anode array (referred to as the angle anodes-array) on the output side of an MCP. Each of these elements intercepts signals from ions of a constant angle of incidence, independent of mass. The tapered pattern reflects the fact that the ions diverge from a common point (S2). Figure 41 shows the fact that the angle anodes extend below the last mass anode. Spring contacts project thorugh the eight holes

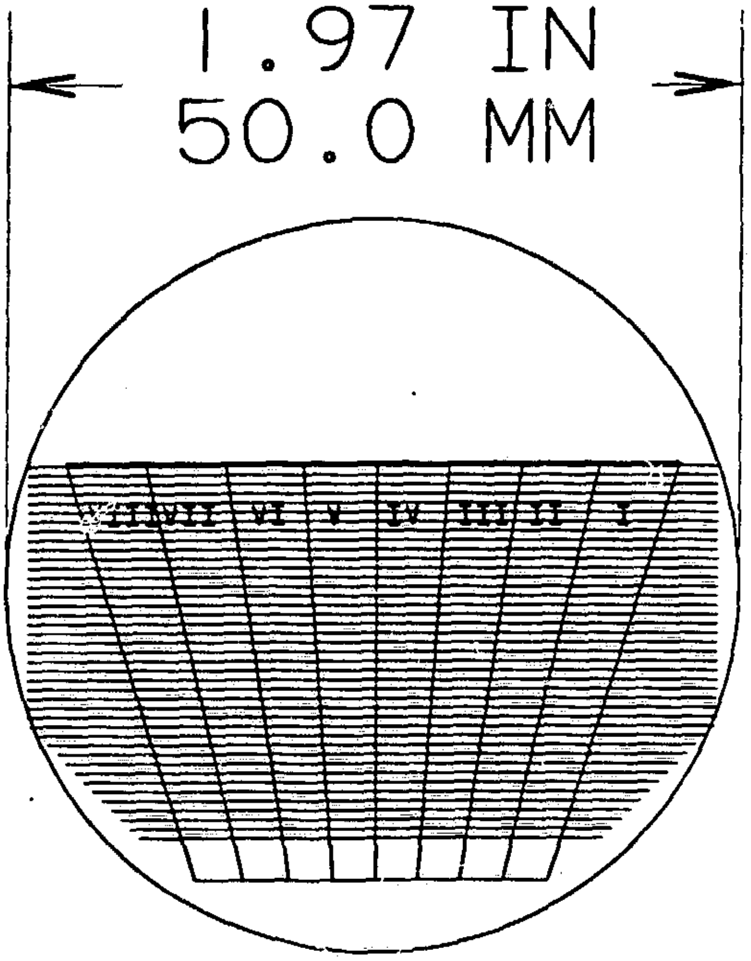

Figure 41. Overlay of HERS MCP imaging electrodes. Horizontal lines show separators between constant mass electrodes and quasi-vertical lines show separators between constant angle electrodes. The former are isolated anodes and the latter are contact anodes.

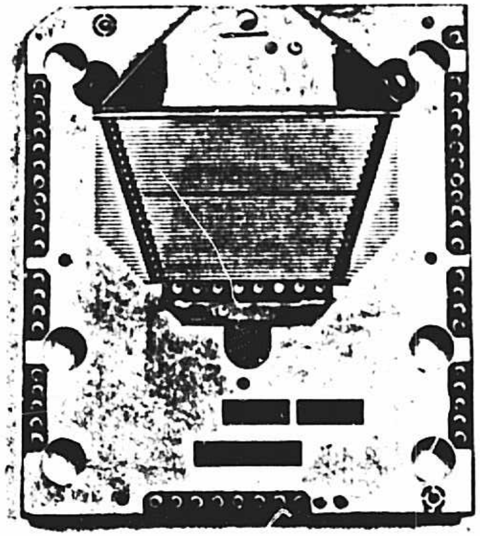

Figure 42. Photograph of actual HERS isloated "mass" anode array. Signals are collected on narrow horizontal electrodes and carried to conductors on back side of the ceramic substrate via metalized holes at ends of electrodes.

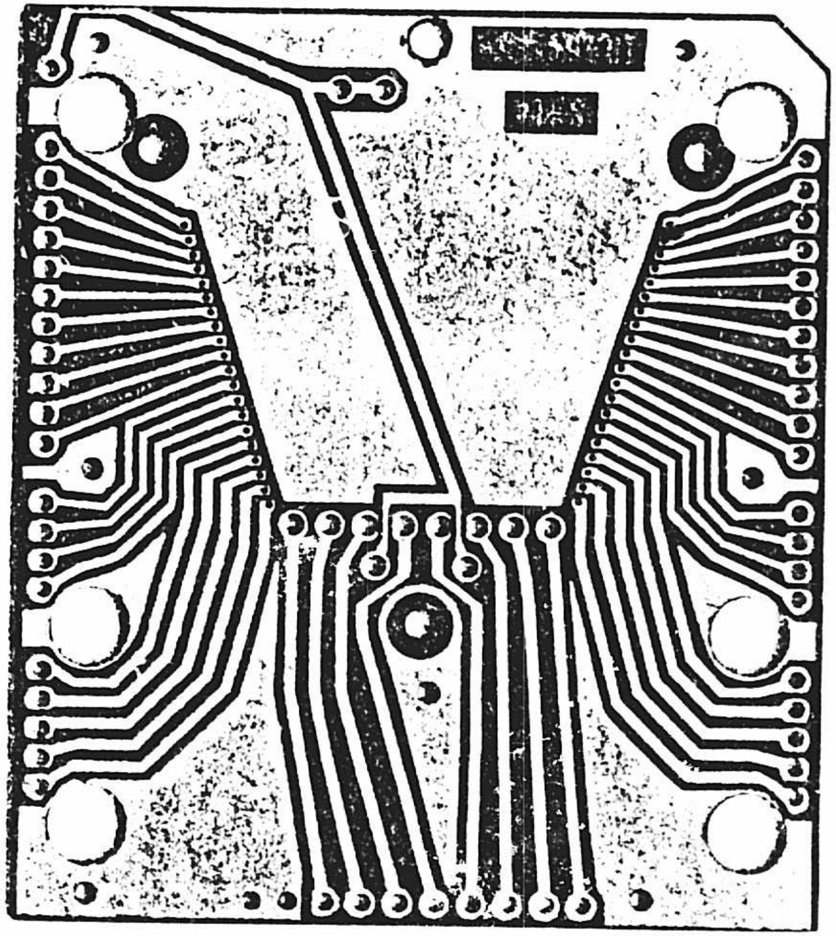

Figure 43. Photograph of back side of "mass" anode showing signal distribution to connectors which interface with the charge sensitive preamplifier assembly. See Figures 2 and 3. The eight conductors running vertically from the bottom connect to the MCP contact anodes via spring contract through the series of holes just below the "mass" anode array.

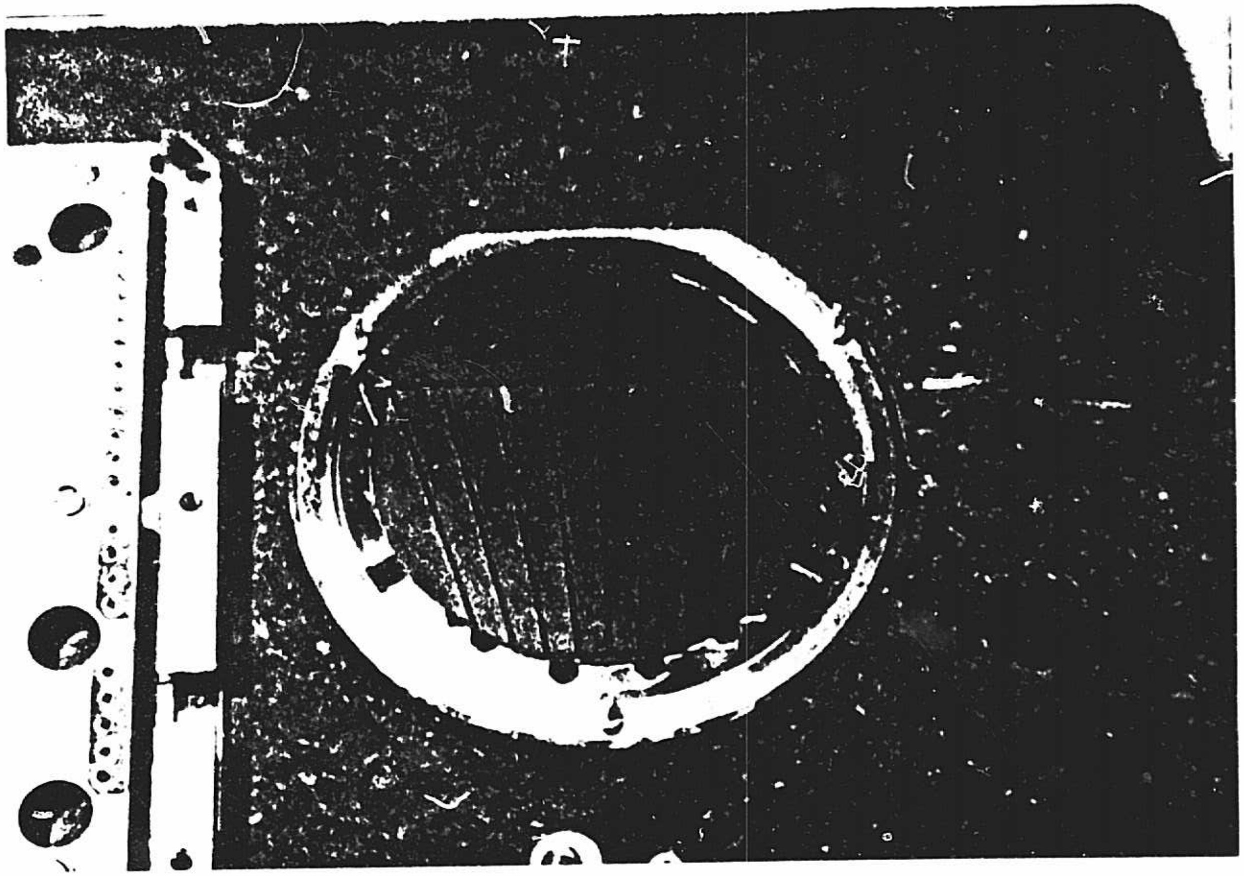

Figure 44. Photograph of the HERS MCP output surface showing contract "angle" anode pattern. The titanium ring clamps the MCP against the ceramic "mass" anode array via the three screws. The thin kapton ring which is visible over the periphery of the MCP isolates the "angle" anodes from the "mass" anodes.

aligned along the bottom of the mass anode array (see Figure 42) to connect the individual angle anodes to their respective charge sensitive preamplifiers (see Figure 43).

The MCP is clamped to the mass anode array plate by the titanium ring and three screws seen in Figure 44. On close inspection of Figure 44 a transparent insulating ring which projects inward from the clamp ring is also visible. This thin (≈ 0.1 mm) insulating ring sets the spacing between the angle anodes and the mass anodes. This narrow spacing, across which a potential of approximately 50 Volts is applied, is required to minimize charge spreading in the electron cloud which exits the MCP and is collected on one of the mass anodes. Excessive charge spreading results in signals being detected on two anodes and consequent rejection.

The complete MCP-Anode assembly is shown in Figure 45. This assembly connects directly to the ESD below (see Figure 37) and the preamplifier assembly above (See Figure 2 and 3).

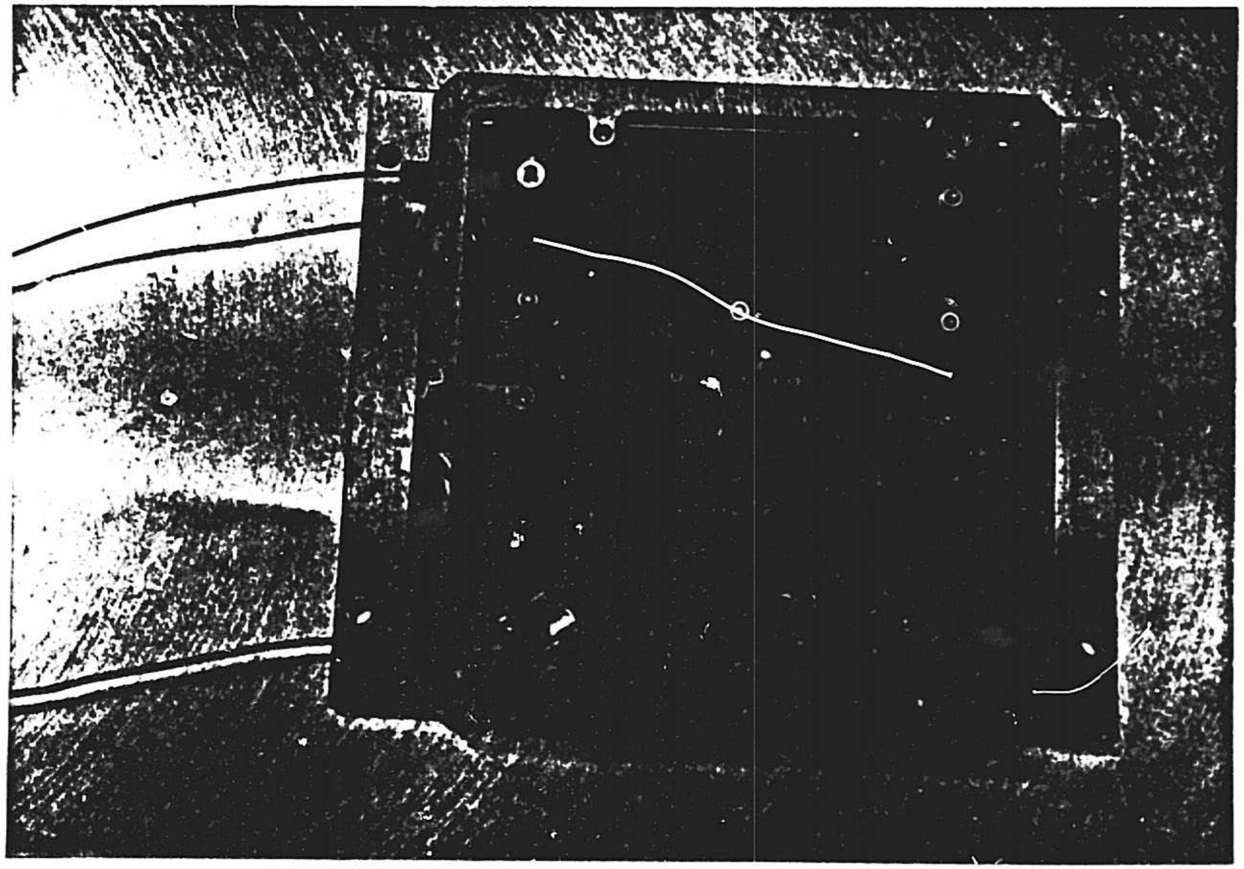

Figure 45. Photograph of the MCP, Mass Anode Assembly ready to mount onto the HERS electrostatic deflector. See Figure 37.

2.7 Image Encoding Electronics

The GIOTTO IMS instrument is comprised of three major assemblies, IMS-3, IMS-2, and IMS-1. The IMS-3 serves as the spacecraft interface; switching low voltage power, formatting and passing all commands and data between the spacecraft and the two measurement instrument heads called the High Intensity Spectrometer (HIS) IMS-2, and the High Energy Range Spectrometer (HERS), IMS-1. The IMS-3 also performs a sorting algorithm to compress the data rate. The HERS ion optics and sensor electronics were implemented by LPARL. For this section of the paper, the electronics are divided into two areas: that provided by the Max Planck Institute for Aeronomie (MPAE) including high and low voltage power, command and data interfacing with IMS-3; and the Lockheed Palo Alto Research Laboratory (LPARL) section which includes sensors output control, conditioning, and event encoding.

The block diagram in Figure 46 illustrates the major elements and their organization within the LPARL system. The details of MCP signal conditioning electronics are divided into three partial schematics called "analog conditioning", "coincidence logic and encoding", and "data output", and are shown in Figures 47, 48, and 49 respectively.

The following is a description of the sensor's electronics processing designed by LPARL. For a minimum period of 1 spin (4 seconds), the system operates exclusively using either the micro-channel plate (MCP) or channel electron multiplier (CEM) outputs, depending on the ion type being measured. If the CEM mode is selected, all MCP events are inhibited and the CEM preamps are powered. This configuration outputs proton events over four elevation angles. The four conditioned CEM outputs are transmitted as they occur directly to

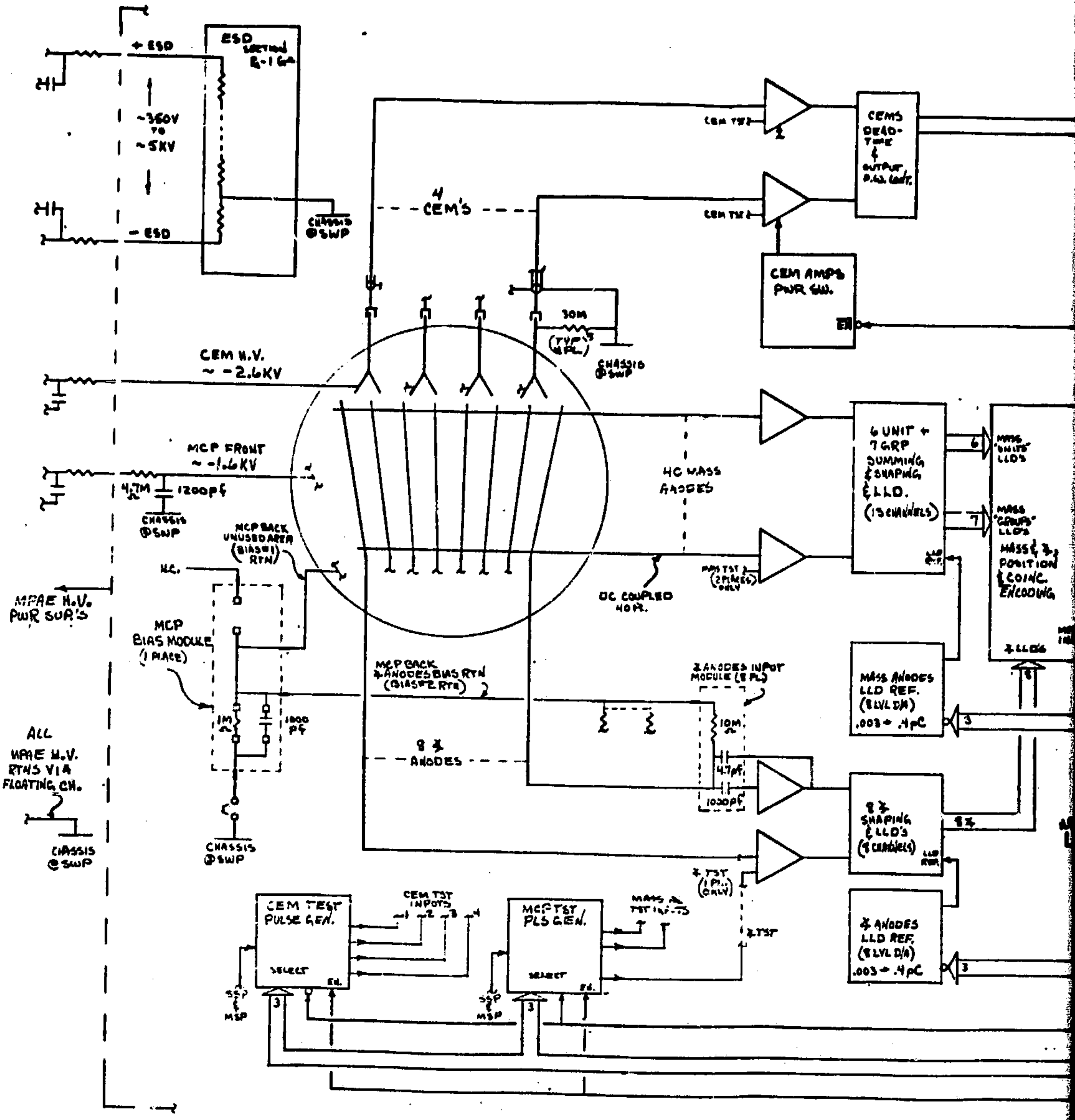

FOLDOUT FRAME

ORIGINAL PAGE IS
OF POOR QUALITY

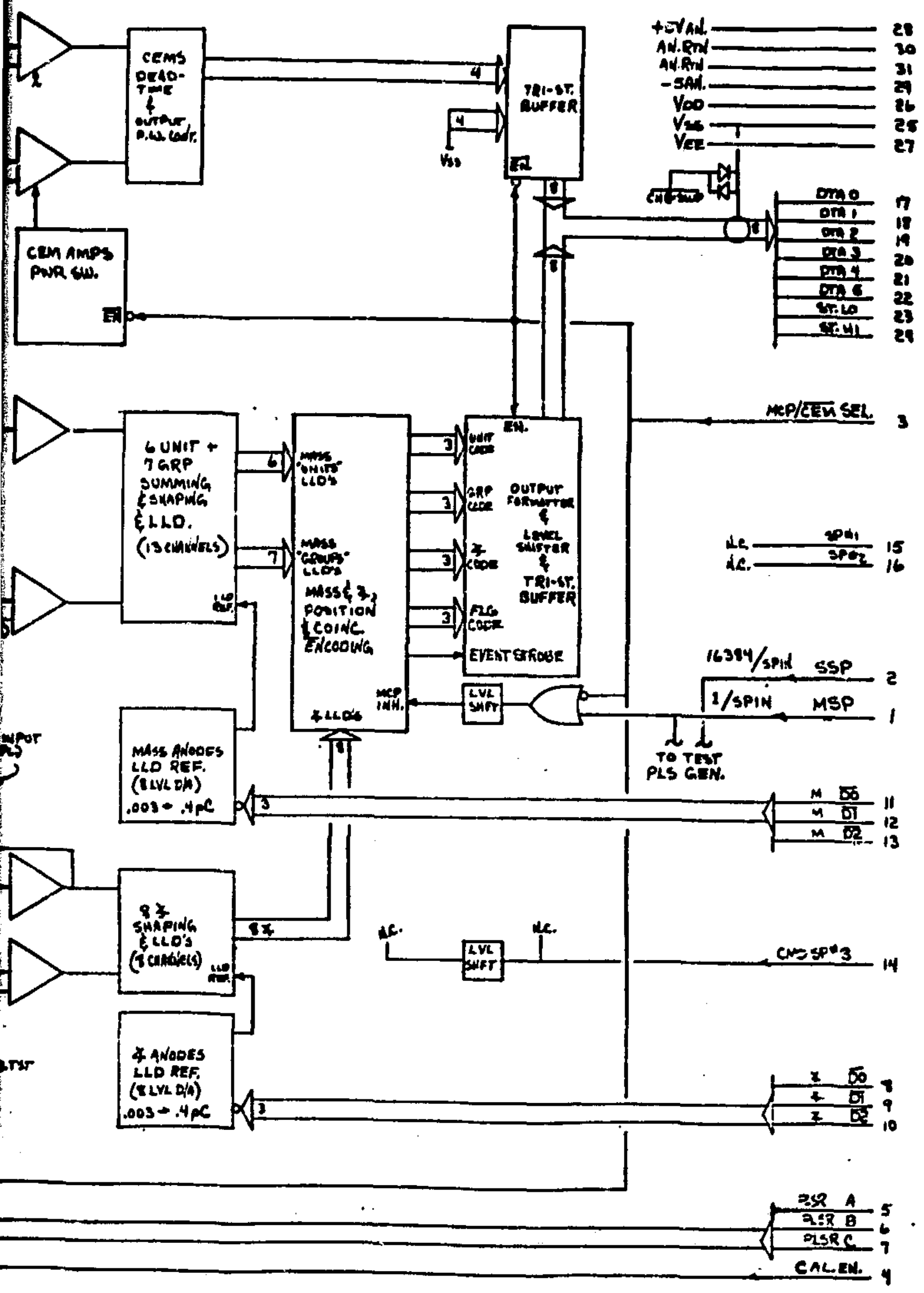

FOLDOUT FRAME 2

Figure 46: Block diagram of LPARL sensor signal conditioning.

ORIGINAL PAGE IS OF POOR QUALITY

ORIGINAL PAGE IS
OF POOR QUALITY

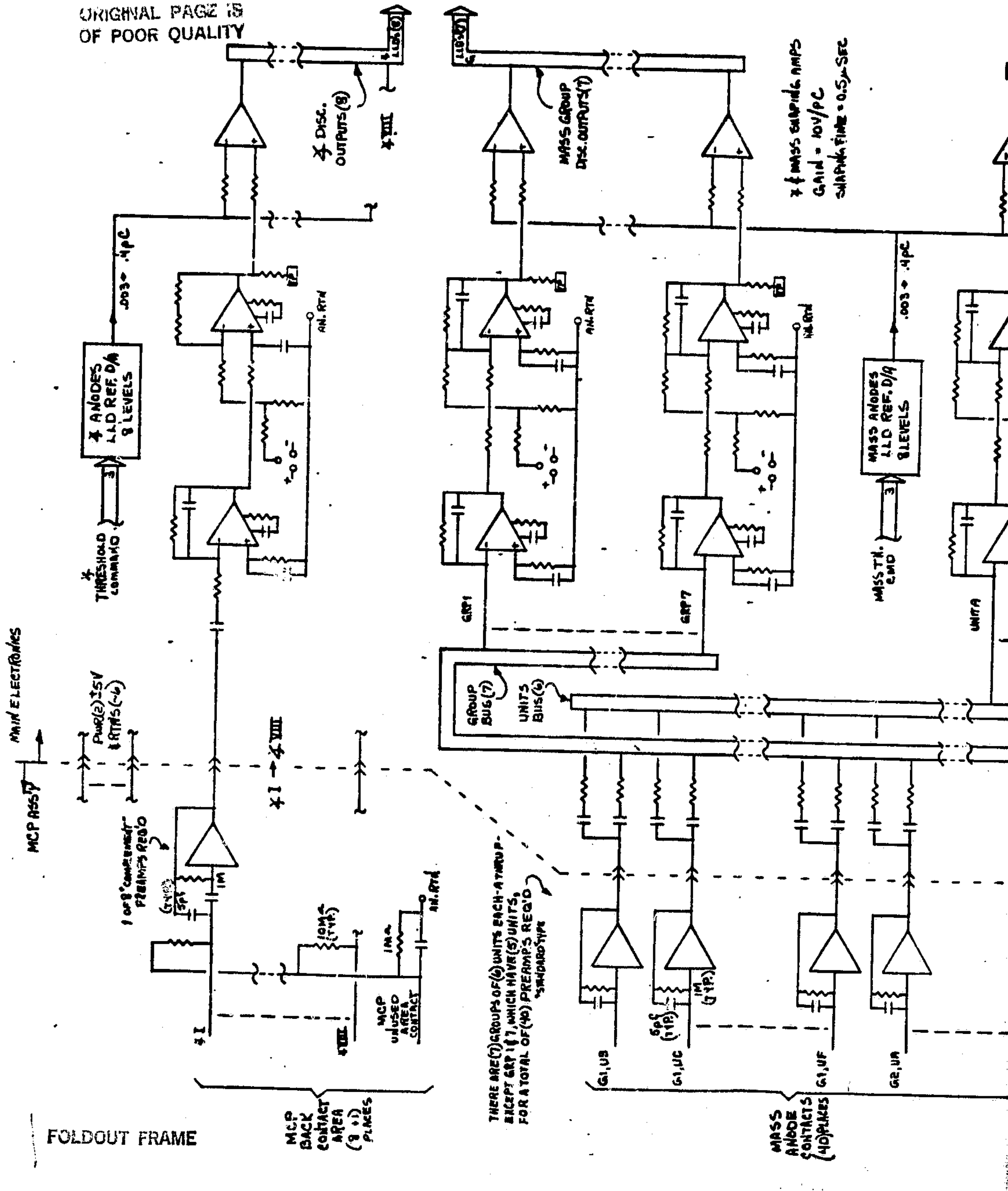

FOLDOUT FRAME

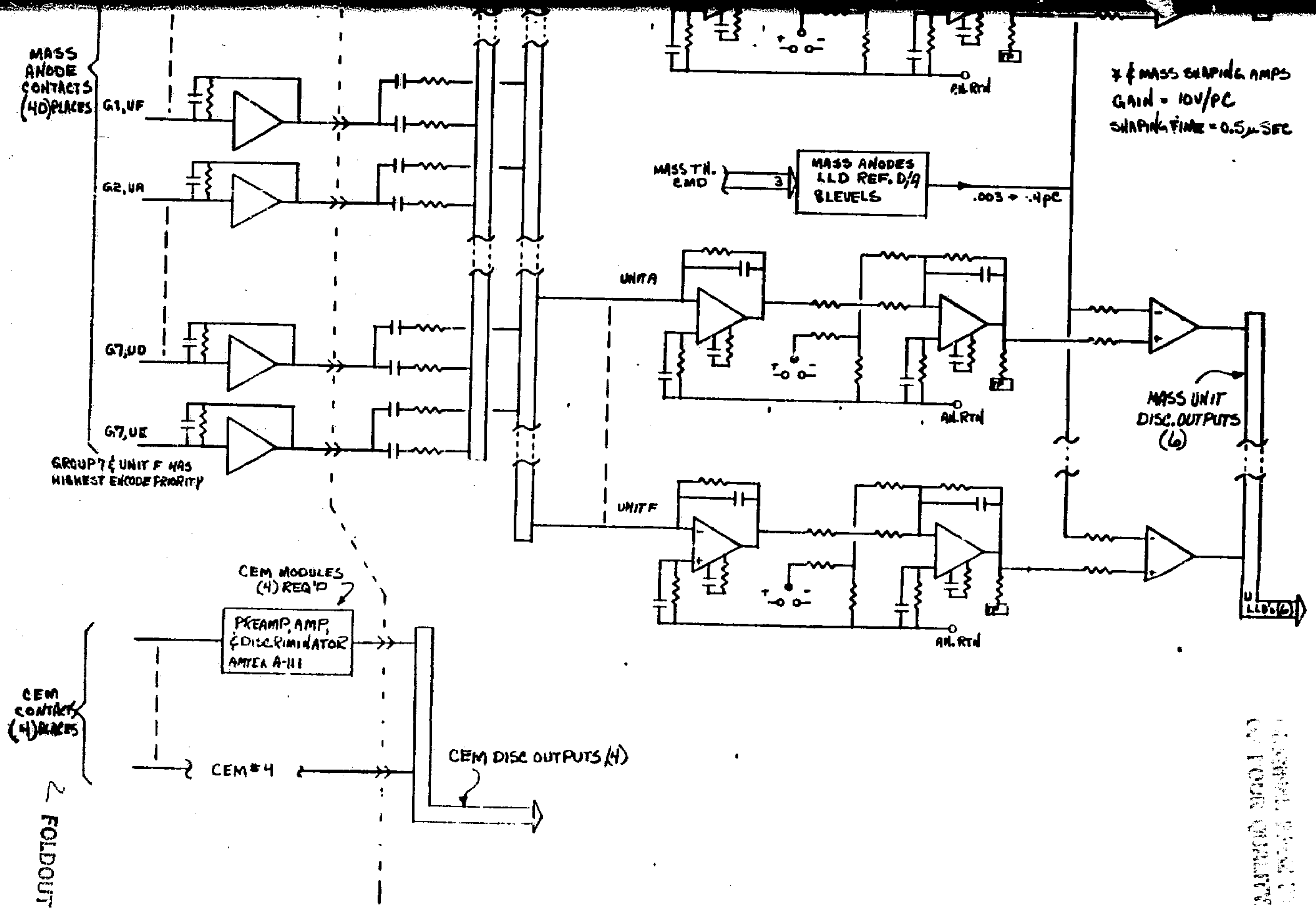

Figure 47. Partial schematic for the analog signal conditioning.

2 FOLDOUT FRAME

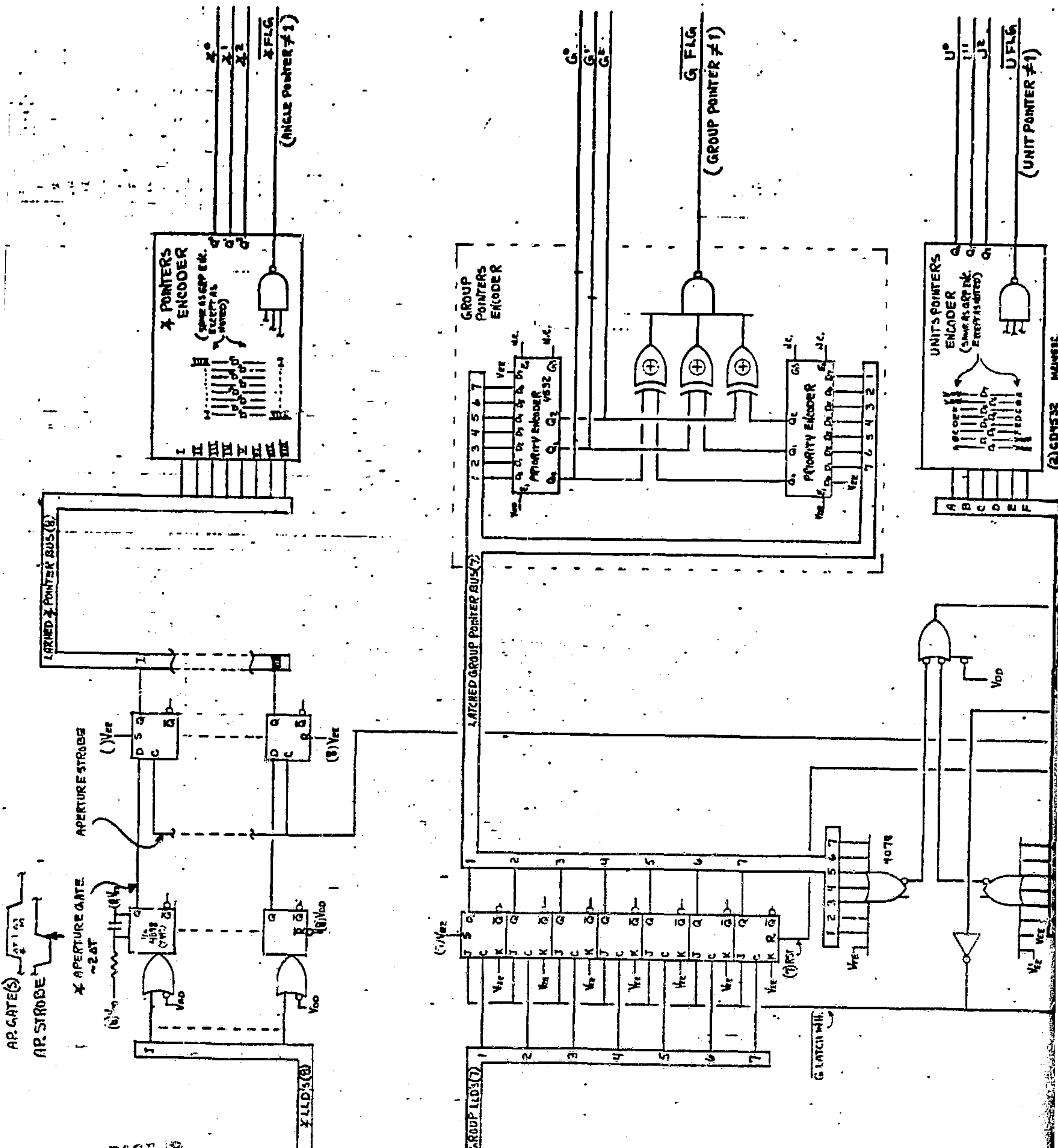

ORIGINAL PAGE IS
OF POOR QUALITY

FOLDOUT FRAME

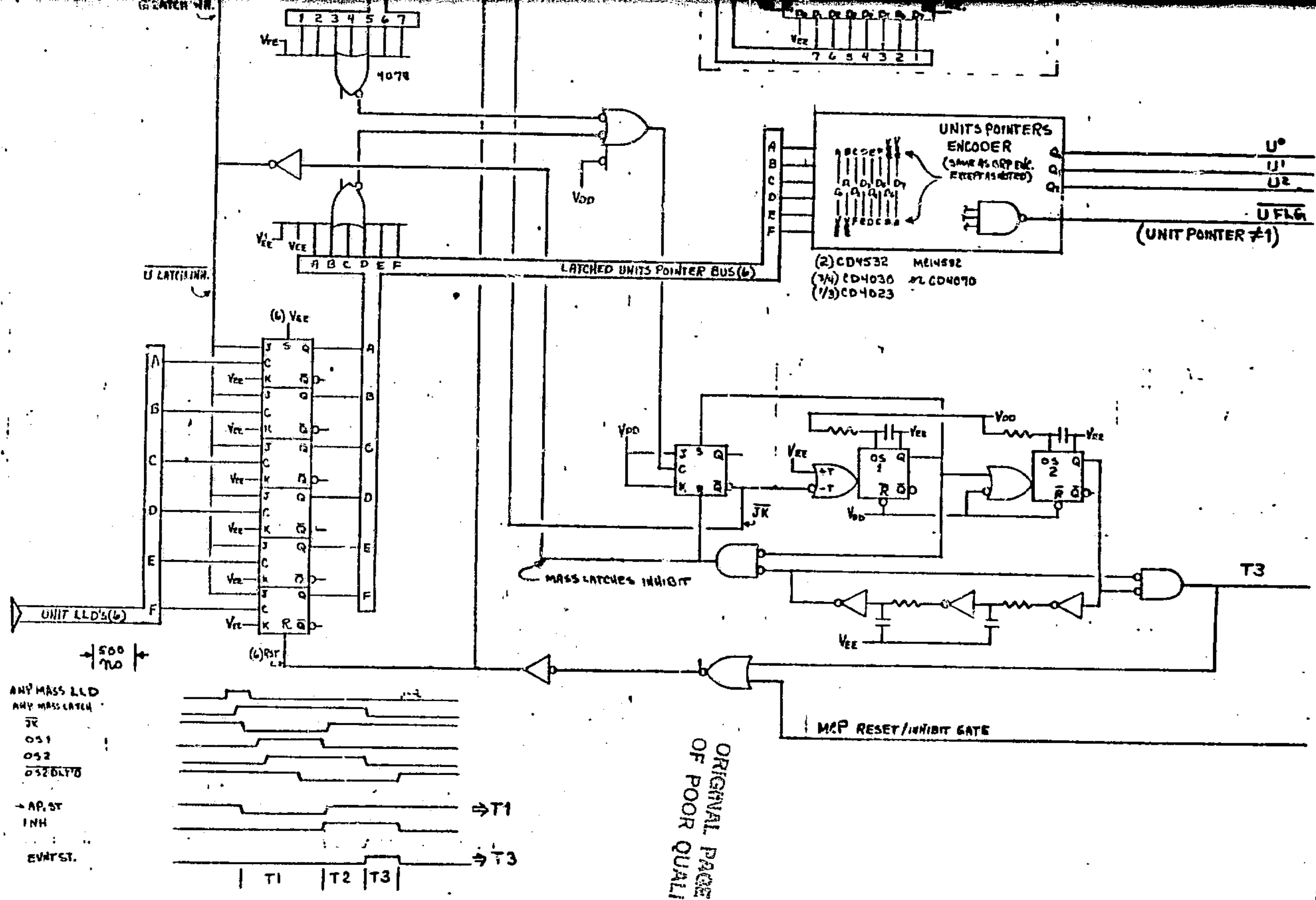

ORIGINAL PAGE IS
OF POOR QUALITY

FOLDOUT FRAME

2

Figure 48. Partial schematic for the coincidence and encoding logic.

ORIGINAL PAGE IS
OF POOR QUALITY

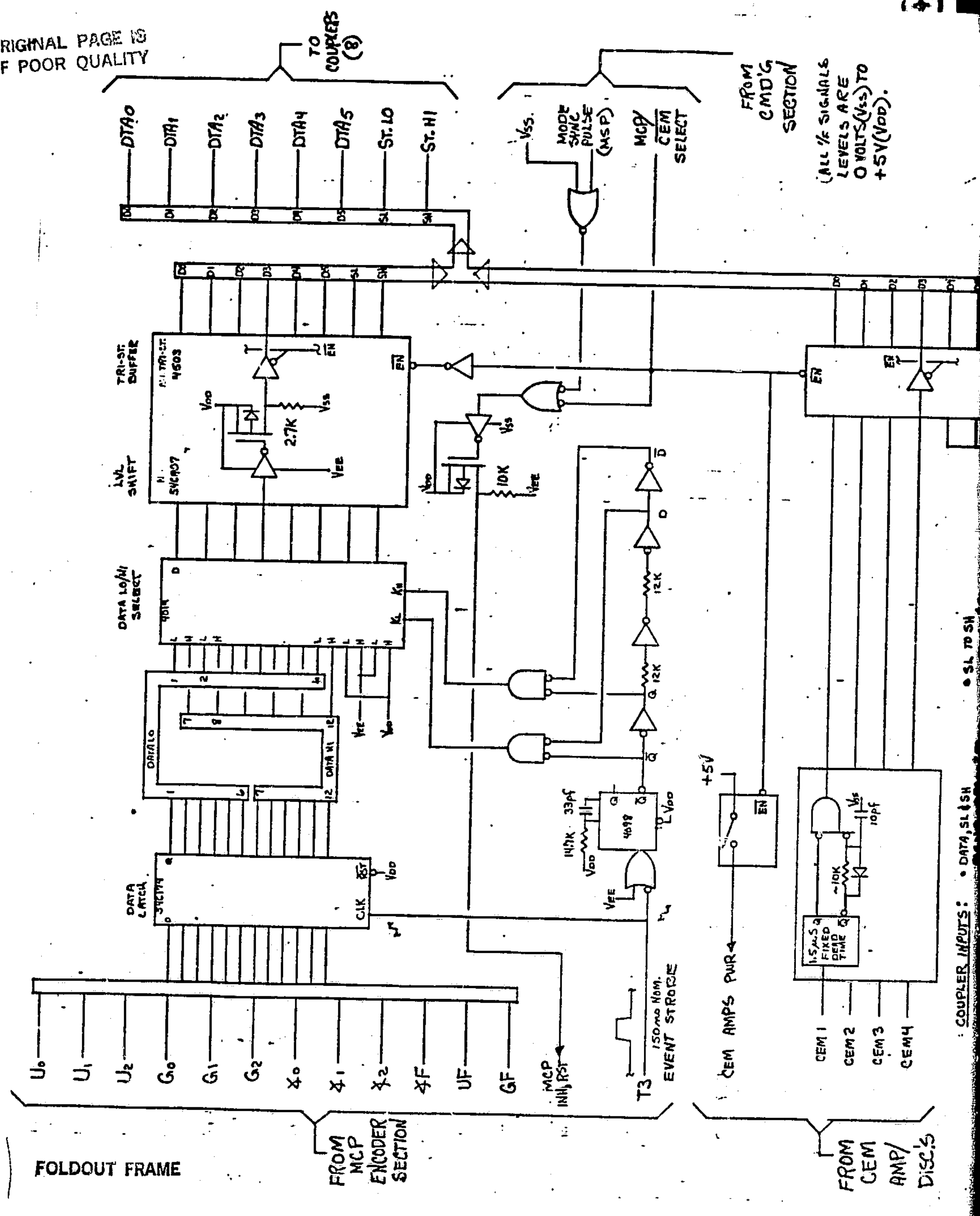

FOLDOUT FRAME

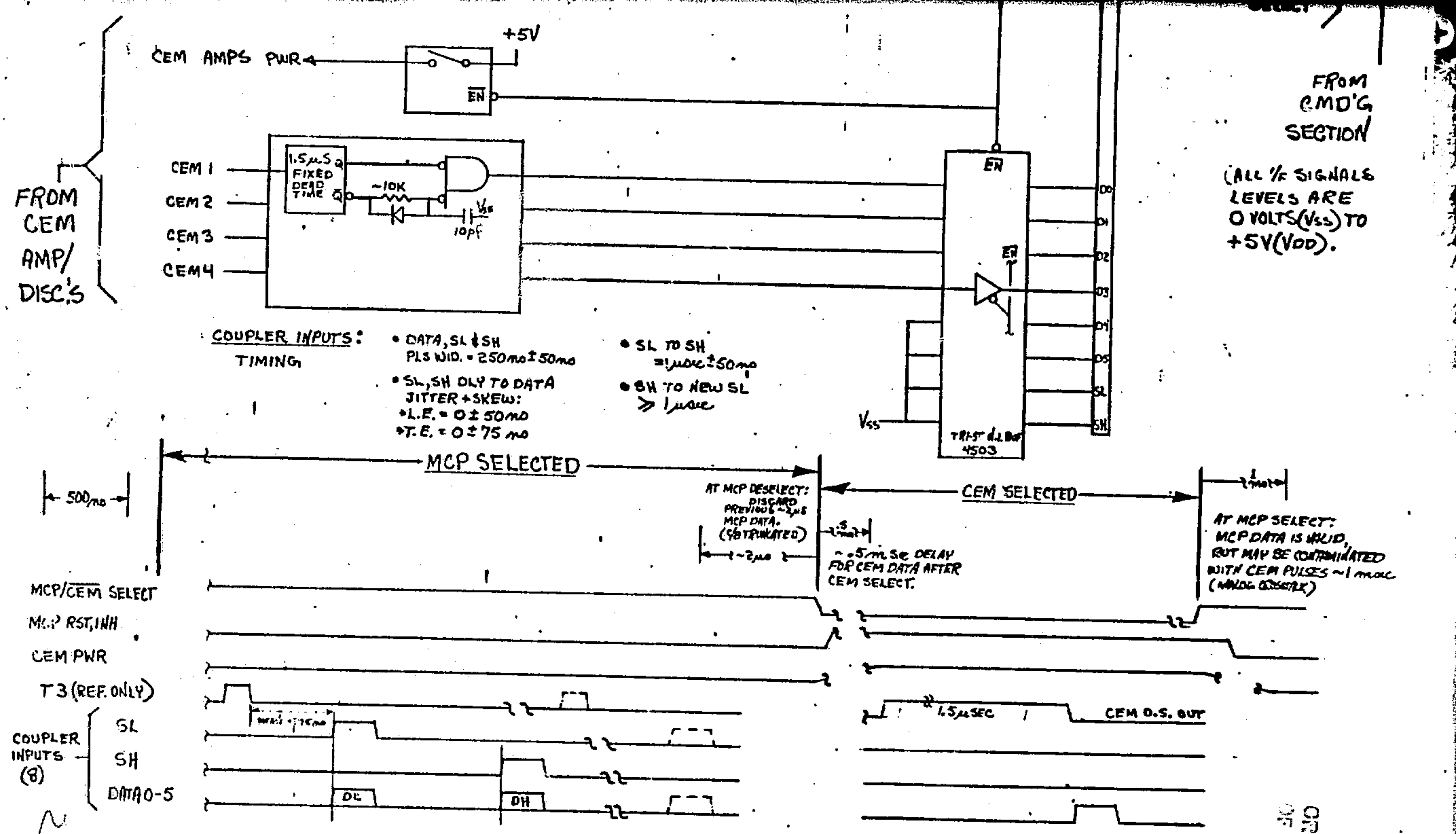

FOLDOUT FRAME

Figure 49. Partial schematic and timing diagram for data output section.

accumulators within IMS-3. The threshold and dead time are 0.1 pC and 1.5 usec respectively. The single CEM high voltage provided can be commanded to one of four values.

When the MCP mode is selected, the "MCP INHIBIT" is removed and the data output system is dedicated to the MCP sensor. As described in the last section the MCP outputs consist of 40 mass anode signals and 8 angle anode signals. the overlay of the mass and angle anode arrays is shown in Figure 41.

Given that certain constraints are observed in the manufacture of the MCP, there is a dominant induced charge produced at the contact anode output of the plate by the exit of the negative charge. Thus most events seen on the mass anode strips as negative charges produce a time correlated inverted replica at the appropriate angle anode.

Individual charge coupled preamps are used at each anode strip to control electrical crosstalk. Because of the slew rate assymetry inherent in this preamp design, the 8 angle preamps were nearly identical to those used for the 40 mass anodes, but all transistors are exchanged for a complementary type to enhance the negative output slew rate.

Figure 50 shows the preamp configuration used for the mass anode strips. The high open loop gain and bandwidth of this design in combination with heavy feedback (4.7 pf & 1 M) results in an adjacent strip rejection ratio > 200 when an integration time of .5 usec is used for the output shaping. (This measurement was based on an estimated worst-case strip-to-strip capacitance of 10pf, and a tail time constant of 5 usec for the preamp feedback network.)

The 40 mass anode signals are processed in the shaping amplifiers in such a way that the number required to encode the position is reduced to 13. This is accomplished by creating 7 "coarse" and 6 "fine" amplifier channels called here "groups" and "units." Every mass preamp output is terminated to both a group

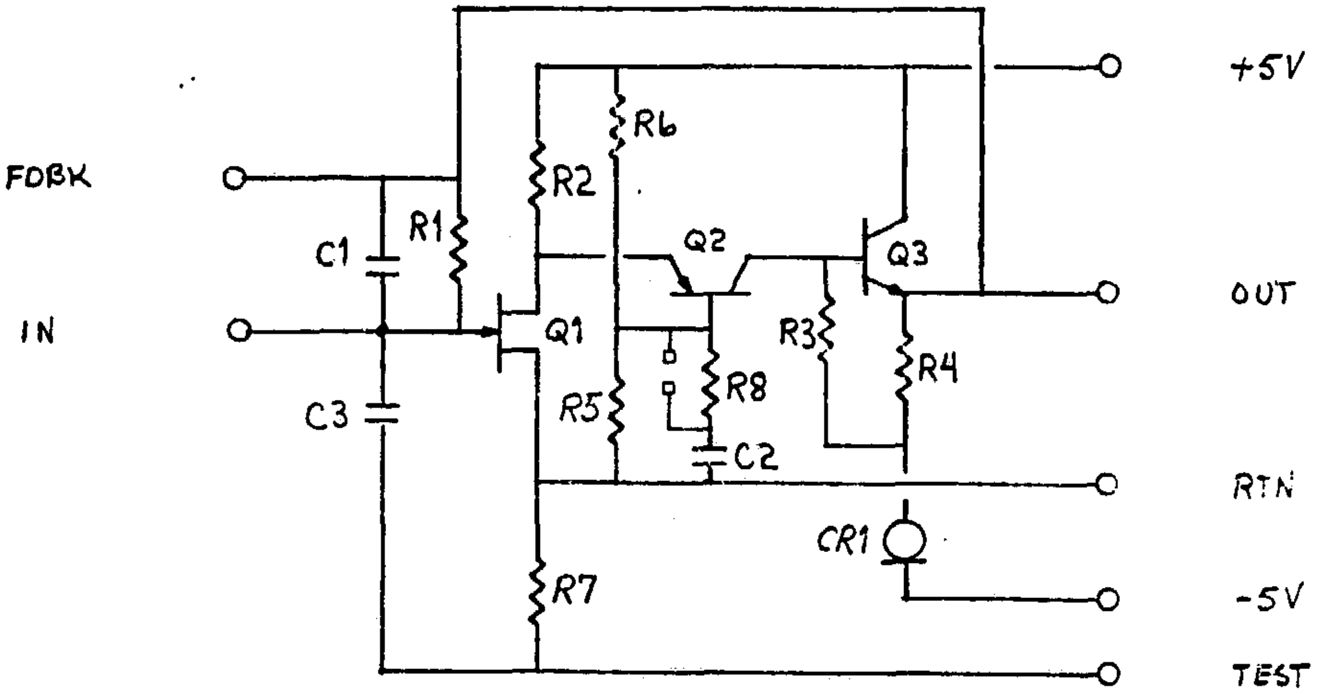

Figure 50. Schematic diagram of charge-coupled preamplifier hybrid.

and a unit channel. It is important to note that a complete mass event produces two elements, a group and a unit. The 13 group or unit amplifiers are configured as summing amplifers and each output is terminated into a programmable comparator, here called a Low Level Discriminator (LLD). Figure 47 details this part of the system.

The eight angle anode signals are each processed individually and are therefore terminated into eight LLD's. Two independently commanded reference D/A converters are provided, one for the 13 mass LLD's and one for the 8 angle LLD's. Each reference requires a 3-bit code to define 8 levels, and each level is twice the preceding one. The range is 128:1, and the minimum threshold is equivalent to .003 pC.

At this point in the processing, an ideal single event produces 3 LLD outputs to define the event position on the MCP: the mass component (group and unit), and the angle component. The time interval between the rising edge of these three outputs may be skewed because their relative threshold crossing time is effected by their relative amplitude variations (for the 0.5 usec shaping constants used, this period is less than 1 usec). Multiple events appearing within this interval, charge spreading, and/or electrical crosstalk responses will produce multiple unit, group, or angle element responses. Marginal amplitudes near the programmed thresholds may cause one or more of the elements to be missing.

The event processing which follows the LLD outputs is primarily digital. It is in this section that the mass and angle position and coincidence encoding is accomplished. The result is a 12-bit word which is available approximately 2 usec following the first mass LLD threshold crossing. The data are then transmitted sequentially as a pair of 6-bit words in the following 2 usec. This procedure is "pipelined," i.e., a new event may be processed while the old one is being outputted. The implementation of this section is presented in the two schematics shown in Figure 48 and 49.

The strategy used within the event position and coincidence encoding logic is discussed below.

Any event trial can be originated only by a mass comparator (MASS LLD) rising edge, from either a group or unit element (a MASS LLD response is latched and stored in an edge triggered flop). The trial begins by allowing a "Mass aperture" for the other element of the mass anode signal to appear. Nearly simultaneous unrelated events may also be latched (stored) during this interval, which is 1.0 usec long. At the termination of this interval, all further mass anode inputs are inhibited. Also the state of each of the eight "angle aperture" gates is tested for coincidence, and the result latched. (Each of the eight angle anode outputs is configured as a separate, independent channel, and each angle LLD positive threshold crossing generates a fixed, retriggerable pulse output called the "angle aperture" whose period [2 usec] and position accomodates the time skew limits between a related angle and mass anode event.)

At this time, all the information of the event is available and stable, consisting of single, multiple, and/or missing elements for both mass and angle position. These states are encoded and logical flags are set to qualify these encoded states. After a short interval to allow the logic outputs to settle, these data are stored for outputting, and the logic is cleared to accept a new event for a trial.

The data are stored as a 12-bit word, organized into four segments of three-bits each. The first segment contains three condition flags, one each for angle, group, and unit respectively. These are required to interpret the binary encoded positions contained in the remaining three segments. The second segment describes the elevation angle position, and the third and fourth define the coarse (group) and fine (unit) mass anode position.

The flags are used in the following way: if a flag is OFF, the code segment that it qualifies is interpreted directly as position. If the flag is ON, and the associated code equals zero, that component of the event position is missing. If that flag is ON, and the associated code is not equal to zero, that component of the event contains multiple positions. When an event or events produce a multiple position, the higher numbered position is given priority and is the value encoded.

Test pulse generators are included for both the CEM and MCP electronics and are input at the preamplifiers. The CEM test pulses may be commanded to one of the four CEM channels, and the amplitudes are fixed to alternate between two levels; .5 and 1.5 times the CEM amplifiers threshold level at a rate of 1024 pulses/second. The MCP test pulses may be commanded in any combination to two mass anodes. The amplitude is fixed at a single value slightly over the third threshold (~ .012 pC), and the rate is 64 pulses/second. The pulse pattern can be altered to produce simulated mass events with multiple, single or missing elements to exercise the encoding and coincidence logic as well as doing a cursory check on the analog thresholds.

The MPAE portion of the system produces a calibration procedure requiring 32 spins (128 seconds) to complete. This sequence programs the test pulse generator outputs, the MCP mass and angle anode LLD thresholds, and the CEM high voltage settings. These automated sequences, in conjunction with the ability to alter the "fixed" parameters between successive calibration procedures, should improve our ability to identify changes in the sensor and electronics after launch, as well as provide an obvious benefit for pre-launch testing activities.

The LPARL systems as described above requires +/- 5 volts and 850 mwatts static power. The hardware is divided into two sections: the preamplifiers, which are mounted immediately above the MCP, shown in Figures 2, 3, and 4. The signal and power are connected to the main electronics box via a pair of flexible harnesses, along with the four CEM signal coax leads.

The main electronics box is shown in Figure 51, and is comprised of eight circuit boards illustrated in Figures 52 - 59. AB1A and AB1 are dedicated to the mass preamps output signal routing, and the mass anodes amplifiers (summing and shaping) respectively. AB2 contains the two programmed D/A converters and eight shaping amplifiers for the angle anodes. AB3 has the LLD'S for the eight angle anodes and four CEM amplifiers with their power supply switches. AB4 contains the thirteen LLD's required for the mass anodes processing.

The digital and interfacing circuitry is on DB1 and DB2. DB1 contains all the coincidence timing and encoding logic. DB2 contains the sections for the conditioning of the four CEM outputs, and generating the programmed test pulses for both the CEM and MCP preamps. The logic level shifters and all interface buffers and receivers between the MPAE and LPARL electronics are on DB2 also.

MB1 is the motherboard which in addition to its obvious function of providing power, ground and signal interconnects, contains most of the ground and power fault clamp diodes and grounding configuration jumpers.

2.8 Sensor Characterization

The MCP and associated electronics without the optics were tested at LPARL using a nickel 63 beta emitting radioactive source to uniformly illuminate the MCP, see Figure 60, and an ultra-violet lamp (U. V.) as a spot source ~ 2.5 mm in diameter at the MCP, shown on Figure 61. The U. V. spot was scanned across

ORIGINAL PAGE IS
OF POOR QUALITY

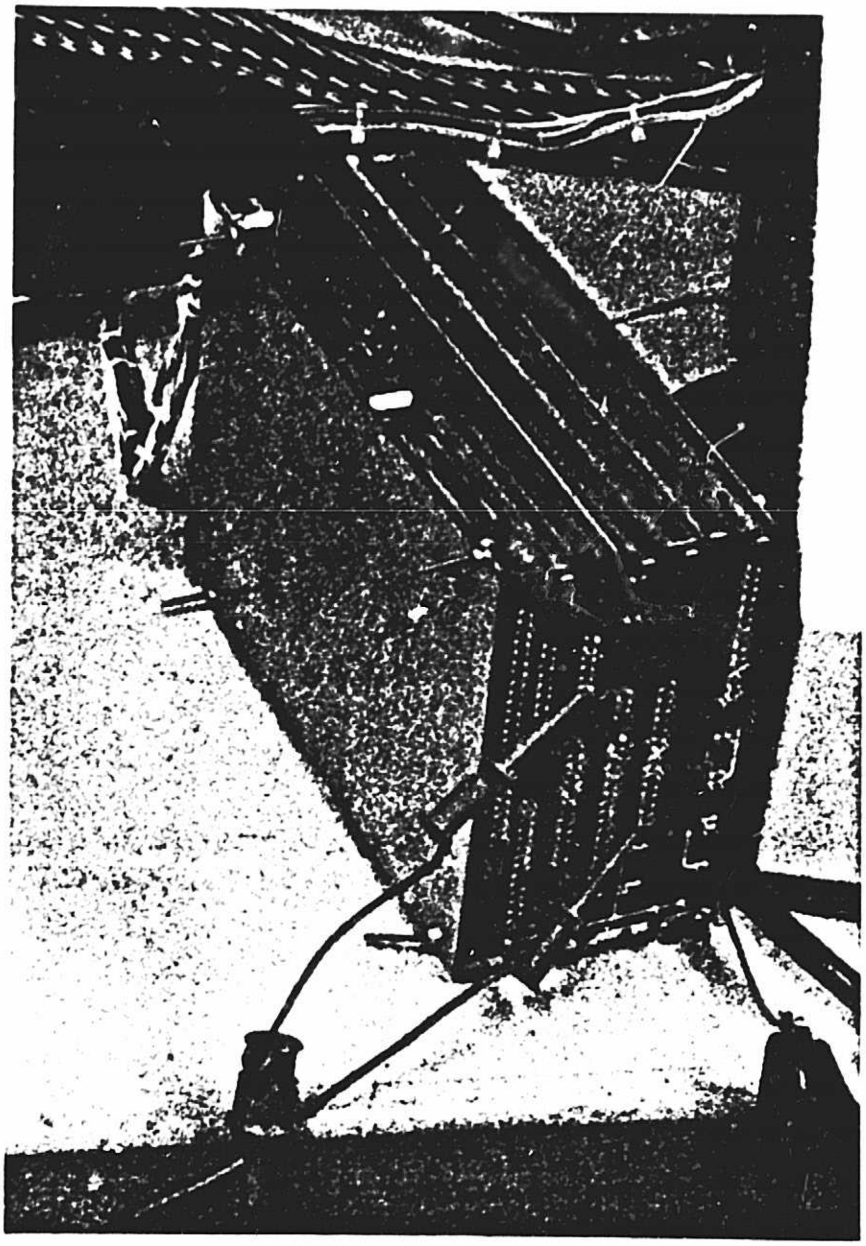

Figure 51. Main electronics signal conditioning system shown here during initial testing.

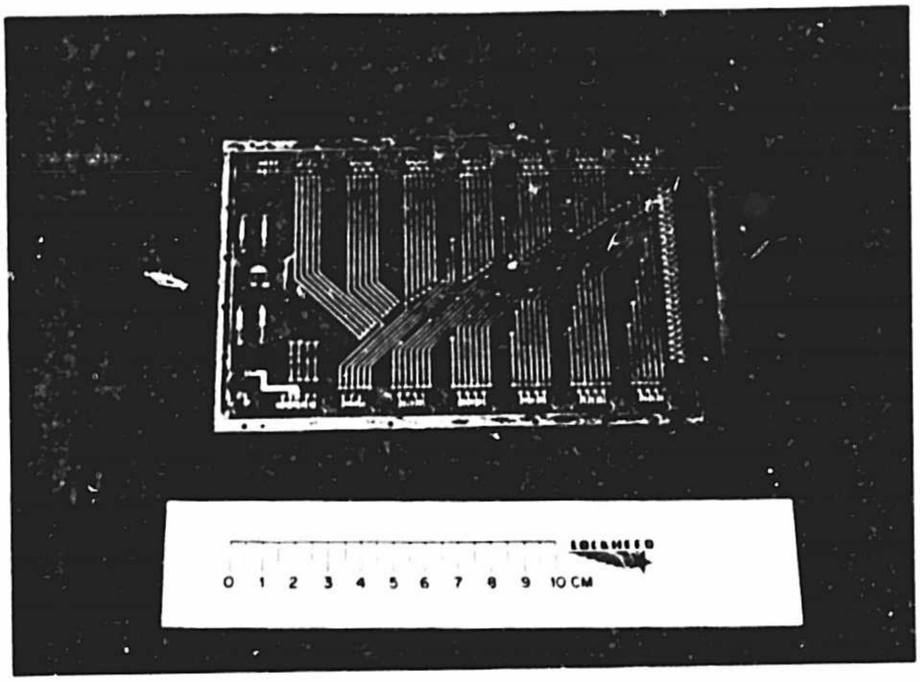

Figure 52. AB1A: Mass anodes preamps output signal routing.

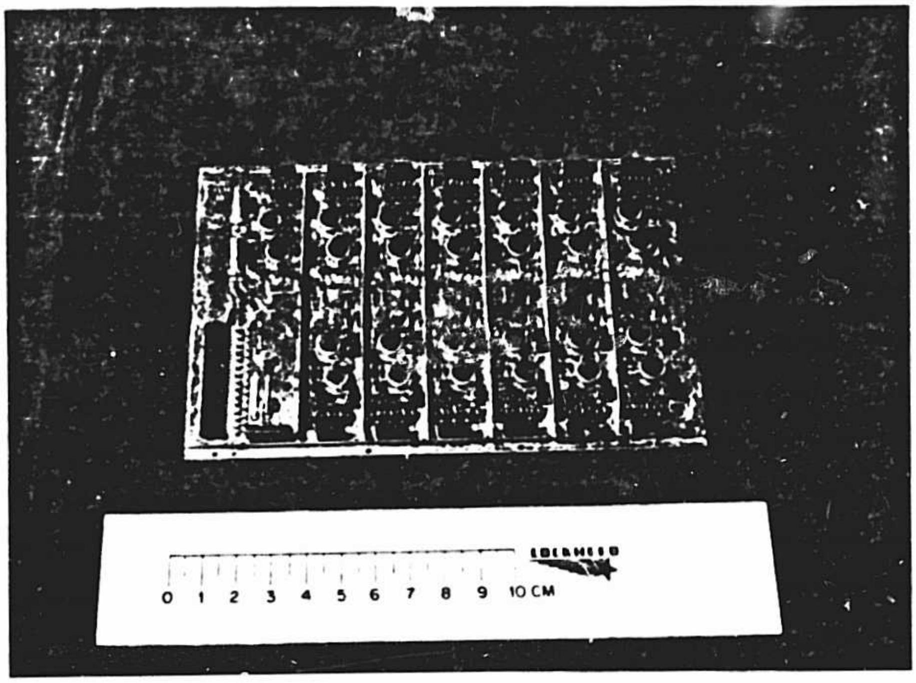

Figure 53. AB1: Mass anode summing and shaping amplifiers (13).

ORIGINAL PAGE IS
OF POOR QUALITY

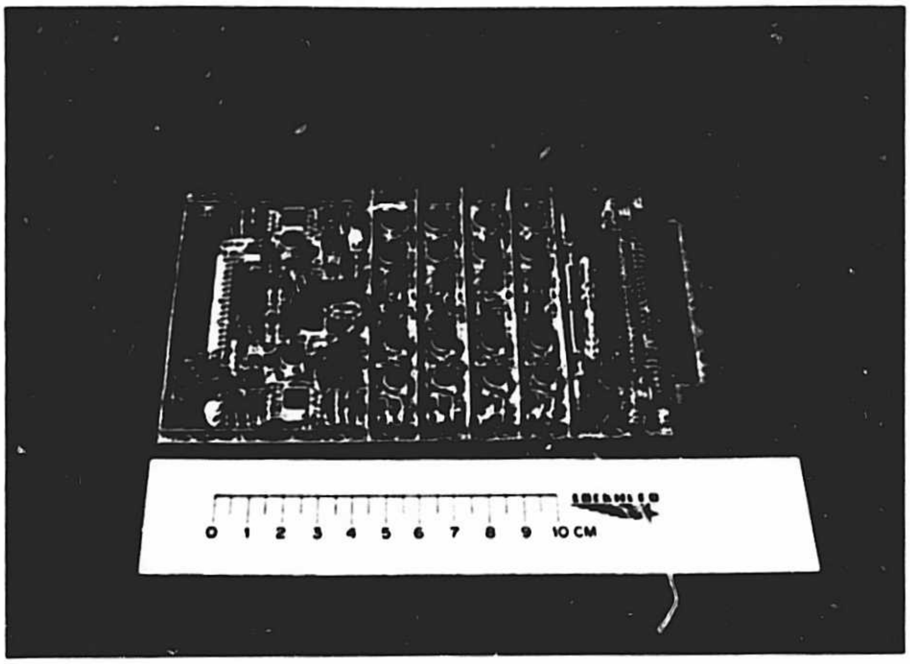

Figure 54. AB2: Mass and angle D/A converters (1 each), angle shaping amplifiers (8).

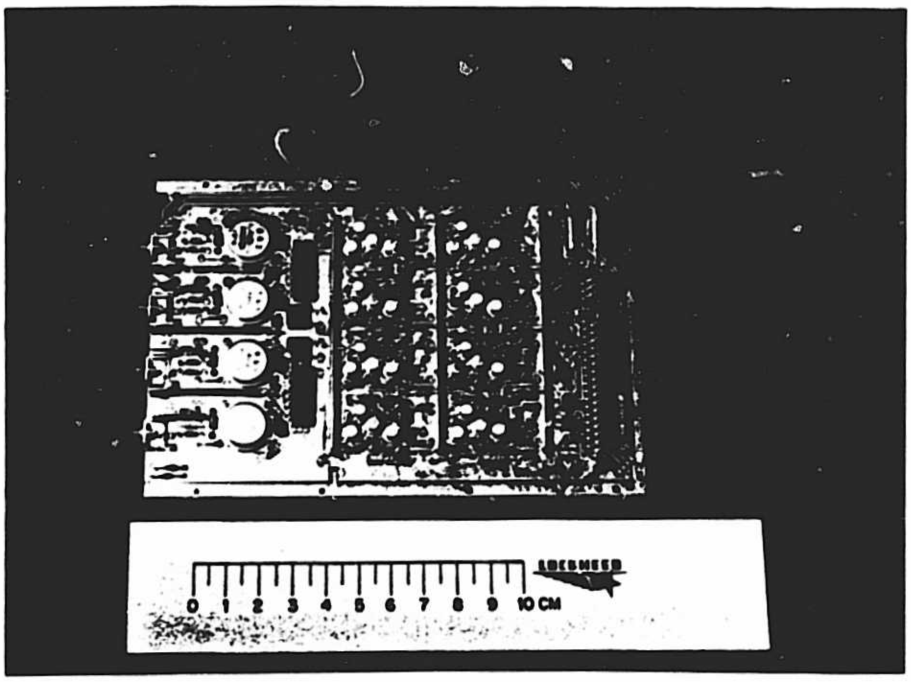

Figure 55. AB3: CEM amplifiers (4), angle LLD's (8).

C-8

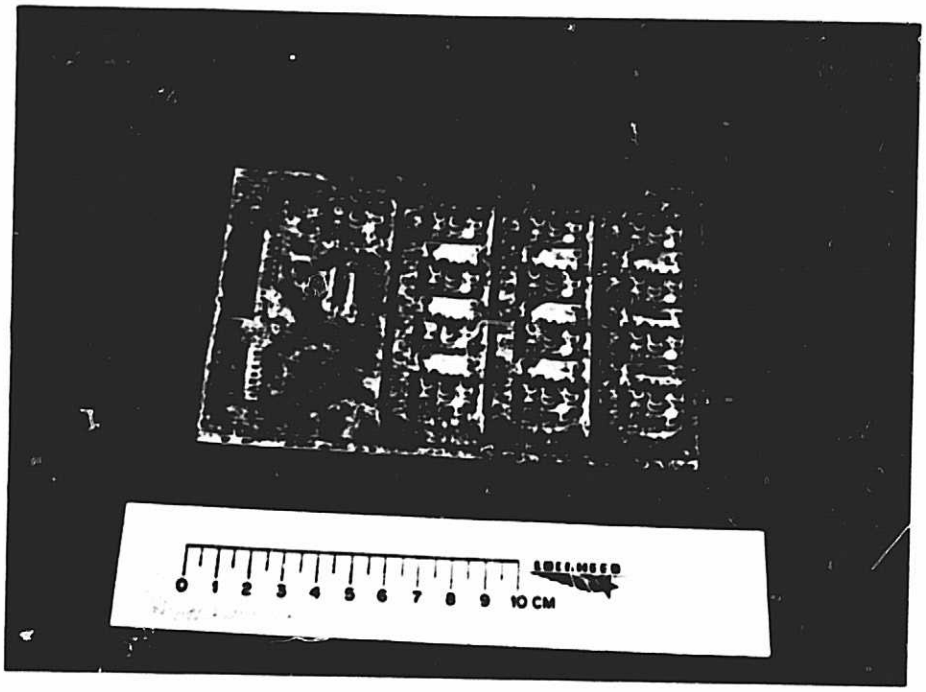

Figure 56. AB4: Mass anode LLD's (13).

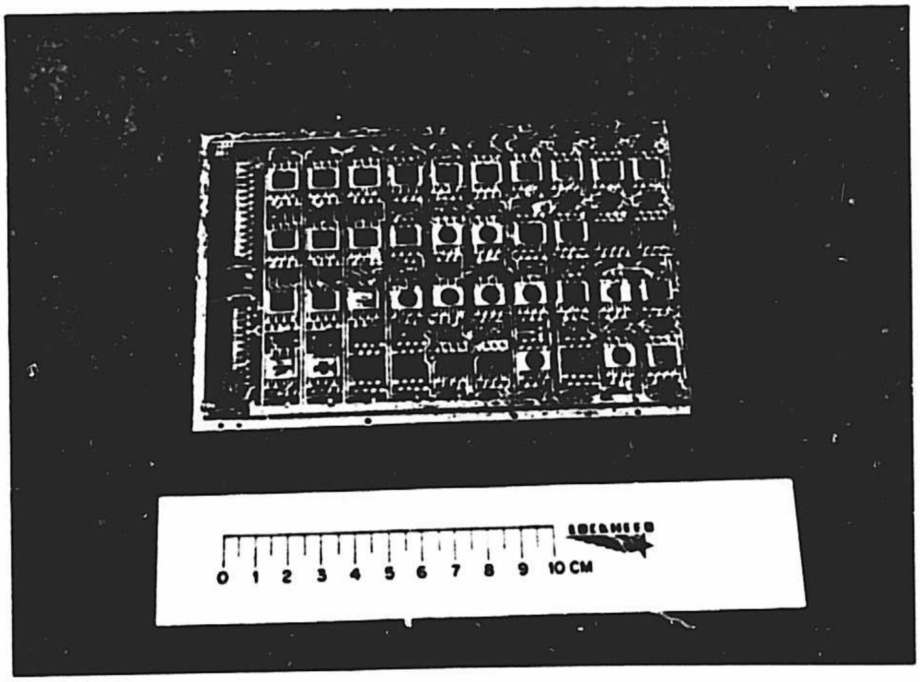

Figure 57. DB1: Coincidence and encoding logic.

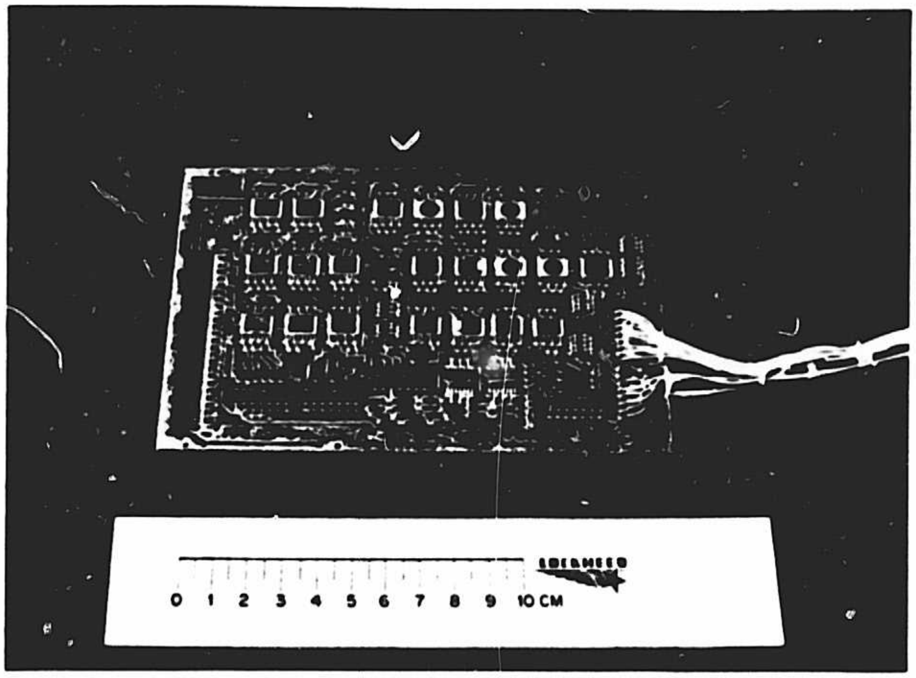

Figure 58. DB2: CEM signal conditioning (4), MCP and CEM test pulse generators (1 each), logic level shifting and MPAE 1/F circuits.

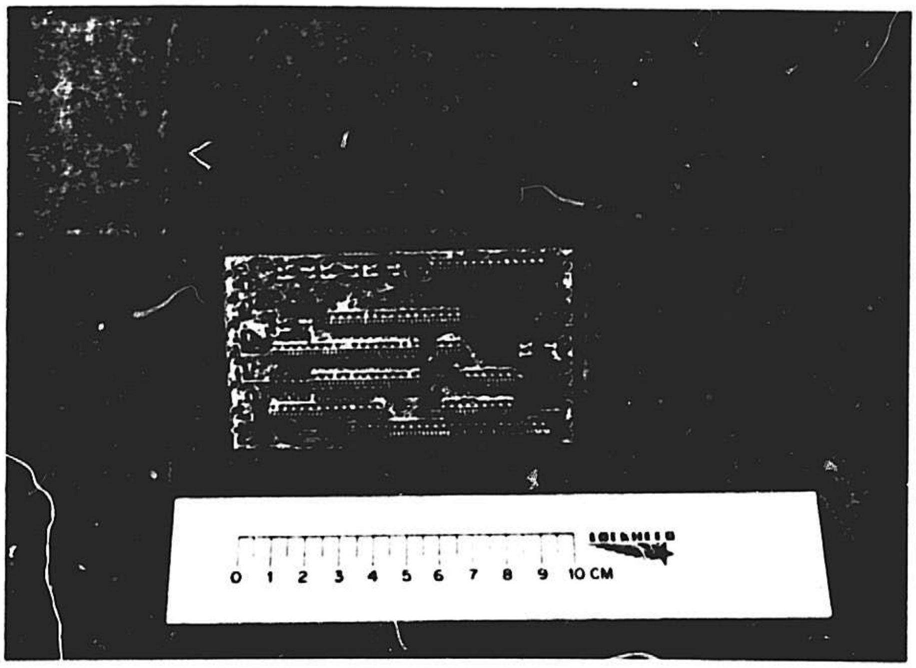

Figure 59. MB1: motherboard; power and signal routing.

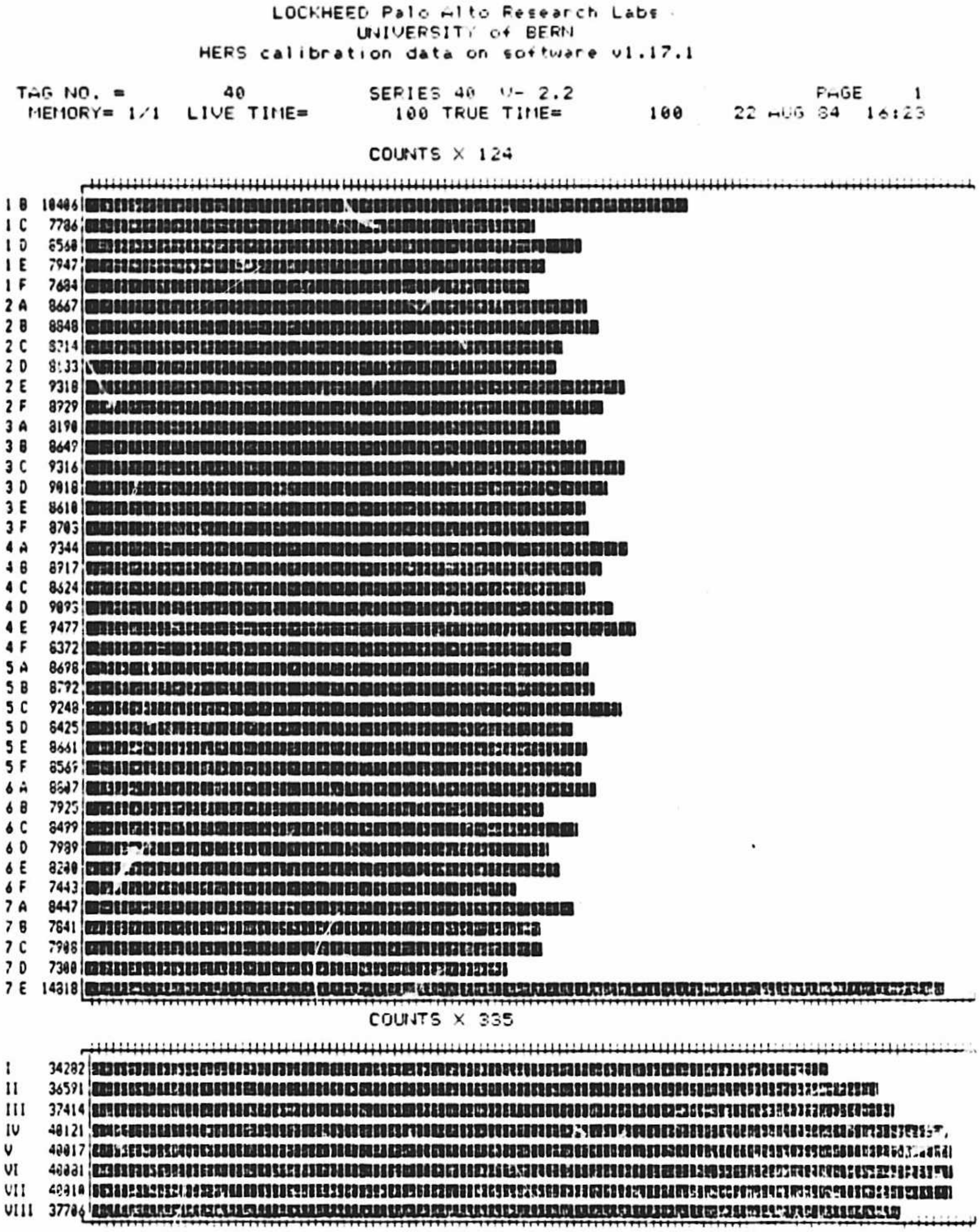

```
              LOCKHEED Palo Alto Research Labs
                   UNIVERSITY of BERN
          HERS calibration data on software v1.17.1

TAG NO. =        40        SERIES 40  V- 2.2                PAGE    1
 MEMORY= 1/1  LIVE TIME=     100 TRUE TIME=       100    22 AUG 84  16:23

                         COUNTS X 124

1 B  10406
1 C   7786
1 D   8560
1 E   7947
1 F   7684
2 A   8667
2 B   8848
2 C   8314
2 D   8133
2 E   9318
2 F   8729
3 A   8190
3 B   8649
3 C   9316
3 D   9018
3 E   8610
3 F   8703
4 A   9344
4 B   8717
4 C   8624
4 D   9093
4 E   9477
4 F   8372
5 A   8698
5 B   8792
5 C   9248
5 D   8425
5 E   8661
5 F   8569
6 A   8807
6 B   7925
6 C   8499
6 D   7989
6 E   8240
6 F   7443
7 A   8447
7 B   7641
7 C   7908
7 D   7300
7 E  14818

                         COUNTS X 335

I     34282
II    36591
III   37414
IV    40121
V     40017
VI    40081
VII   40010
VIII  37706
```

ORIGINAL PAGE IS
OF POOR QUALITY

Figure 60. MCP response to Nickel 63 input. Mass and angle responses shown are summed over all angles and masses respectively.

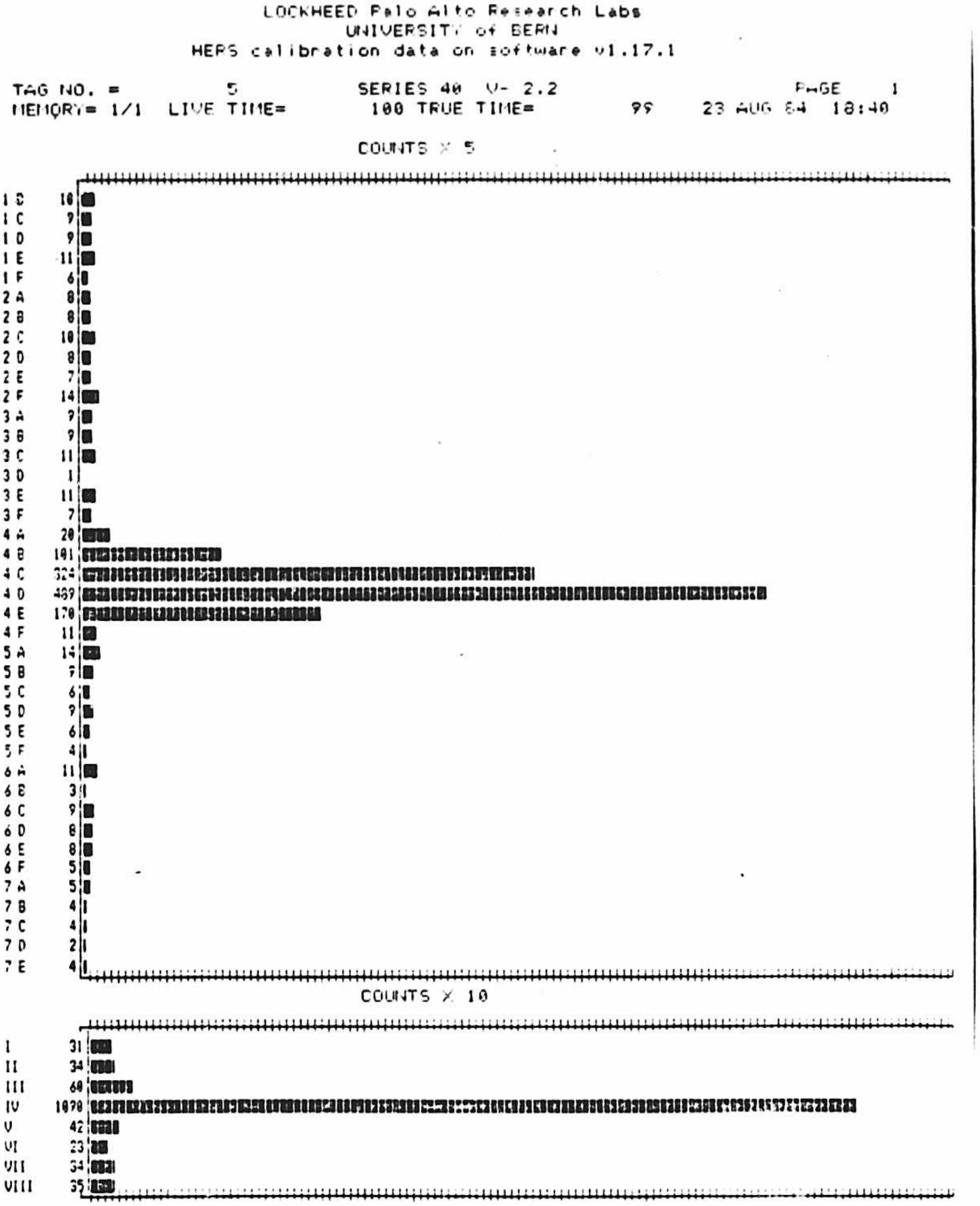

```
                 LOCKHEED Palo Alto Research Labs
                         UNIVERSITY of BERN
               HERS calibration data on software v1.17.1

TAG NO. =          5         SERIES 40  V- 2.2                     PAGE    1
MEMORY= 1/1  LIVE TIME=      100 TRUE TIME=         99   23 AUG 84  18:40

                              COUNTS X 5

1 B     10
1 C      9
1 D      9
1 E     11
1 F      6
2 A      8
2 B      8
2 C     10
2 D      8
2 E      7
2 F     14
3 A      9
3 B      9
3 C     11
3 D      1
3 E     11
3 F      7
4 A     20
4 B    101
4 C    324
4 D    489
4 E    170
4 F     11
5 A     14
5 B      7
5 C      6
5 D      9
5 E      6
5 F      4
6 A     11
6 B      3
6 C      9
6 D      8
6 E      8
6 F      5
7 A      5
7 B      4
7 C      4
7 D      2
7 E      4
                              COUNTS X 10

I       31
II      34
III     60
IV    1070
V       42
VI      23
VII     34
VIII    35
```

Figure 61. MCP response to a U.V. spot. Mass and angle responses shown are summed over all angles and masses respectively.

the MCP to examine the detailed response of the plate over particular areas such as the angle anode boundaries, see Figure 62. The MCP gain and charge thresholds were systematically altered to produce a data base to evaluate the systems gain and encoding characteristics using both the Ni^{63} and U. V. spot. Background runs were also performed to establish the distribution of the "dark" counts and total rate, see Figure 63. Based on the above tests an operating high voltage and charge threshold were selected to optimize the system response to total ions incident at the MCP input. The MCP presently installed in the FS is operated at a net bias of ~ -1600 VDC. The operating threshold for mass (and angle) signals is set at ~ .012 pC. This is well under the lower flank of the amplitude distribution for this plate as shown in Figure 64.

The proper performance at the selected operating levels is verified at the system level by logging the change in total events (flagged and unflagged) as the mass threshold is altered. For the FS detector the reduction in total event rate is less than 5% for a factor of 2 increase above the selected threshold. The events output without any conditional flagging are greater than 80% of the total events. The number of events containing "defects" in the angular position encoding is ~ 2%-5% over most of the MCP imaged area, excluding the narrow unmetallized gap between angle anodes. This area is difficult to probe in detail due to the large size of the U. V. spot. However it is estimated that over the entire plate image less than 5% of the event codes contain flagged ("defective") angle codes from these regions. The dark count average is < 4 counts/second over the image area used.

An important factor in high voltage and threshold selection is the overall uniformity of response over the surface of the plate when it is illuminated with the Ni^{63} source. Figure 60 shows the overall response for the FS MCP at the high voltage and charge threshold selected for operation. (All of the events

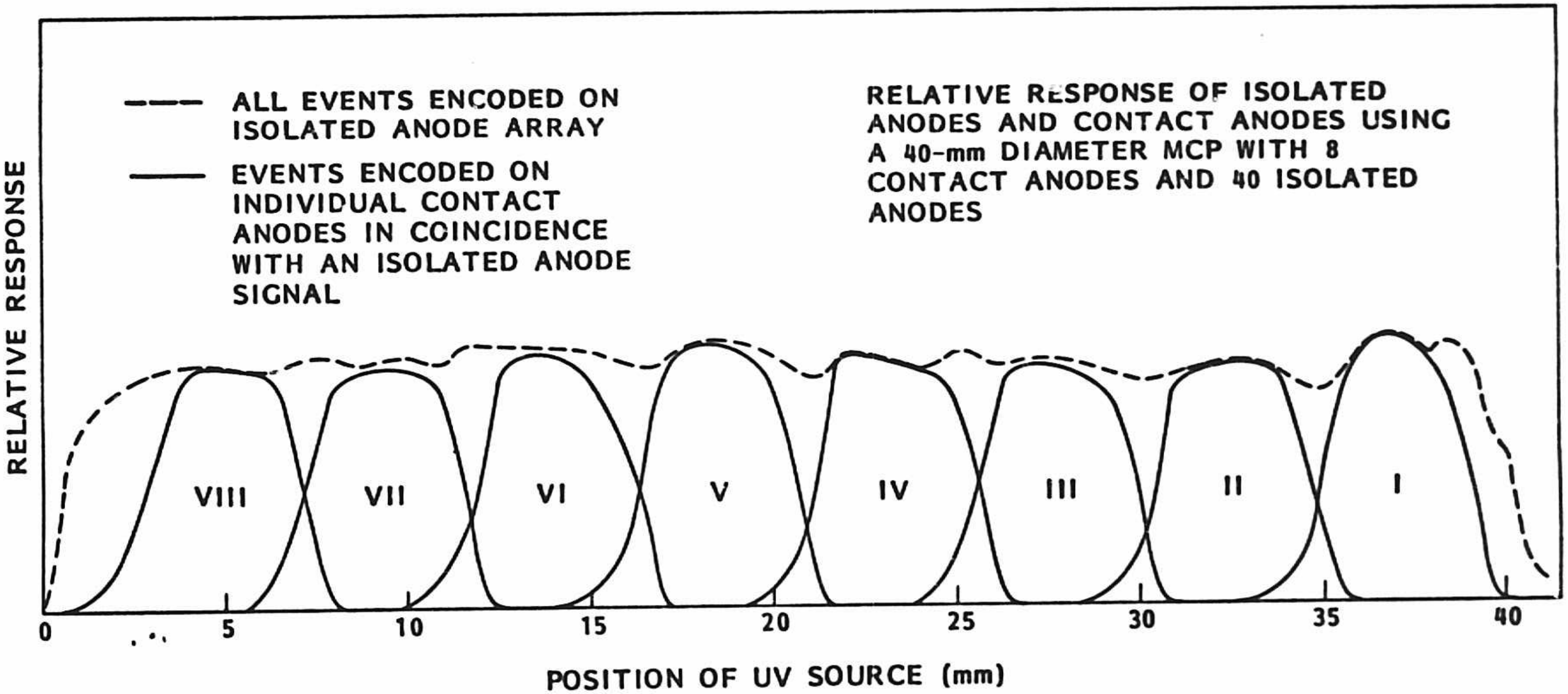

Figure 62. Typical response from a 2.5 mm U.V. spot scan.

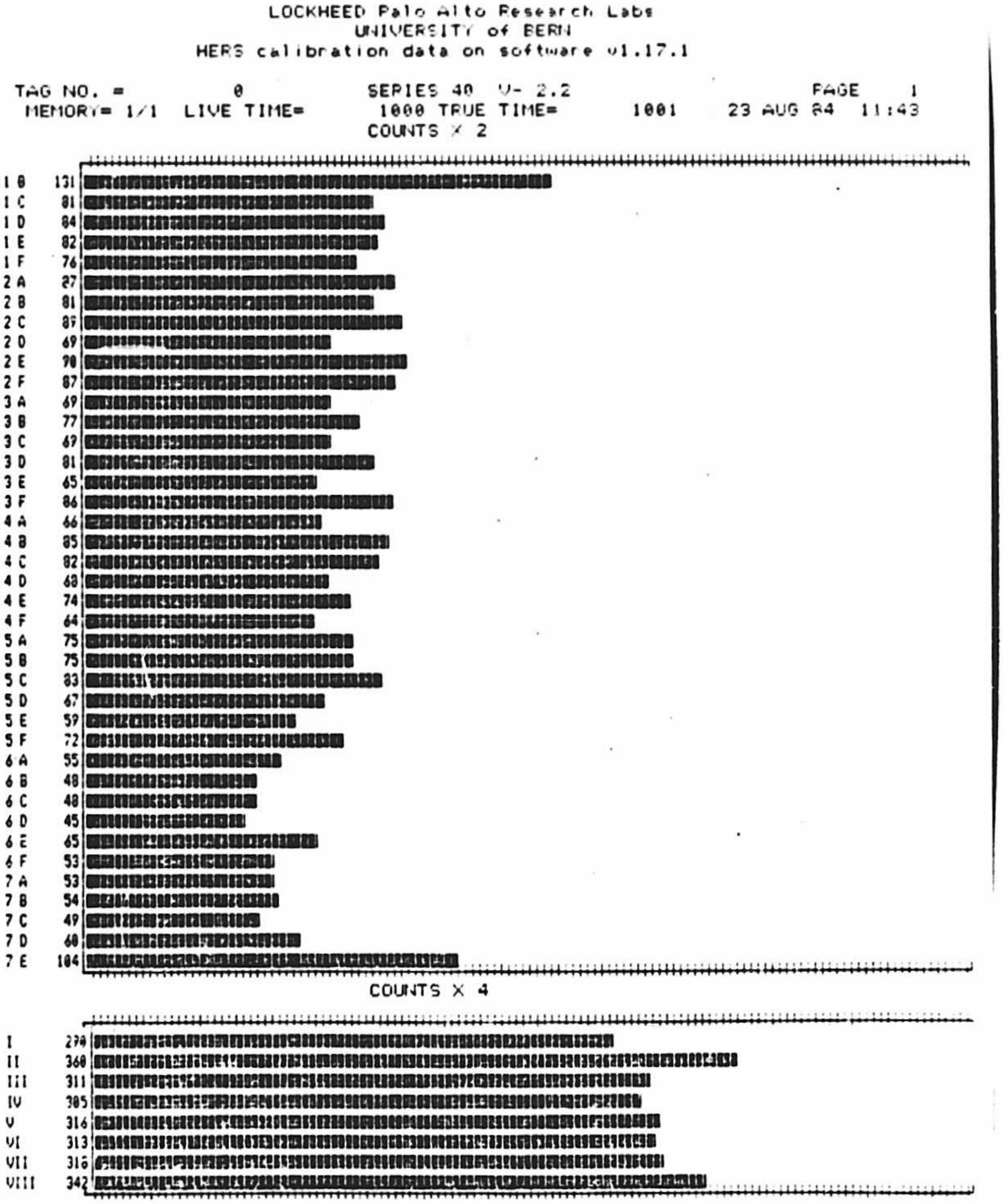

```
                    LOCKHEED Palo Alto Research Labs
                           UNIVERSITY of BERN
                 HERS calibration data on software v1.17.1

TAG NO. =           0          SERIES 40  V- 2.2                          PAGE    1
 MEMORY= 1/1  LIVE TIME=        1000 TRUE TIME=       1001    23 AUG 84   11:43
                               COUNTS X 2
```

Figure 63. MCP background; mass and angle responses shown are summed over all angles and masses respectively.

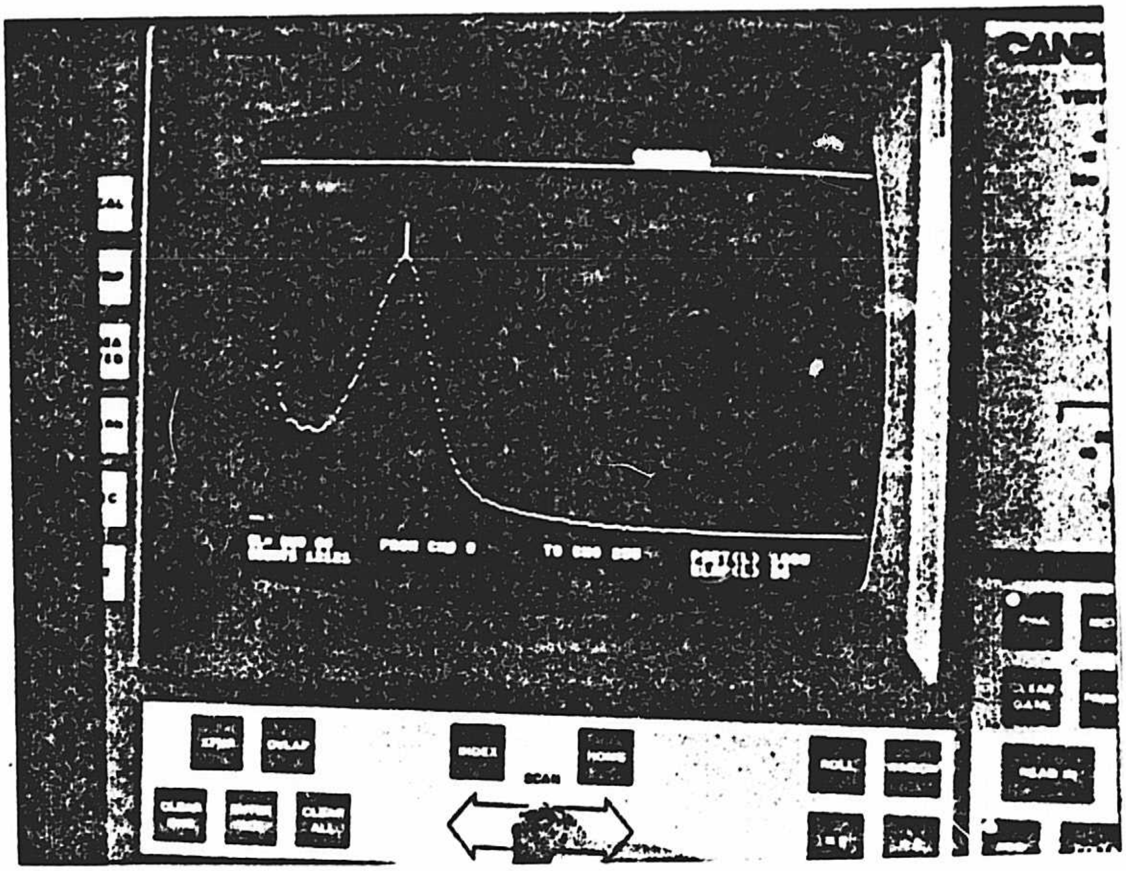

Figure 64. Flight spare MCP gain distribution at -1600 V. Gain peak is $5.9 \times 10^3 e^-$ ($\sim$ .1 pC) and FWHM = 55%.

shown in both mass and angle axis' were summed from only those events which did not contain a flag for either element [group or unit] of the mass component. All of the events shown along the angle axis did not contain any flags). The enhanced response at the first and last mass anodes is thought to be caused primarily by the proximity of a larger dielectric surface adjacent to these two end anodes, see Figure 42. Electrons stored on this surface will deflect some charge so that the effective collection area of these end anodes is increased. The anodes are being redesigned to correct this problem, and if successful will be installed into the flight system. In addition the lack of an adjacent anode on one side reduces the number of multiple events produced by charge spreading, therefore the number of unflagged events will be slightly higher for these two anodes.

The background distribution plot for the FS MCP is shown in Figure 63 and has the same event criteria as discussed above for Figure 60.

Tests at University of Bern in Switzerland

After the MCP and encoding tests are performed at LPARL, the system is joined to the optics portion of the HERS instrument and taken to a facility at the University of Bern where we can input various ion types over a range of energies and entrance angles. Here we can evaluate the image quality, total efficiency, and various artifacts produced within the sytem by the introduction of these elements. Figure 65 shows some preliminary results with the instrument configured for the medium mass range. Here methane, water, and other residual gas components (including Ar^{++}) were used to produce M/Q values of 12 through 20.

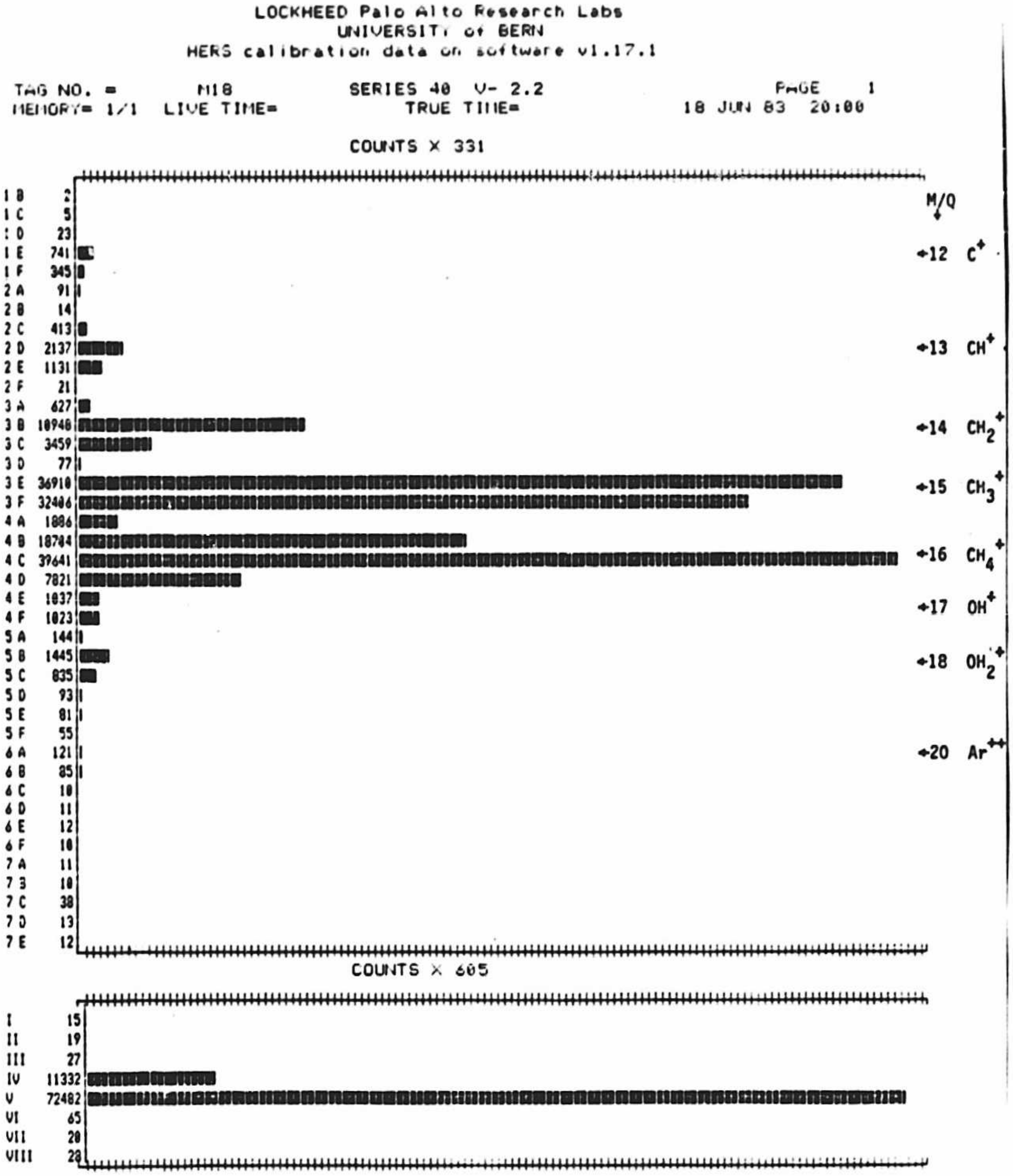

```
LOCKHEED Palo Alto Research Labs
UNIVERSITY of BERN
HERS calibration data on software v1.17.1

TAG NO. =        M18        SERIES 40  V- 2.2                PAGE    1
MEMORY= 1/1  LIVE TIME=           TRUE TIME=            18 JUN 83  20:00

                           COUNTS X 331
1 B      2
1 C      5
1 D     23
1 E    741
1 F    345
2 A     91
2 B     14
2 C    413
2 D   2137
2 E   1131
2 F     21
3 A    627
3 B  10946
3 C   3459
3 D     77
3 E  36910
3 F  32406
4 A   1886
4 B  18784
4 C  39641
4 D   7821
4 E   1037
4 F   1023
5 A    144
5 B   1445
5 C    835
5 D     93
5 E     81
5 F     55
6 A    121
6 B     85
6 C     10
6 D     11
6 E     12
6 F     10
7 A     11
7 B     10
7 C     38
7 D     13
7 E     12
                           COUNTS X 605
I        15
II       19
III      27
IV    11332
V     72482
VI       65
VII      20
VIII     28
```

Figure 65: A linear plot of a composite mass spectrum produced during preliminary instrument characterization at University of Bern, Switzerland.

The external ion energy was adjusted for each ion species independently to satisfy the constant momentum requirement imposed by the deflection magnet. Each of the M/Q measurements were corrected for background then all were added together to produce the composite spectrum, shown as a linear plot in Figure 65 and as a log plot in Figure 66. all species are resolved from one another at a level of greater than than 2×10^{-3} of the adjacent species.

LOCKHEED Palo Alto Research Labs
UNIVERSITY of BERN
HERS calibration data on software v1.17.1

TAG NO. = MI8 SERIES 40 V- 2.2 PAGE 1
MEMORY= 1/1 LIVE TIME= TRUE TIME= 18 JUN 83 20:00

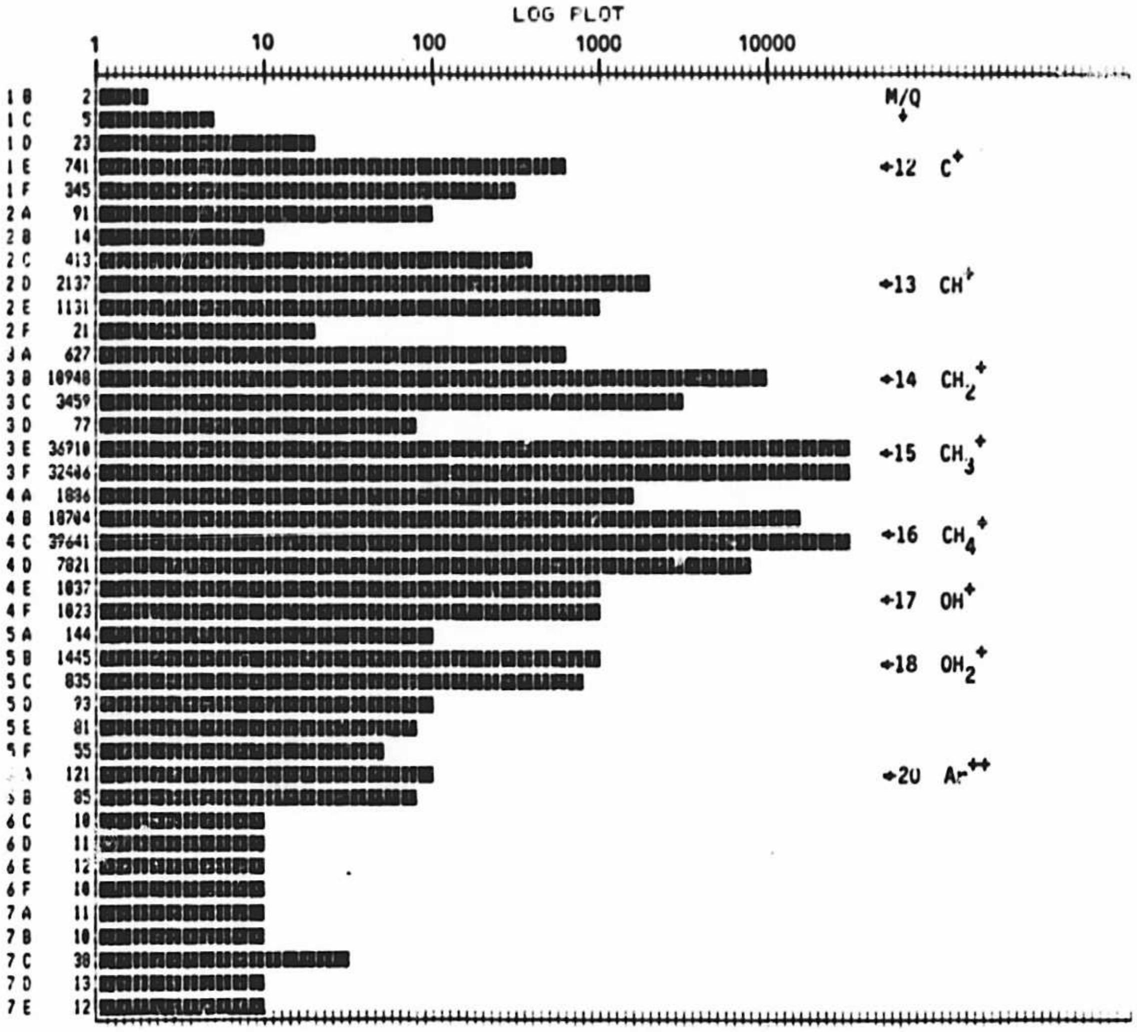

Figure 66: A log plot of the mass spectrum illustrated in the previous figure.

3. SUMMARY AND RECOMMENDATIONS

A High Energy Range Spectrometer (HERS) suitable for ion composition measurements during an encounter with the Comet Halley has been designed, developed, fabricated and delivered to the University of Bern to be integrated into the ESA GIOTTO Spacecraft. Lockheed personnel have supported the integration of the HERS ion optics with the Max Planck Institute provided electronics and have participated in the instrument calibration at the University of Bern.

It is anticipated that continued support for the instrument calibration, testing, launch, post launch operations and data analysis will be funded through the GIOTTO Co-Investigator Program.

This sophisticated instrument, which has been jointly developed by an international team of scientists, was specifically designed to provide the high mass resolution required to characterize the cometary environment. It is recommended that the NASA consider this proven instrument for future planetary missions including the possible cometary rendezvous mission.